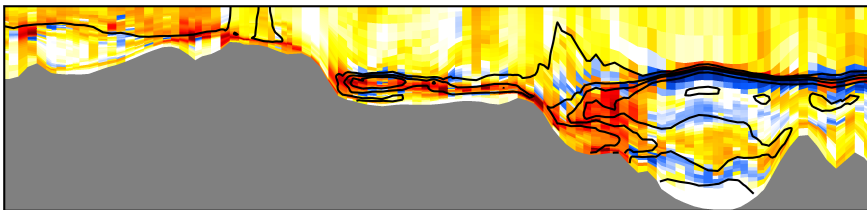

KNUT KLINGBEIL

**Approaches for the improvement of
physical transport processes
in numerical models of coastal oceans**



Dissertation
zur Erlangung des akademischen Grades
doctor rerum naturalium (Dr. rer. nat.)
der Mathematisch-Naturwissenschaftlichen Fakultät
der Universität Rostock

**Approaches for the improvement of
physical transport processes
in numerical models of coastal oceans**

VORGELEGT VON
KNUT KLINGBEIL

Rostock, 09.08.2013

Supervised by:



Prof. Dr. Hans Burchard
Leibniz Institute for Baltic Sea Research Warnemünde

Presented to:



The Institute of Physics
Faculty of Mathematics and Natural Sciences
University of Rostock

Reviewed by:

Prof. Dr. Hans Burchard
Dept. of Physical Oceanography and Instrumentation
Leibniz Institute for Baltic Sea Research Warnemünde

Prof. Dr. Oliver Fringer
Dept. of Civil and Environmental Engineering
Stanford University

Date of defence:

19 February 2014

Declaration

I hereby declare under oath that I have completed the work submitted here independently and have composed it without outside assistance. Furthermore, I have not used anything other than the resources and sources stated and where I have taken sections from these works in terms of content or text, I have identified this appropriately.

09 August 2013

Abstract

The increasing computational power of today's computers significantly extends the applicability of numerical models for the investigation of oceanic and estuarine flows. In particular, simulations with much higher resolution become feasible. This development offers but also requires different modifications to the established coastal ocean models. Coastal ocean models simulate currents and the physical transport of momentum, energy, sediment and other species driven by them. In this thesis three approaches to improve the simulated transport processes in coastal ocean models are discussed. These approaches address different levels of the modelling procedure. The first approach deals with the discretisation of the governing equations and provides a diagnostic tool to assess the accuracy of a numerical transport scheme. The second approach considers the validity of the governing equations itself and suggests an alternative inclusion of missing nonhydrostatic dynamics. The third approach presents the inclusion of unresolved wind wave effects into a coastal ocean model.

Zusammenfassung

Die zunehmende Rechenleistung heutiger Computer erweitert die Anwendungsmöglichkeiten von numerischen Modellen zur Untersuchung von ozeanischen und ästuaren Strömungen wesentlich. Insbesondere Simulationen mit deutlich höherer Auflösung werden realisierbar. Diese Entwicklung ermöglicht und erfordert diverse Anpassungen der bestehenden Küstenozeanmodelle. Küstenozeanmodelle simulieren Strömungen und den von ihnen angetriebenen physikalischen Transport von Impuls, Energie, Sediment und anderen Stoffen. In dieser Arbeit werden drei Ansätze zur Verbesserung der simulierten Transportprozesse in Küstenozeanmodellen diskutiert. Diese Ansätze adressieren verschiedene Stufen der Modellierung. Der erste Ansatz befasst sich mit der Diskretisierung der Grundgleichungen und stellt ein Diagnosewerkzeug für die Beurteilung von numerischen Transportverfahren bereit. Der zweite Ansatz betrachtet die Gültigkeit der Grundgleichungen an sich und regt eine alternative Einbeziehung fehlender nichthydrostatischer Dynamik an. Der dritte Ansatz stellt die Einbeziehung der Effekte von nicht aufgelösten Windwellen in ein Küstenozeanmodell vor.

Contents

List of Figures	vii
List of Tables	ix
1. Introduction	1
1.1. Outline	3
2. The governing hydrodynamic equations	5
2.1. The Navier-Stokes Equations	5
2.2. Treatment of the pressure	6
2.2.1. Pressure decomposition	6
2.2.2. The hydrostatic pressure assumption	8
2.3. Turbulence	9
3. The General Estuarine Transport Model (GETM)	11
3.1. The governing equations of GETM	11
3.2. Concepts	12
3.2.1. Transformation to general vertical coordinates and layer integration	13
3.2.2. Explicit mode-splitting	15
3.2.3. Outline of the time loop	17
4. Analysis of spurious dissipation and mixing	21
4.1. Introduction	21
4.2. Basics	22
4.2.1. Analytical variance decay (AVD)	22
4.2.2. Discrete variance decay (DVD)	23
4.2.2.1. The DVD analysis method of Burchard and Rennau (2008, BR08)	26
4.2.2.2. An alternative DVD analysis method (K13)	27
4.2.3. Implementation into 3D ocean models	27
4.2.3.1. The 3D DVD analysis method of Burchard and Rennau (2008, BR08)	27
4.2.3.2. The 3D extension of the alternative DVD analysis method (K13)	28
4.2.4. 3D dissipation analysis	30
4.2.4.1. Dissipation due to a transversely isotropic stress tensor	30
4.3. Applications	33
4.3.1. Analysis of 1D TVD-schemes	34
4.3.2. Analysis of an idealised mesoscale eddy	38
4.3.3. Analysis of a realistic Western Baltic Sea model	42
4.4. Conclusions	49
5. Inclusion of nonhydrostatic dynamics	51
5.1. Introduction	51
5.2. Basics	54
5.2.1. Breakdown of the hydrostatic pressure assumption	54

5.2.2. Outline of a straight-forward nonhydrostatic extension	54
5.3. Straight-forward extension of the General Estuarine Transport Model	57
5.3.1. Transformation to general vertical coordinates and layer integration	57
5.3.2. Explicit mode-splitting	58
5.3.3. Implementation	58
5.3.4. Stability issues	59
5.4. Simulations with the extended GETM	59
5.4.1. Dispersing interfacial waves	60
5.4.2. Lock-exchange	60
5.4.3. Sloshing basin waves	62
5.4.3.1. 2D setup	62
5.4.3.2. 3D setup	67
5.4.3.3. A moderately nonhydrostatic standing wave	68
5.4.4. Tidally induced internal lee waves	68
5.4.5. Analysis of a realistic Western Baltic Sea model	71
5.5. Discussion	72
5.6. Conclusions	73
6. Inclusion of wind wave effects	75
6.1. Introduction	75
6.2. Modified governing equations	76
6.2.1. Details of the Radiation Stress formulation	78
6.2.2. Details of the Vortex Force formulation	79
6.2.3. Vertical distribution of wave-induced forcing	79
6.2.4. Further modifications	80
6.3. Summary of Moghimi et al. (2012)	80
6.4. Conclusions and Outlook	81
7. Summary and Outlook	83
A. Constitutive relations	I
A.1. The Stress tensor	I
A.1.1. The viscous stress tensor	I
A.1.2. The turbulent stress tensor	III
A.2. The heat flux	VIII
A.2.1. The molecular heat flux	VIII
A.2.2. The turbulent heat flux	IX
B. Discrete Variance Decay	XI
B.1. Comments on higher-order TVD-schemes	XI
B.2. DVD due to diffusion	XIII
B.3. DVD due to the explicit FOU scheme	XIV
B.4. An alternative derivation of χ^{K13}	XV
C. The temporal resolution of nonhydrostatic effects	XIX
Nomenclature	XXI
Bibliography	XXIII

List of Figures

1.1. The bricks of modelling	2
4.1. Analysis of 1D TVD-schemes	36
4.2. Analysis of an idealised mesoscale eddy: Evolution of global energy composition . . .	39
4.3. Analysis of an idealised mesoscale eddy: Dissipation and mixing analysis (after 1 day)	40
4.4. Analysis of an idealised mesoscale eddy: Dissipation and mixing analysis (after 19 days)	41
4.5. Analysis of a realistic Western Baltic Sea model: Map of model domain	43
4.6. Analysis of a realistic Western Baltic Sea model: Longterm validation	44
4.7. Analysis of a realistic Western Baltic Sea model: Mixing analysis (salinity)	45
4.8. Analysis of a realistic Western Baltic Sea model: Mixing analysis (temperature) . . .	46
4.9. Analysis of a realistic Western Baltic Sea model: Dissipation analysis	47
5.1. Dispersing interfacial waves: Snapshots	61
5.2. Dispersing interfacial waves: Interface displacement	62
5.3. Lock-exchange	63
5.4. 2D Sloshing basin waves: Evolution of surface elevation	64
5.5. 2D Sloshing basin waves: Snapshot after $t = 7.6$ s	65
5.6. 2D Sloshing basin waves: Graphical representation of Table 5.1	66
5.7. 3D sloshing basin waves	67
5.8. A moderately nonhydrostatic standing wave	68
5.9. Tidally induced internal lee waves	70
5.10. Analysis of a realistic Western Baltic Sea model: Nonhydrostatic effects	71
B.1. Advection in a FV-framework	XVI

List of Tables

4.1. Analysis of 1D TVD-schemes	37
5.1. 2D Sloshing basin waves: Convergence analysis	66

Chapter 1.

Introduction

The increasing computational power significantly extends the applicability of numerical models for the investigation of oceanic and estuarine flows. In particular, simulations with much higher resolution become feasible. However, the blind application of the established numerical models will not automatically lead to improved simulation results, because the development of higher-resolution setups must be associated with different modifications to the established coastal ocean models. The purpose of coastal ocean models is the correct simulation of velocity fields, driven by various forces and responsible for the physical transport of momentum, energy, sediment and other species. In this thesis three approaches to improve the simulated transport processes in coastal ocean models are discussed. These approaches address different levels of the modelling procedure.

Figure 1.1 depicts the key elements of numerical modelling. Observed events and processes are manifestations of a physical system. In a first step the functioning of this physical system has to be translated into a closed set of mathematical equations those analytical solutions should describe the observations as good as possible. For fluid dynamics the mathematical model is based on balance laws consistent with the fundamental physical principles. Closed with constitutive relations, the derived Navier-Stokes Equations represent the governing equations. Unfortunately, for most realistic applications these equations are too complex to be solved analytically. Computer-based solutions can be obtained, if in a second step the continuous equations are discretised into algebraic equations. Yet, this discretisation introduces truncation errors, causing deviations between the discrete and analytical solution. Further errors are added due to the numerical solver. Therefore, the obtained numerical solution will deviate from the observation for different reasons and its significance has to be ensured by both the verification of the implementation and the validation of the mathematical model.

The first approach to improve the simulated transport processes in coastal ocean models addresses the discretisation. It is well known, that the *advective transport* needs to be discretised with sufficient accuracy to minimise truncation errors. These truncation errors can cause the numerical solution to violate the conservation of second moments, a basic property of the advected continuous solution. The numerical loss of second moment (*variance decay*) is referred to as *spurious mixing* (for advected tracers) and *spurious dissipation* (for advected momentum). To assess the performance of advection schemes a reliable diagnostic method is developed to quantify their associated local numerical variance decay. Furthermore, based on this diagnostic method, a dissipation analysis to quantify the loss of 3D kinetic energy for a staggered arrangement of the velocity components is presented. The decrease of numerical variance decay, either due to improved advection schemes or due to improved resolution, offers and also requires the increase of physically induced variance decay to accurately simulate transport processes.

In contrast to the first, **the second approach** addresses the mathematical model. Due to the continuous improvement of model resolution basic approximations to the governing equations can become invalid. The *hydrostatic pressure assumption* is valid for sufficiently small aspect ratios between typical vertical to typical horizontal length scales and strongly simplifies the governing equations. However, these length scales are not only determined by the process of interest, but also by the processes present

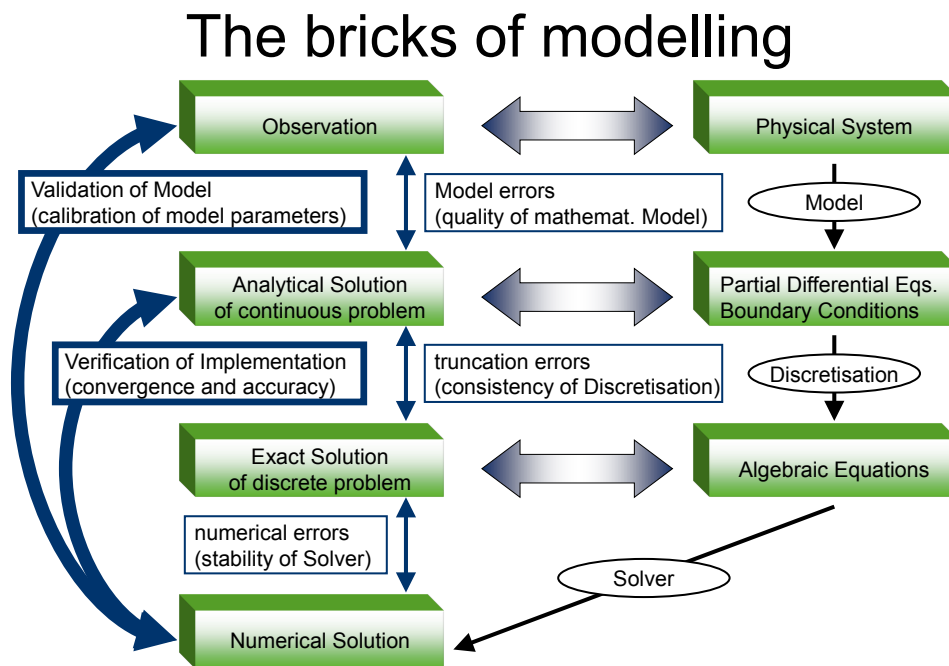


Figure 1.1.: The bricks of modelling (motivated by Griebel et al. (1998) and Hirsch (2007))

in a given numerical resolution. The invalidity of the hydrostatic pressure assumption demands the withdrawal of the simplifications of the governing equations and implies crucial modifications to the numerical model. As an alternative to common nonhydrostatic model procedures, for weak nonhydrostatic processes an extension of the original hydrostatic procedure is presented that requires only minimal modifications. The potential of this *alternative inclusion of nonhydrostatic effects* for future ocean modelling applications is assessed. The inclusion of nonhydrostatic dynamics offers the correct simulation of recirculation patterns and thus can lead to a more realistic transport of quantities.

The third approach addresses again the mathematical model, but in contrast to the second approach it includes effects of unresolved processes. In the context of turbulence, the necessity of a proper parameterisation of unresolved processes for the resolved mean flow is long known. In addition to turbulence, wind waves can significantly affect the mean flow by releasing additional momentum fluxes. The proper *inclusion of wind wave effects* into a coastal ocean model is possible by modifications to its governing equations. These modifications are presented for two different formulations, recently established within the ocean modelling community. The additional forcing terms depend on wave properties that can be provided by a statistical wind wave model. After the inclusion of wind wave effects the modelled transports of species, in particular of sediment, are significantly improved.

1.1. Outline

The present thesis is based on the author's contributions to the following publications:

- Moghimi, S., **K. Klingbeil**, U. Gräwe, H. Burchard (2012)
A direct comparison of a depth-dependent Radiation stress formulation and a Vortex force formulation within a three-dimensional coastal ocean model.
Ocean Modelling; doi:10.1016/j.ocemod.2012.10.002
- **Klingbeil, K.** and H. Burchard (2013)
Implementation of a direct nonhydrostatic pressure gradient discretisation into a layered ocean model.
Ocean Modelling; doi:10.1016/j.ocemod.2013.02.002
- **Klingbeil, K.**, M. Mohammadi-Aragh, U. Gräwe, H. Burchard (2013)
Quantification of spurious dissipation and mixing – Discrete Variance Decay in a Finite-Volume framework.
Ocean Modelling; submitted
- Gräwe, U., P. Holtermann, **K. Klingbeil**, H. Burchard
Advantages of vertically adaptive coordinates in numerical models of stratified shelf seas.
Ocean Modelling; in preparation
- Holtermann, P., H. Burchard, U. Gräwe, **K. Klingbeil**, L. Umlauf
Evolution of an anthropogenic tracer in a stratified basin with intensified boundary mixing.
Journal of Geophysical Research; in preparation

Paragraphs taken from the author's own contributions to these publications will not be highlighted again in the thesis. In addition, some derivations in Klingbeil and Burchard (2013) are based on Klingbeil (2009) and are repeated in this thesis as well.

In Chapter 2 the governing equations for ocean modelling are summarised. Based on these equations, in Chapter 3 the General Estuarine Transport Model (GETM) is presented as the utilised numerical model. The first of the three approaches to improve the modelled transport processes, addressing the truncation errors of the discretisation, is presented in Chapter 4 and covers the study of Klingbeil et al. (2013). The usefulness of the developed diagnostic tool is demonstrated in Gräwe et al. (in prep.), assessing the performance of different vertical meshing techniques in terms of spurious mixing. After the improvement of the advective transports in GETM, the implementation of a so far missing physically sound parameterisation for lateral mixing was necessary for the study of Holtermann et al. (in prep.). The second approach, dealing with the inclusion of missing nonhydrostatic dynamics, is discussed in Chapter 5 and was published in Klingbeil and Burchard (2013). The third approach, outlining the inclusion of wind waves into coastal ocean models, is presented in Chapter 6 and provided the governing equations for Moghimi et al. (2012). In addition to the detailed conclusions in the single chapters, a summary of the thesis and an outlook are given in Chapter 7.

Chapter 2.

The governing hydrodynamic equations

2.1. The Navier-Stokes Equations

In Figure 1.1 the need of a precise mathematical formulation of the physical system for the development of a numerical model is obvious. For fluid dynamics the mathematical model yields the Navier-Stokes Equations (NSE). These equations can be derived from the fundamental physical principles (see e.g. Spurk and Aksel, 2008). For simplicity in the present thesis the governing equations are formulated with reference to a local Cartesian system at the surface of the rotating earth with axes pointing towards the east, the north and upwards. Under the Boussinesq approximation (see e.g. Kundu and Cohen, 2008), the incompressibility constraint and NSE are then given by:

$$0 = \frac{\partial u}{\partial x} + \frac{\partial v}{\partial y} + \frac{\partial w}{\partial z}, \quad (2.1a)$$

$$\begin{aligned} & \frac{\partial u}{\partial t} + \frac{\partial}{\partial x} \{uu\} + \frac{\partial}{\partial y} \{vu\} + \frac{\partial}{\partial z} \{wu\} + f_h w - f_v v \\ & = - \frac{\partial}{\partial x} \left\{ \frac{p}{\rho_0} \right\} + F_x, \end{aligned} \quad (2.1b)$$

$$\begin{aligned} & \frac{\partial v}{\partial t} + \frac{\partial}{\partial x} \{uv\} + \frac{\partial}{\partial y} \{vv\} + \frac{\partial}{\partial z} \{wv\} + f_v u \\ & = - \frac{\partial}{\partial y} \left\{ \frac{p}{\rho_0} \right\} + F_y, \end{aligned} \quad (2.1c)$$

$$\begin{aligned} & \frac{\partial w}{\partial t} + \frac{\partial}{\partial x} \{uw\} + \frac{\partial}{\partial y} \{vw\} + \frac{\partial}{\partial z} \{ww\} - f_h u \\ & = - \frac{\rho}{\rho_0} g - \frac{\partial}{\partial z} \left\{ \frac{p}{\rho_0} \right\} + F_z. \end{aligned} \quad (2.1d)$$

This set of equations couples the velocity (u, v, w) , the density ρ and the pressure p . In the balance of momentum (2.1b) – (2.1d) f_h , f_v , ρ_0 and g are the horizontal and vertical Coriolis parameter, the reference density and the gravitational acceleration, respectively. Molecular friction is incorporated by forces (F_x, F_y, F_z) obtained from the divergence of a corresponding deviatoric viscous stress tensor (see Appendix A.1.1).

Assuming that a bounding surface of the fluid is always a material surface, kinematic boundary conditions can be derived (Spurk and Aksel, 2008). For the free surface with elevation $\eta(x, y, t)$ and the bottom with depth $H(x, y)$ these are given by:

$$0 = \frac{\partial \eta}{\partial t} + u \Big|_{z=\eta} \frac{\partial \eta}{\partial x} + v \Big|_{z=\eta} \frac{\partial \eta}{\partial y} - w \Big|_{z=\eta}, \quad (2.2a)$$

$$0 = u \Big|_{z=-H} \frac{\partial H}{\partial x} + v \Big|_{z=-H} \frac{\partial H}{\partial y} + w \Big|_{z=-H}. \quad (2.2b)$$

The system of governing equations is completed by prognostic equations for temperature T and salinity S and is closed by the thermal equation of state $\rho(T, S)$. Because these do not enter the following derivations they are not discussed further.

2.2. Treatment of the pressure

Under the Boussinesq approximation the pressure is degenerated to a Lagrangian multiplier (see e.g. Ferziger and Perić, 1997), instantaneously enforcing a solenoidal velocity field constrained by the incompressibility constraint (2.1a). In this Section the special treatment of the pressure is described.

2.2.1. Pressure decomposition

For a fluid at rest (2.1b) – (2.1d) define pressure and density distributions p_r and ρ_r in strict *hydrostatic balance*:

$$\frac{\partial p_r}{\partial x} = 0, \quad (2.3)$$

$$\frac{\partial p_r}{\partial y} = 0, \quad (2.4)$$

$$\frac{\partial p_r}{\partial z} = -\rho_r g. \quad (2.5)$$

Only perturbations from these resting quantities are dynamically relevant. The dynamic pressure may be decomposed into hydrostatic (hs) and nonhydrostatic (nh) contributions,

$$p - p_r = p'_{hs} + p_{nh}, \quad (2.6)$$

with the hydrostatic pressure perturbation defined similar to (2.5), but in terms of the dynamic density:

$$\frac{\partial p'_{\text{hs}}}{\partial z} = -(\rho - \rho_r)g. \quad (2.7)$$

Although numerical truncation errors can be reduced by replacing the pressure and the density in (2.1b) – (2.1d) by the perturbation quantities, here the full pressure is retained and decomposed according to:

$$p = p_r + p'_{\text{hs}} + p_{\text{nh}} = p_{\text{hs}} + p_{\text{nh}}. \quad (2.8)$$

Defining the nonhydrostatic buoyancy b_{nh} by

$$b_{\text{nh}} = \frac{\partial w}{\partial t} + \frac{\partial}{\partial x} \{uw\} + \frac{\partial}{\partial y} \{vw\} + \frac{\partial}{\partial z} \{ww\} - f_{\text{h}}u - F_z, \quad (2.9)$$

combination of (2.1d), (2.5), (2.7) and (2.9) yields:

$$\frac{\partial p_{\text{hs}}}{\partial z} = -\rho g, \quad (2.10a)$$

$$\frac{\partial p_{\text{nh}}}{\partial z} = -\rho_0 b_{\text{nh}}. \quad (2.10b)$$

Due to the Boussinesq approximation (2.10a) lost its transcendental character and the hydrostatic pressure contribution can be obtained independently from the nonhydrostatic one by vertical integration:

$$p_{\text{hs}} = p \Big|_{z=\eta} + \int_z^\eta \rho g dz. \quad (2.11)$$

With the buoyancy,

$$b = -\frac{\rho - \rho_0}{\rho_0} g, \quad (2.12)$$

the hydrostatic pressure contribution can be further decomposed into barotropic and baroclinic parts:

$$p_{\text{hs}} = p \Big|_{z=\eta} + \rho_0 g (\eta - z) - \rho_0 \int_z^\eta b dz. \quad (2.13)$$

2.2.2. The hydrostatic pressure assumption

From (2.7) and (2.10b) the ratio of the dynamic relevant pressure contributions is given by:

$$\mathcal{O} \left\{ \frac{p_{\text{nh}}}{p_{\text{hs}}} \right\} = \mathcal{O} \left\{ \frac{b_{\text{nh}}}{\frac{\rho - \rho_r}{\rho_0} g} \right\} \approx \mathcal{O} \left\{ \frac{b_{\text{nh}}}{b} \right\}. \quad (2.14)$$

With typical horizontal and vertical length scales (\mathcal{L} and \mathcal{H}), horizontal and vertical velocities (\mathcal{U} and \mathcal{W}) and the buoyancy frequency $N = \sqrt{-\partial_z b}$ dimensionless numbers can be defined: the aspect ratio $\delta = \frac{\mathcal{H}}{\mathcal{L}}$, the Richardson number $\text{Ri} = \left(\frac{N\mathcal{H}}{\mathcal{U}}\right)^2$, the Rossby number $\text{Ro} = \frac{\mathcal{U}}{|f_h|\mathcal{L}}$ and the horizontal divergence number $\Upsilon = \frac{\mathcal{W}}{\delta\mathcal{U}} \lesssim 1$. Scaling of the buoyancy equation then shows (also see Marshall et al., 1997, 1998):

$$\mathcal{O}(b) = \Upsilon \frac{\mathcal{U}^2 \text{Ri}}{\mathcal{L} \delta}. \quad (2.15)$$

The scaling of (2.9) without F_z gives:

$$\mathcal{O}(b_{\text{nh}}) = \frac{\mathcal{U}^2}{\mathcal{L}} \left(\Upsilon \delta + \frac{1}{\text{Ro}} \right). \quad (2.16)$$

With (2.15) and (2.16) the ratio (2.14) can finally be estimated as:

$$\mathcal{O} \left\{ \frac{p_{\text{nh}}}{p_{\text{hs}}} \right\} \approx \frac{\delta}{\text{Ri}} \left(\delta + \frac{1}{\Upsilon \text{Ro}} \right). \quad (2.17)$$

In most geophysical applications the aspect ratio δ is very small. The flows mainly take place in horizontal planes without significant vertical velocities. Strong stratification (large Richardson number Ri) also inhibits vertical motion. If furthermore the influence of earth rotation is sufficiently weak (sufficiently large Rossby number Ro), the nonhydrostatic pressure contribution becomes negligible:

$$\mathcal{O} \left\{ \frac{p_{nh}}{p_{hs}} \right\} \ll 1. \quad (2.18)$$

In this case the nonhydrostatic pressure contribution can only induce a significant pressure gradient force on sufficiently small scales. Since these are usually not resolved within large scale applications, the nonhydrostatic pressure contribution is simply neglected. This *hydrostatic pressure assumption* degenerates (2.1d) into (2.10a), whose integral (2.13) can directly be inserted into (2.1b) and (2.1c). The vertical velocity must now be diagnosed by vertically integrating (2.1a) to ensure a solenoidal velocity field:

$$w = w \Big|_{z=-H} - \int_{-H}^z \left(\frac{\partial u}{\partial x} + \frac{\partial v}{\partial y} \right) dz. \quad (2.19)$$

Since under the hydrostatic pressure assumption the Coriolis acceleration $f_h u$ in (2.1d) is neglected, $f_h w$ in (2.1b) must also be neglected to retain a fictitious Coriolis force. Even for not sufficiently large Rossby numbers this neglect of the Coriolis accelerations proportional to f_h is sustained (*traditional approximation*).

For many applications the hydrostatic pressure assumption is a satisfying approximation. Analytically it is exact only for strongly idealised flows. Neglecting nonlinear and viscous terms, the hydrostatic limit $\frac{\partial w}{\partial t} \rightarrow 0$ coincides with e. g. shallow water surface gravity waves (additionally neglecting all Coriolis terms) and near-inertial internal gravity waves in a continuously stratified fluid (additionally neglecting the nontraditional Coriolis terms).

2.3. Turbulence

Turbulence is a complex phenomenon in nature. Mathematically it can be modelled by coupled nonlinear differential equations (see e.g. Lorenz, 1963). The Navier-Stokes Equations (2.1a)–(2.1d) are coupled nonlinear partial differential equations, therefore they include turbulent effects (Foias et al., 2001). In this context, turbulent flows can be characterised by dominating nonlinearities in the equations. Since viscous effects damp turbulence, the ratio of nonlinear to viscous terms is a famous measure for turbulence, given by the Reynolds number (Reynolds, 1883). If the Reynolds number exceeds a critical value, the solution can become turbulent. This solution is usually chaotic and sensitive to disturbances.

The reasonability of a direct comparison of individual turbulent solutions is questionable. Furthermore, the turbulent solution describes stirring down to the viscous scales those Direct Numerical

Simulation (DNS) would require an impractical high spatio-temporal resolution. Therefore, several approaches for the description of only the resolvable mean flow are common.

Formally, all approaches are based on a general linear averaging operator $\langle \cdot \rangle$, decomposing every quantity into a mean part and a fluctuation. If this operator commutes with spatio-temporal derivatives, averaging of the Navier-Stokes Equations (2.1a)–(2.1d) yields identical equations for the mean parts, except for additional terms due to the nonlinearities (see Appendices A.1.2 and A.2.2). If the averaging operator commutes with spatio-temporal derivatives and is idempotent, it is called a Reynolds-Average¹. Only for Reynolds-Averages the additional turbulent terms in the Reynolds-Averaged-NSE (RANSE) can be derived as correlators of fluctuations. However, as shown by Germano (1992), the additional terms arising from non-idempotent averages can formally be treated in a similar way.

Following Pope (2000), in turbulent flows quantities behave like random variables and the averaging operator can be defined as the statistical mean. Theoretically, the random process is completely characterised by a multi-point joint probability density function. However, in real applications more practical averages must be used, that converge towards the statistical mean under certain conditions. For an ensemble of differently perturbed realisations an Ensemble-Average can be defined. The average of an ensemble of perturbed NSE yields prognostic equations for the ensemble-averaged quantities under ensemble-averaged initial and boundary conditions. The Ensemble-Average is a Reynolds-Average and converges to the statistical mean in the limit of an infinite number of realisations.

Both statistical approaches mentioned in the last paragraph remove turbulent flow patterns, which are only represented in an individual solution of the NSE. For one individual realisation the mean flow that is properly resolved within the used spatio-temporal resolution can be obtained by a filter. This Large-Eddy-Simulation (LES) can be viewed as an intermediate approach between the statistical approaches and DNS (Germano, 1992). If the mean flow within the filter interval is approximately homogeneous and stationary, the filter is approximately idempotent and converges to the statistical mean (Burchard, 2002a). However, especially near boundaries, filters may not commute with spatial derivatives and can introduce commutation errors (Geurts and Holm, 2006).

For all averages the additional terms in the averaged Navier-Stokes Equations, originating from the nonlinearities must be modelled accurately, because only due to these the effects of the fluctuations on the mean flow are incorporated. The closure of these additional terms is the key of turbulence modelling.

¹In the literature the term *Reynolds-Average* often is either exclusively identified with the Ensemble-Average or even with a temporal filter of sufficient filter width. Originally Reynolds (1895) proposed a spatial filter of sufficient filter width to approximate idempotency.

Chapter 3.

The General Estuarine Transport Model (GETM)

GETM is an open source coastal ocean model available from <http://www.getm.eu>. It solves the hydrostatic Navier-Stokes Equations under the Boussinesq approximation together with transport equations for potential temperature and salinity on C-staggered Finite Volumes in a horizontally curvilinear and an adaptive vertical mesh (Burchard and Bolding, 2002; Hofmeister et al., 2010). An explicit mode-splitting technique allows the efficient calculation of the free surface with drying and flooding in a depth-integrated module (Burchard et al., 2004). The baroclinic module contains various schemes for the calculation of the internal pressure gradient. Also for the baroclinic module a variety of advection schemes is implemented. As promoted by Pietrzak (1998), most of them are based on 1D TVD-schemes subsequently executed for each direction within a series of fractional steps. An interface to the external General Ocean Turbulence Model (GOTM, <http://www.gotm.net>) optionally provides state-of-the-art turbulence closures from Umlauf and Burchard (2005) for the vertical diffusivities. The modular FORTRAN-90 source code is optimised for parallelisation with MPI and OpenMP.

3.1. The governing equations of GETM

As outlined in Section 2.2.2, the hydrostatic pressure assumption simplifies the Navier-Stokes Equations (2.1a)–(2.1d) considerably. Turbulent motions can be optionally incorporated by turbulent stresses in terms of lateral and vertical eddy-viscosities (see Appendix A.1.2). In this context the governing equations are prognostic equations for the mean quantities and the brackets $\langle \cdot \rangle$ are omitted. DNS-like simulations can be performed by simply setting the turbulent viscosities to zero.

With the buoyancy b already defined in (2.12),

$$b = -\frac{\rho - \rho_0}{\rho_0}g, \quad (3.1)$$

the governing hydrodynamic equations of GETM can be formulated as:

$$0 = \frac{\partial u}{\partial x} + \frac{\partial v}{\partial y} + \frac{\partial w}{\partial z}, \quad (3.2a)$$

$$\begin{aligned} & \frac{\partial u}{\partial t} + \frac{\partial}{\partial x} \{uu\} + \frac{\partial}{\partial y} \{vu\} + \frac{\partial}{\partial z} \{wu\} - f_v v \\ &= - \frac{\partial}{\partial x} \left\{ \frac{p|_{z=\eta}}{\rho_0} \right\} - g \frac{\partial \eta}{\partial x} + \frac{\partial}{\partial x} \int_z^\eta b dz + \frac{\partial}{\partial z} \left\{ \left(\nu + \nu^{\text{turb},v} \right) \frac{\partial u}{\partial z} \right\} + F_x^h, \end{aligned} \quad (3.2b)$$

$$\begin{aligned} & \frac{\partial v}{\partial t} + \frac{\partial}{\partial x} \{uv\} + \frac{\partial}{\partial y} \{vv\} + \frac{\partial}{\partial z} \{wv\} + f_v u \\ &= - \frac{\partial}{\partial y} \left\{ \frac{p|_{z=\eta}}{\rho_0} \right\} - g \frac{\partial \eta}{\partial y} + \frac{\partial}{\partial y} \int_z^\eta b dz + \frac{\partial}{\partial z} \left\{ \left(\nu + \nu^{\text{turb},v} \right) \frac{\partial v}{\partial z} \right\} + F_y^h. \end{aligned} \quad (3.2c)$$

In (3.2b) and (3.2c) the forces obtained from the divergence of a deviatoric stress tensor are separated into lateral and vertical contributions with $(\nu, \nu^{\text{turb},h}, \nu^{\text{turb},v}) = \frac{1}{\rho_0} (\mu, \mu^{\text{turb},h}, \mu^{\text{turb},v})$ and with the molecular diffusivity of momentum ν assumed to be constant. The lateral contributions are also strongly simplified due to the hydrostatic pressure assumption (see Appendix A.1.2) and are given by

$$F_\alpha^h = \frac{\partial}{\partial x_\beta} \left\{ \nu \frac{\partial u_\alpha}{\partial x_\beta} \right\} + \frac{\partial}{\partial x_\beta} \left\{ 2\nu^{\text{turb},h} S_{\alpha\beta}(u, v) \right\}, \quad (3.3)$$

with the lateral deformation rate tensor

$$S_{\alpha\beta}(u, v) = \frac{1}{2} \left(\frac{\partial u_\alpha}{\partial x_\beta} + \frac{\partial u_\beta}{\partial x_\alpha} \right). \quad (3.4)$$

In (3.3) and in the following, summation is carried out over repeated indices with $\alpha, \beta \in \{x, y\}$ and $x_x = x$, $x_y = y$, $u_x = u$ and $u_y = v$.

3.2. Concepts

The utilisation of a numerical model and in particular its modification requires a detailed knowledge about the model concepts. In this Section the basic concepts of GETM are summarised. For more details the reader is referred to the original documentation (Burchard and Bolding, 2002; Burchard et al., 2013).

3.2.1. Transformation to general vertical coordinates and layer integration

For clarity in the present thesis a curvilinear transformation of the horizontal coordinates is not taken into account. However, the transformation to a general vertical coordinate s (Kasahara, 1974), representing the bottom topography with depth $H(x, y)$ and the free surface with elevation $\eta(x, y, t)$ by coordinate lines, is carried out. The vertical space is discretised into k_{\max} arbitrary layers with interfaces at $z_{k+1/2}(x, y, t)$ for $k \in [0, k_{\max}]$ and with $z_{1/2} = -H$ and $z_{k_{\max}+1/2} = \eta$. With layer heights $h_k = z_{k+1/2} - z_{k-1/2}$ and centre positions $z_k = \frac{1}{2}(z_{k-1/2} + z_{k+1/2})$ for $k \in [1, k_{\max}]$ layer-integrated equations can be derived (Burchard and Petersen, 1997). It should be noted that, unless denoted by $(\)_z$, due to the vertical coordinate transformation all partial derivatives refer to the same layer (to constant s) instead of to constant z .

With layer-averaged horizontal velocities (u_k, v_k) and the grid-related vertical velocity w^s the layer-integration of (3.2a)–(3.2c) yields:

$$0 = \frac{\partial h_k}{\partial t} + \frac{\partial}{\partial x} \{h_k u_k\} + \frac{\partial}{\partial y} \{h_k v_k\} + (w_{k+1/2}^s - w_{k-1/2}^s), \quad (3.5a)$$

$$\begin{aligned} & \frac{\partial}{\partial t} \{h_k u_k\} + \frac{\partial}{\partial x} \{h_k u_k u_k\} + \frac{\partial}{\partial y} \{h_k v_k u_k\} + (w_{k+1/2}^s u_{k+1/2} - w_{k-1/2}^s u_{k-1/2}) - f_v h_k v_k \\ &= -h_k \frac{\partial}{\partial x} \left\{ \frac{p|_{z=\eta}}{\rho_0} \right\} - h_k g \frac{\partial \eta}{\partial x} + (\tau_{x,k+1/2}(u, v) - \tau_{x,k-1/2}(u, v)) + h_k \tilde{F}_x^h(u_k, v_k, h_k) \\ &+ h_k F_{x,k}^{\text{IP}}(b), \end{aligned} \quad (3.5b)$$

$$\begin{aligned} & \frac{\partial}{\partial t} \{h_k v_k\} + \frac{\partial}{\partial x} \{h_k u_k v_k\} + \frac{\partial}{\partial y} \{h_k v_k v_k\} + (w_{k+1/2}^s v_{k+1/2} - w_{k-1/2}^s v_{k-1/2}) + f_v h_k u_k \\ &= -h_k \frac{\partial}{\partial y} \left\{ \frac{p|_{z=\eta}}{\rho_0} \right\} - h_k g \frac{\partial \eta}{\partial y} + (\tau_{y,k+1/2}(u, v) - \tau_{y,k-1/2}(u, v)) + h_k \tilde{F}_y^h(u_k, v_k, h_k) \\ &+ h_k F_{y,k}^{\text{IP}}(b). \end{aligned} \quad (3.5c)$$

In (3.5b) and (3.5c) the internal pressure gradient force is given by

$$F_{\alpha,k}^{\text{IP}}(b) = \frac{1}{h_k} \int_{z_{k-1/2}}^{z_{k+1/2}} \left(\frac{\partial}{\partial x_\alpha} \right)_z \int_z^\eta b dz' dz, \quad (3.6)$$

and is approximated in terms of the layer-averaged buoyancies b_k (see, e.g. Shchepetkin and McWilliams, 2003).

The vertical shear stresses are defined as

$$\tau_{\alpha,k+1/2}(u,v) = \begin{cases} \tau_{\alpha}^{\text{surf}}(u,v) & , k = k_{\text{max}} \\ \left(\nu + \nu_{k+1/2}^{\text{turb},v} \right) \frac{u_{\alpha,k+1} - u_{\alpha,k}}{z_{k+1} - z_k} & , k \in [1, k_{\text{max}} - 1] , \\ \tau_{\alpha}^{\text{bott}}(u,v) & , k = 0 \end{cases} \quad (3.7)$$

with $\tau_{\alpha}^{\text{surf}}$ obtained from the wind stress and with the bottom stress $\tau_{\alpha}^{\text{bott}}$ reconstructed from a logarithmic boundary profile of the velocity.

The lateral contributions of the stress tensor F_{α}^{h} are approximated according to Mellor and Blumberg (1985) and Kantha and Clayson (2000):

$$\tilde{F}_{\alpha}^{\text{h}}(u_k, v_k, h_k) = \frac{1}{h_k} \left[\frac{\partial}{\partial x_{\beta}} \left\{ h_k \nu \frac{\partial u_{\alpha,k}}{\partial x_{\beta}} \right\} + \frac{\partial}{\partial x_{\beta}} \left\{ h_k 2\nu^{\text{turb},h}(u_k, v_k) S_{\alpha\beta}(u_k, v_k) \right\} \right],$$

with $S_{\alpha\beta}$ given in (3.4) but evaluated with reference to the corresponding layer k (to constant s instead of to constant z).

Based on (2.2a) and (2.2b), the grid-related vertical velocity obeys the kinematic boundary conditions

$$w_{k_{\text{max}}+1/2}^{\text{s}} = 0, \quad (3.8a)$$

$$w_{1/2}^{\text{s}} = 0. \quad (3.8b)$$

In the hydrostatic model kernel the vertical velocity is only calculated for output and can be obtained from the discretised material derivative of the vertical position z :

$$w_k = \frac{1}{h_k} \left[\frac{\partial}{\partial t} \{ h_k z_k \} + \frac{\partial}{\partial x} \{ h_k u_k z_k \} + \frac{\partial}{\partial y} \{ h_k v_k z_k \} + \left(w_{k+1/2}^{\text{s}} z_{k+1/2} - w_{k-1/2}^{\text{s}} z_{k-1/2} \right) \right]. \quad (3.9)$$

3.2.2. Explicit mode-splitting

Due to the presence of a free surface, surface gravity waves are part of the numerical solution. This can be shown by summation of (3.5a)–(3.5c) over all layers with consideration of the kinematic boundary conditions (3.8a) and (3.8b) and $\sum_{k=1}^{k_{\max}} h_k = D(x, y, t) = -H(x, y) + \eta(x, y, t)$:

$$0 = \frac{\partial \eta}{\partial t} + \frac{\partial}{\partial x} \left\{ \sum_{k=1}^{k_{\max}} h_k u_k \right\} + \frac{\partial}{\partial y} \left\{ \sum_{k=1}^{k_{\max}} h_k v_k \right\}, \quad (3.10a)$$

$$\begin{aligned} & \frac{\partial}{\partial t} \left\{ \sum_{k=1}^{k_{\max}} h_k u_k \right\} + \frac{\partial}{\partial x} \left\{ \sum_{k=1}^{k_{\max}} h_k u_k u_k \right\} + \frac{\partial}{\partial y} \left\{ \sum_{k=1}^{k_{\max}} h_k v_k u_k \right\} - f_v \sum_{k=1}^{k_{\max}} h_k v_k \\ &= -D \frac{\partial}{\partial x} \left\{ \frac{p|_{z=\eta}}{\rho_0} \right\} - Dg \frac{\partial \eta}{\partial x} + \left(\tau_x^{\text{surf}}(u, v) - \tau_x^{\text{bott}}(u, v) \right) + \sum_{k=1}^{k_{\max}} h_k \tilde{F}_x^h(u_k, v_k, h_k) \\ &+ \sum_{k=1}^{k_{\max}} h_k F_{x,k}^{\text{IP}}(b) \end{aligned} \quad (3.10b)$$

$$\begin{aligned} & \frac{\partial}{\partial t} \left\{ \sum_{k=1}^{k_{\max}} h_k v_k \right\} + \frac{\partial}{\partial x} \left\{ \sum_{k=1}^{k_{\max}} h_k u_k v_k \right\} + \frac{\partial}{\partial y} \left\{ \sum_{k=1}^{k_{\max}} h_k v_k v_k \right\} + f_v \sum_{k=1}^{k_{\max}} h_k u_k \\ &= -D \frac{\partial}{\partial y} \left\{ \frac{p|_{z=\eta}}{\rho_0} \right\} - Dg \frac{\partial \eta}{\partial y} + \left(\tau_y^{\text{surf}}(u, v) - \tau_y^{\text{bott}}(u, v) \right) + \sum_{k=1}^{k_{\max}} h_k \tilde{F}_y^h(u_k, v_k, h_k) \\ &+ \sum_{k=1}^{k_{\max}} h_k F_{y,k}^{\text{IP}}(b) \end{aligned} \quad (3.10c)$$

Combination of (3.10a)–(3.10c) with only the blue terms considered and D assumed to be constant indeed yields a linear wave equation for η :

$$0 = \frac{\partial^2 \eta}{\partial t^2} - gD \left(\frac{\partial^2 \eta}{\partial x^2} + \frac{\partial^2 \eta}{\partial y^2} \right), \quad (3.11)$$

with the celerity of shallow-water surface gravity waves¹ $c = \sqrt{gD}$. Following Courant et al. (1928), an explicit temporal discretisation requires a time step Δt restricted by the CFL condition $\frac{c\Delta t}{\Delta x} \leq 1$

¹Deep-water surface gravity waves have been excluded due to the hydrostatic pressure assumption. Yet, even without this assumption, deep-water surface gravity waves are usually not resolved within the spatio-temporal resolution of an ocean model because of their short wavelengths and periods. Furthermore, the celerity of deep-water gravity waves is much smaller than that of shallow-water gravity waves and thus does not pose a more restrictive CFL condition.

and Δx being the discrete spatial resolution. Within an implicit temporal discretisation the time step is not restricted by this strong CFL condition. However, the computational and implementational effort of implicit discretisations, particularly in parallelised numerical models, is high. Furthermore, the prognostic equations for the 3D quantities can indeed be integrated within an explicit temporal discretisation and with a time step not restricted by the strong CFL condition in terms of $c = \sqrt{gD}$. Therefore, in GETM the governing equations are integrated within an explicit temporal discretisation, but are split into two modes.

Within the *2D-mode* the depth-integrated equations (3.10a)–(3.10c) are integrated with the *external time step* Δt_{2D} restricted by the strong CFL condition in terms of $c = \sqrt{gD}$. With the depth-averaged velocities

$$U_\alpha = \frac{1}{D} \sum_{k=1}^{k_{\max}} h_k u_{\alpha,k}, \quad (3.12)$$

these can be formulated as closed prognostic equations for η , $U = U_x$ and $V = U_y$:

$$0 = \frac{\partial \eta}{\partial t} + \frac{\partial}{\partial x} \{DU\} + \frac{\partial}{\partial y} \{DV\}, \quad (3.13a)$$

$$\begin{aligned} & \frac{\partial}{\partial t} \{DU\} + \frac{\partial}{\partial x} \{DUU\} + \frac{\partial}{\partial y} \{DVU\} - f_v DV \\ &= -D \frac{\partial}{\partial x} \left\{ \frac{p|_{z=\eta}}{\rho_0} \right\} - Dg \frac{\partial \eta}{\partial x} + \left(\tau_x^{\text{surf}}(U, V) - \tau_x^{\text{bott}}(U, V) \right) + D\tilde{F}_x^h(U, V, D) \\ & \quad - (S_x^A + S_x^B - S_x^D + S_x^F), \end{aligned} \quad (3.13b)$$

$$\begin{aligned} & \frac{\partial}{\partial t} \{DV\} + \frac{\partial}{\partial x} \{DUV\} + \frac{\partial}{\partial y} \{DVV\} + f_v DU \\ &= -D \frac{\partial}{\partial y} \left\{ \frac{p|_{z=\eta}}{\rho_0} \right\} - Dg \frac{\partial \eta}{\partial y} + \left(\tau_y^{\text{surf}}(U, V) - \tau_y^{\text{bott}}(U, V) \right) + D\tilde{F}_y^h(U, V, D) \\ & \quad - (S_y^A + S_y^B - S_y^D + S_y^F). \end{aligned} \quad (3.13c)$$

In (3.13b) and (3.13c) the interaction terms

$$S_{\alpha}^A = \left[\frac{\partial}{\partial x} \left\{ \sum_{k=1}^{k_{\max}} h_k u_k u_{\alpha,k} \right\} + \frac{\partial}{\partial y} \left\{ \sum_{k=1}^{k_{\max}} h_k v_k u_{\alpha,k} \right\} \right] - \left[\frac{\partial}{\partial x} \{DUU_{\alpha}\} + \frac{\partial}{\partial y} \{DVU_{\alpha}\} \right], \quad (3.14a)$$

$$S_{\alpha}^B = - \sum_{k=1}^{k_{\max}} h_k F_{\alpha,k}^{\text{IP}}(b), \quad (3.14b)$$

$$S_{\alpha}^D = \left[\sum_{k=1}^{k_{\max}} h_k \tilde{F}_{\alpha}^{\text{h}}(u_k, v_k, h_k) \right] - \left[D \tilde{F}_{\alpha}^{\text{h}}(U, V, D) \right] \quad (3.14c)$$

$$S_{\alpha}^F = \left[\tau_{\alpha}^{\text{surf}}(u, v) - \tau_{\alpha}^{\text{bott}}(u, v) \right] - \left[\tau_{\alpha}^{\text{surf}}(U, V) - \tau_{\alpha}^{\text{bott}}(U, V) \right], \quad (3.14d)$$

are only updated every *internal time step* $\Delta t_{3D} = M \Delta t_{2D}$ ($M \in \mathbb{N}$), subsequent to the integration of the prognostic equations (3.5a)–(3.5c) within the *3D-mode*. As mentioned above, the internal time step Δt_{3D} is not restricted by the strong CFL condition in terms of $c = \sqrt{gD}$ and usually offers $\mathcal{O}(M) = 10^1$.

3.2.3. Outline of the time loop

A consistent coupling of the 2D- and 3D-mode is guaranteed by the following time loop. The superscript (r) depicts the discrete value at time $t = r \Delta t_{3D}$ ($r \in \mathbb{R}$), e.g.

$$U^{(n+\frac{2m-1}{2M})} = U \Big|_{t=(n+\frac{2m-1}{2M})\Delta t_{3D}} = U \Big|_{t=n\Delta t_{3D} + \frac{2m-1}{2}\Delta t_{2D}}.$$

- time loop for $n = 0 : N - 1$:

1. Cycle of depth-averaged integrations for $m = 0 : M - 1$:

a) Integration of (3.13b) and (3.13c):

$$\begin{aligned} & \frac{(DU)^{\left(n+\frac{2m+1}{2M}\right)} - (DU)^{\left(n+\frac{2m-1}{2M}\right)}}{\Delta t_{2D}} \\ & = f^{DU} \left((U, V)^{\left(n+\frac{2m-1}{2M}\right)}, \eta^{\left(n+\frac{2m}{2M}\right)}, (S_x^A, S_x^D, S_x^F)^{(n-1/2)}, (S_x^B)^{(n)} \right), \end{aligned} \quad (3.15a)$$

$$\begin{aligned} & \frac{(DV)^{\left(n+\frac{2m+1}{2M}\right)} - (DV)^{\left(n+\frac{2m-1}{2M}\right)}}{\Delta t_{2D}} \\ & = f^{DV} \left((U, V)^{\left(n+\frac{2m-1}{2M}\right)}, \eta^{\left(n+\frac{2m}{2M}\right)}, (S_y^A, S_y^D, S_y^F)^{(n-1/2)}, (S_y^B)^{(n)} \right), \end{aligned} \quad (3.15b)$$

b) Integration of (3.13a):

$$\frac{\eta^{\left(n+\frac{2m+2}{2M}\right)} - \eta^{\left(n+\frac{2m}{2M}\right)}}{\Delta t_{2D}} = \frac{\partial}{\partial x} \left\{ (DU)^{\left(n+\frac{2m+1}{2M}\right)} \right\} + \frac{\partial}{\partial y} \left\{ (DV)^{\left(n+\frac{2m+1}{2M}\right)} \right\}, \quad (3.16)$$

c) Calculation of depth-averaged velocities $U_\alpha^{\left(n+\frac{2m+1}{2M}\right)} = \left(\frac{1}{D}\right) (DU_\alpha)^{\left(n+\frac{2m+1}{2M}\right)}$
with $D^{\left(n+\frac{2m+1}{2M}\right)} = \frac{1}{2} \left(D^{\left(n+\frac{2m}{2M}\right)} + D^{\left(n+\frac{2m+2}{2M}\right)} \right)$,

2. Calculation of mean depth-averaged velocities with $\bar{D}^{(n+1/2)} = \frac{1}{2} (D^{(n)} + D^{(n+1)})$:

$$\bar{U}^{(n+1/2)} = \frac{1}{\bar{D}^{(n+1/2)}} \left[\frac{1}{M} \sum_{m=0}^{M-1} (DU)^{\left(n+\frac{2m+1}{2M}\right)} \right], \quad (3.17a)$$

$$\bar{V}^{(n+1/2)} = \frac{1}{\bar{D}^{(n+1/2)}} \left[\frac{1}{M} \sum_{m=0}^{M-1} (DV)^{\left(n+\frac{2m+1}{2M}\right)} \right], \quad (3.17b)$$

3. Update of layer heights $h_k^{(n+1)}$ under constraint $\sum_{k=1}^{k_{\max}} h_k^{(n+1)} = D^{(n+1)}$ and calculation of $h_k^{(n+1/2)} = \frac{1}{2} (h_k^{(n)} + h_k^{(n+1)})$,

4. Integration of (3.5b) and (3.5c):

$$\frac{(h_k u_k)^{(*)} - (h_k u_k)^{(n-1/2)}}{\Delta t_{3D}} = f_k^{\text{hu}} \left((u, v, w^s)^{(n-1/2)}, \eta^{(n)} \right), \quad (3.18a)$$

$$\frac{(h_k v_k)^{(*)} - (h_k v_k)^{(n-1/2)}}{\Delta t_{3D}} = f_k^{\text{hv}} \left((u, v, w^s)^{(n-1/2)}, \eta^{(n)} \right), \quad (3.18b)$$

5. Shift of velocity profiles:

$$u_k^{(n+1/2)} = \frac{1}{h_k^{(n+1/2)}} (h_k u_k)^{(*)} - \left[\frac{1}{\bar{D}^{(n+1/2)}} \sum_{k=1}^{k_{\max}} (h_k u_k)^{(*)} - \bar{U}^{(n+1/2)} \right], \quad (3.19a)$$

$$v_k^{(n+1/2)} = \frac{1}{h_k^{(n+1/2)}} (h_k v_k)^{(*)} - \left[\frac{1}{\bar{D}^{(n+1/2)}} \sum_{k=1}^{k_{\max}} (h_k v_k)^{(*)} - \bar{V}^{(n+1/2)} \right], \quad (3.19b)$$

6. Update of the grid-related vertical velocity according to (3.5a):

$$w_{k-1/2}^{s,(n+1/2)} = \frac{h_k^{(n+1)} - h_k^{(n)}}{\Delta t_{3D}} + \frac{\partial}{\partial x} \left\{ (h_k u_k)^{(n+1/2)} \right\} + \frac{\partial}{\partial y} \left\{ (h_k v_k)^{(n+1/2)} \right\} + w_{k+1/2}^{s,(n+1/2)}, \quad (3.20)$$

7. Integration of tracer equations from (n) to $(n+1)$ in terms of $(u, v, w^s)^{(n+1/2)}$ and update of buoyancy $b^{(n+1)}$,
8. Update of interaction terms $(S_\alpha^A, S_\alpha^D, S_\alpha^F)^{(n+1/2)}$ and $(S_\alpha^B)^{(n+1)}$ (3.14a)–(3.14d) in terms of $(u, v)^{(n+1/2)}$, $(\bar{U}, \bar{V})^{(n+1/2)}$ and $b^{(n+1)}$,

The key elements for the consistent coupling of the 2D- and 3D-mode are the use of accurate interaction terms² and the shift of the velocity profiles (3.19a) and (3.19b). The former incorporates missing 3D dynamics into the 2D-mode, the latter guarantees

$$\begin{aligned}
 \frac{\eta^{(n+1)} - \eta^{(n)}}{M\Delta t_{2D}} &= \frac{1}{M} \sum_{m=0}^{M-1} \frac{\eta^{(n+\frac{2m+2}{2M})} - \eta^{(n+\frac{2m}{2M})}}{\Delta t_{2D}} \\
 &\stackrel{(3.16)}{=} \frac{1}{M} \sum_{m=0}^{M-1} \left[\frac{\partial}{\partial x} \left\{ (DU)^{(n+\frac{2m+1}{2M})} \right\} + \frac{\partial}{\partial y} \left\{ (DV)^{(n+\frac{2m+1}{2M})} \right\} \right] \\
 &\stackrel{(3.17a),(3.17b)}{=} \frac{\partial}{\partial x} \left\{ (\overline{DU})^{(n+1/2)} \right\} + \frac{\partial}{\partial y} \left\{ (\overline{DV})^{(n+1/2)} \right\} \\
 &\stackrel{(3.19a),(3.19b)}{=} \frac{\partial}{\partial x} \left\{ \sum_{k=1}^{k_{\max}} (h_k u_k)^{(n+1/2)} \right\} + \frac{\partial}{\partial y} \left\{ \sum_{k=1}^{k_{\max}} (h_k v_k)^{(n+1/2)} \right\} \\
 &\stackrel{(3.20)}{=} \sum_{k=1}^{k_{\max}} \frac{h_k^{(n+1)} - h_k^{(n)}}{\Delta t_{3D}} \\
 &= \frac{\eta^{(n+1)} - \eta^{(n)}}{\Delta t_{3D}}.
 \end{aligned}$$

²In the official GETM code $(S_{\alpha}^B)^{(n+1)}$ is calculated in terms of $b^{(n)}$. For the simulations in the present thesis this inaccurate treatment is changed as described in the time loop.

Chapter 4.

Analysis of spurious dissipation and mixing

It is well known, that in numerical models the advective transport relative to fixed or moving grids needs to be discretised with sufficient accuracy to minimise the spurious decay of tracer variance (spurious mixing). In this Chapter a general analysis of discrete variance decay (DVD) caused by advective and diffusive fluxes is established. In the lack of a general closed derivation for the local DVD rate, two noninvasive methods to quantify local DVD during model runtime are discussed. Whereas the first was presented recently by Burchard and Rennau (2008), the second is a newly proposed alternative. This alternative analysis method is shown to have a sound foundation, missing limitations and a much better runtime performance. The diagnosed DVD can be separated into physical and numerical (spurious) contributions, with the latter originating from discretisation errors. Based on the DVD analysis, a 3D dissipation analysis is developed to quantify the physically and numerically induced loss of kinetic energy and thereby providing a missing piece of information to assess the energy conservation of an ocean model. The mixing and dissipation analyses are performed and evaluated for three test cases, with complexities ranging from idealised 1D advection to a realistic ocean modelling application to the Western Baltic Sea. In all test cases the proposed alternative DVD analysis method is demonstrated to provide a reliable diagnostic tool for the local quantification of physically and numerically induced dissipation and mixing.

4.1. Introduction

Discretisation errors in ocean models can cause the numerical solution to violate basic conservation properties of the continuous solution. The spatial discretisation by means of Finite Volumes (FVs) offers the straightforward development of numerical schemes conserving global first moments. However, even in the absence of diffusion, in general these schemes do not conserve global second moments (*variance*). Starting with the seminal work of Arakawa (1966), constraints on the discrete advection term were derived to prevent spurious decay of variance. The disbenefit of the resulting schemes was only second-order spatial accuracy and oscillations in the obtained solution (Shchepetkin and McWilliams, 1998). In contrast, TVD-schemes, systematically introduced to the ocean modelling community by Pietrzak (1998), are nonoscillatory, can be of higher-order spatial accuracy, but do not conserve variance.

The local quantification of spurious variance decay is essential for a detailed assessment of numerical models. For advection schemes based on the explicit first-order upstream (FOU) scheme Morales Maqueda and Holloway (2006) quantified the local variance decay as the variance destroyed by the final recombination of advected subvolumes inside one FV-cell. Based on this definition, Morales Maqueda and Holloway (2006) could analytically deduce the well-known numerical diffusivity of the explicit FOU scheme for uniform 1D flow. Also in 1D they calculated the spurious variance decay of the SOM-scheme (Prather, 1986).

Burchard and Rennau (2008) generalised an alternative derivation for the local variance decay rate of the 1D explicit FOU scheme given in a footnote in Morales Maqueda and Holloway (2006). The so developed diagnostic method can be applied to any 3D advection scheme and provided valuable insight into the local strength and origin of spurious decay of tracer variance (*spurious mixing*) in realistic ocean modelling applications (Rennau and Burchard, 2009; Hofmeister et al., 2011). Thereby it promoted the systematic development and assessment of new numerical techniques reducing spurious mixing, e.g. adaptive vertical grids (Hofmeister et al., 2010; Gräwe et al., in prep.). Recently, Burchard (2012) demonstrated the application of the developed variance method to quantify spurious decay of velocity variance (*spurious dissipation*) in 1D.

In this Chapter the diagnostic method of Burchard and Rennau (2008) is reviewed in the light of a general analysis of DVD. In this context, deficiencies of the method are identified and an alternative method for quantifying DVD is presented. Furthermore, the concept of the 1D dissipation analysis is extended to 3D for a staggered arrangement of velocity components.

In Section 4.2 the theoretical foundations of AVD and DVD are provided and the two different methods to quantify DVD are presented and discussed in detail. Based on these methods, the 3D dissipation analysis is developed. In Section 4.3 mixing and dissipation analyses are performed and evaluated for three test cases, with complexities ranging from idealised 1D advection to a realistic ocean modelling application. Conclusions and an outlook are given in Section 4.4. In B.1 additional information about the applied TVD-schemes is provided. Details about the closed derivation of DVD for the 1D diffusion scheme and the explicit FOU scheme are given in B.2 and B.3. As a further proof of concept, in B.4 the alternative DVD analysis method is presented as a consistent extension of the physically sound definition of local DVD by Morales Maqueda and Holloway (2006).

4.2. Basics

Starting from the analytical 1D transport equation, in Section 4.2.1 the AVD rate is derived as a measure for diffusion. By means of the discretised 1D transport equation, two different methods for quantifying DVD are presented in Section 4.2.2. Details about their extension to 3D and their implementation into ocean models are provided in Section 4.2.3. Based on these 3D DVD analysis methods, in Section 4.2.4 a method for quantifying the dissipation of kinetic energy in ocean models with a staggered arrangement of velocity components is developed.

4.2.1. Analytical variance decay (AVD)

Under the Boussinesq approximation the 1D transport equation describes the local temporal change of an arbitrary specific¹ quantity φ due to advective and diffusive fluxes, given in terms of velocity u and diffusivity ν , respectively:

$$\frac{\partial \varphi}{\partial t} + \frac{\partial}{\partial x} \left\{ u\varphi - \nu \frac{\partial \varphi}{\partial x} \right\} = 0. \quad (4.1)$$

¹A *specific* quantity φ is measured on *per mass* basis, i.e. $\varphi = 1$ for mass or $\varphi = u$ for momentum.

Multiplication of (4.1) with 2φ and use of the incompressibility constraint $\frac{\partial u}{\partial x} = 0$ (obtained from (4.1) for $\varphi = 1$) yields a similar prognostic equation for the second moment, but with a sink term originating exclusively in the diffusion of φ :

$$\frac{\partial (\varphi^2)}{\partial t} + \frac{\partial}{\partial x} \left\{ u (\varphi^2) - \nu \frac{\partial (\varphi^2)}{\partial x} \right\} = -2\nu \left(\frac{\partial \varphi}{\partial x} \right)^2. \quad (4.2)$$

The sink term on the right-hand side of (4.2) is a measure for the redistribution of φ due to diffusion. In a closed or periodic domain with volume V and the global mean $\langle \cdot \rangle_V = \frac{1}{V} \int_V \cdot dV$, (4.1) conserves the global first moment $\langle \varphi \rangle_V$ and the *global AVD rate* $-\frac{\partial}{\partial t} \{ \sigma_V^2 \}$ can be derived as:

$$\begin{aligned} -\frac{\partial}{\partial t} \{ \sigma_V^2(\varphi) \} &= -\frac{\partial}{\partial t} \left\{ \langle \varphi^2 \rangle_V - \langle \varphi \rangle_V^2 \right\} \\ &\stackrel{(4.1)}{=} -\frac{\partial}{\partial t} \langle \varphi^2 \rangle_V \\ &\stackrel{(4.2)}{=} \left\langle 2\nu \left(\frac{\partial \varphi}{\partial x} \right)^2 \right\rangle_V. \end{aligned} \quad (4.3)$$

Therefore, the sink on the right-hand side of (4.2) will be denoted as the *local AVD rate* χ^{ana} :

$$\chi^{\text{ana}}(\varphi) = 2\nu \left(\frac{\partial \varphi}{\partial x} \right)^2 \geq 0. \quad (4.4)$$

4.2.2. Discrete variance decay (DVD)

A conservative FV-discretisation of the 1D transport equation (4.1) can be obtained by integration over one FV-cell,

$$\frac{V_i^{(n+1)} \varphi_i^{(n+1)} - V_i^{(n)} \varphi_i^{(n)}}{\Delta t} + \left[A_{i'} \left(u_{i'} \tilde{\varphi}_{i'} - \frac{\nu_{i'}}{\Delta x_{i'}} \overline{[\varphi_{i*}]_{i*=i'-1/2}^{i*=i'+1/2}} \right) \right]_{i'=i-1/2}^{i'=i+1/2} = 0, \quad (4.5)$$

with $V_i^{(n)}$ as the volume of the i -th FV-cell at time level (n) and the discrete first moment $\varphi_i^{(n)} = \frac{1}{V_i^{(n)}} \int_{V_i^{(n)}} \varphi^{(n)} dV$. The rectangular brackets $[X_{i'}]_{i'=i-1/2}^{i'=i+1/2} = X_{i+1/2} - X_{i-1/2}$ originally stem

from the surface integral but are also used as shorthand notation for differences originating from gradients. Quantities with half indices are located at the corresponding interface between two FV-cells, e.g. the area of the interface $A_{i'}$ and the distance between the two adjacent cell centres $\Delta x_{i'}$. The effective interfacial values $\tilde{\varphi}_{i'}$ are approximated from the discrete values φ_i , depending on the applied advection scheme. The gradients $[\varphi_{i*}]_{i*=i'-1/2}^{i*=i'+1/2}$ setting up the diffusive fluxes may contain explicit and implicit contributions.

In a closed or periodic domain with volume V and the discrete global mean $\langle \cdot \rangle_V^{(n+1)} = \frac{1}{V} \sum_i V_i^{(n+1)} (\cdot)_i$, the FV-discretisation (4.5) indeed guarantees the conservation of the global first moment:

$$\langle \varphi^{(n+1)} \rangle_V^{(n+1)} \equiv \langle \varphi^{(n)} \rangle_V^{(n)}. \quad (4.6)$$

In contrast, due the presence of diffusive fluxes and discretisation errors of the advective fluxes the global second moment $\langle (\varphi^{(n)})^2 \rangle_V^{(n)}$ will in general not be conserved. James (1996) quantified the cumulative global loss of discrete second moment in terms of the ratio $\langle (\varphi^{(n+1)})^2 \rangle_V^{(n+1)} / \langle (\varphi^{(0)})^2 \rangle_V^{(0)}$. Alternatively, and in analogy to the global AVD rate (4.3), the global loss of discrete second moment can be quantified in terms of the *global DVD rate*:

$$\begin{aligned} -\frac{(\Delta\sigma^2)_V^{(n+1)}(\varphi)}{\Delta t} &= -\frac{1}{\Delta t} \left\{ \left[\langle (\varphi^{(n+1)})^2 \rangle_V^{(n+1)} - \left(\langle \varphi^{(n+1)} \rangle_V^{(n+1)} \right)^2 \right] \right. \\ &\quad \left. - \left[\langle (\varphi^{(n)})^2 \rangle_V^{(n)} - \left(\langle \varphi^{(n)} \rangle_V^{(n)} \right)^2 \right] \right\} \\ &\stackrel{(4.6)}{=} -\frac{1}{\Delta t} \left\{ \langle (\varphi^{(n+1)})^2 \rangle_V^{(n+1)} - \langle (\varphi^{(n)})^2 \rangle_V^{(n)} \right\}. \end{aligned} \quad (4.7)$$

However, this global measure does not provide any information on the spatial distribution of DVD and it fails for domains with open boundaries. Therefore, analogous to the local AVD rate (4.4), a *local DVD rate* $\chi_i^{(n+1)}$ with

$$\langle \chi^{(n+1)} \rangle_V^{(n+1)} \equiv -\frac{(\Delta\sigma^2)_V^{(n+1)}}{\Delta t} \quad (4.8)$$

is needed.

Ideally, and in analogy to the analytical case presented in Section 4.2.1, $\chi_i^{(n+1)}$ associated with the transport of $\varphi_i^{(n)}$ according to (4.5) should be deducible from the prognostic equation for $(\varphi_i^{(n+1)})^2$.

For consistency of the discretised quantities the associated prognostic equation for $(\varphi_i^{(n+1)})^2$ must be derived from the transport equation for the discrete first moment (4.5) and cannot be obtained from an independent discretisation of the analytical prognostic equation for the second moment (4.2).

Unfortunately, a closed derivation of the prognostic equation for $(\varphi_i^{(n+1)})^2$ and thus $\chi_i^{(n+1)}$ can only be carried out for rather trivial cases.

1D diffusion (for details see Appendix B.2) In the context of a conservative discretisation of the production term for turbulent kinetic energy, Burchard (2002b) derived a closed expression for $\chi_i^{(n+1)}$ associated with the 1D diffusion scheme temporally discretised by the θ -method. As derived in detail in (B.11), the corresponding $\chi_i^{(n+1)}$ could be deduced from the following prognostic equation for $(\varphi_i^{(n+1)})^2$:

$$\chi_i^{\text{diff},(n+1)} = -\frac{1}{V_i} \left(\frac{V_i (\varphi_i^{(n+1)})^2 - V_i (\varphi_i^{(n)})^2}{\Delta t} - \left[A_{i'} \frac{\nu_{i'}}{\Delta x_{i'}} \left[\theta (\varphi_{i_*}^{(n+1)})^2 + (1-\theta) (\varphi_{i_*}^{(n)})^2 \right]_{i_*=i'-1/2}^{i_*=i'+1/2} \right]_{i'=i-1/2}^{i'=i+1/2} \right). \quad (4.9)$$

1D explicit first-order upstream (FOU) scheme (for details see Appendix B.3) The derivation for the 1D explicit FOU scheme was mentioned in a footnote in Morales Maqueda and Holloway (2006). Burchard (2012) presented its generalisation for the depth-integrated 1D scheme. According to (B.14), the associated prognostic equation for $(\varphi_i^{(n+1)})^2$ can be derived as

$$\chi_i^{\text{FOU},(n+1)} = -\frac{1}{V_i^{(n+1)}} \left(\frac{V_i^{(n+1)} (\varphi_i^{(n+1)})^2 - V_i^{(n)} (\varphi_i^{(n)})^2}{\Delta t} + \left[A_{i'} u_{i'} (\tilde{\varphi}_{i'})^2 \right]_{i'=i-1/2}^{i'=i+1/2} \right). \quad (4.10)$$

In the lack of a general closed derivation, the local DVD rate may be alternatively defined as

$$\chi_i^{(n+1)}(\varphi) = \frac{(\hat{\varphi}^2)_i^{(n+1)} - (\varphi_i^{(n+1)})^2}{\Delta t}, \quad (4.11)$$

with $(\varphi_i^{(n+1)})^2$ being the actual discrete second moment and $(\hat{\varphi}^2)_i^{(n+1)}$ representing an expected target second moment consistent with the transported $\varphi_i^{(n)}$. The expected target second moment is not uniquely determined and due to (4.8) only constrained by

$$\left\langle (\hat{\varphi}^2)^{(n+1)} \right\rangle_V^{(n+1)} \equiv \left\langle (\varphi^{(n)})^2 \right\rangle_V^{(n)}. \quad (4.12)$$

In this Chapter the DVD analyses will be performed with two reasonable choices for $(\hat{\varphi}^2)^{(n+1)}$ discussed in the following.

4.2.2.1. The DVD analysis method of Burchard and Rennau (2008, BR08)

Although originally intended to only quantify spurious variance decay of advection schemes, the analysis method developed by Burchard and Rennau (2008) can in principle be performed for a general transport scheme \mathcal{T} defined by

$$\mathcal{T}\{\varphi\}_i^{(n+1)} = \frac{1}{V_i^{(n+1)}} \left(V_i^{(n)} \varphi_i - \Delta t \left[A_{i'} \left(u_{i'} \tilde{\varphi}_{i'} - \frac{\nu_{i'}}{\Delta x_{i'}} \overline{[\varphi_{i*}]_{i*=i'-1/2}^{i*=i'+1/2}} \right) \right]_{i'=i-1/2}^{i'=i+1/2} \right). \quad (4.13)$$

If the discrete first moment is obtained as $\varphi_i^{(n+1)} = \mathcal{T}\{\varphi^{(n)}\}_i^{(n+1)}$, Burchard and Rennau (2008) proposed to estimate the associated transport of $(\varphi_i^{(n)})^2$ in terms of the same transport scheme:

$$\begin{aligned} (\hat{\varphi}^2)_i^{\text{BR08},(n+1)} &= \mathcal{T} \left\{ (\varphi^{(n)})^2 \right\}_i^{(n+1)} \\ &= \frac{1}{V_i^{(n+1)}} \left(V_i^{(n)} (\varphi_i^{(n)})^2 - \Delta t \left[A_{i'} \left(u_{i'} \overline{(\varphi^2)_{i'}} - \frac{\nu_{i'}}{\Delta x_{i'}} \overline{[(\varphi^2)_{i*}]_{i*=i'-1/2}^{i*=i'+1/2}} \right) \right]_{i'=i-1/2}^{i'=i+1/2} \right). \end{aligned} \quad (4.14)$$

Indeed, since the transport of $(\varphi_i^{(n)})^2$ according to (4.14) is conservative, the constraint (4.8) is fulfilled. Furthermore, for the explicit FOU scheme the combination of (4.14) and (4.11) reproduces $\chi_i^{\text{FOU},(n+1)}$ derived in (4.10). However, the implicit contributions to the diffusive fluxes in (4.14) are given by $\theta (\varphi^2)_{i*}^{(n+1)}$ instead of $\theta (\varphi_{i*}^{(n+1)})^2$ as in (4.9), indicating a limitation to explicit transport schemes.

The outlined analysis method is easily extended to 3D, if $(\hat{\varphi}^2)^{\text{BR08}}$ is defined in terms of the utilised 3D transport scheme. In this context Burchard and Gräwe (2013) questioned the validity of the analysis for schemes based on fractional steps. However, in the lack of a general closed derivation, the corresponding choice for $(\hat{\varphi}^2)^{\text{BR08}}$ seems to be still reasonable.

In fact, the concerns raised by Burchard and Gräwe (2013) should be discussed in a general context, already affecting the 1D analysis. The central issue to be questioned is, whether $(\hat{\varphi}^2)^{\text{BR08},(n+1)}$ does sufficiently represent the transport of $(\varphi^{(n)})^2$ associated with the transport of $\varphi^{(n)}$ according to (4.5). The utilisation of “the same transport scheme” only implies identical algorithms for approximating the effective interfacial values and for splitting the prognostic integration. However, the fluxes actually used in (4.14) are not directly linked to the ones used in (4.5). This missing relation between the fluxes motivates an alternative choice for the expected target second moment $\hat{\varphi}^2$.

4.2.2.2. An alternative DVD analysis method (K13)

The expected target second moment $(\hat{\varphi}^2)^{\text{BR08}}$ defined in (4.14) can be equivalently obtained as a discrete analogue to the analytical prognostic equation for the second moment (4.2) without sink term. However, as argued in the preceding Section, (4.14) is actually independent from the transport equation for the discrete first moment (4.5). In contrast, an alternative discretisation of (4.2) without sink term may be obtained with the fluxes of second moment explicitly defined in terms of the fluxes of first moment used in (4.5):

$$(\hat{\varphi}^2)_i^{\text{K13},(n+1)} = \frac{1}{V_i^{(n+1)}} \left(V_i^{(n)} (\varphi_i^{(n)})^2 - \Delta t \left[A_{i'} \left(u_{i'} (\tilde{\varphi}_{i'})^2 - \frac{\nu_{i'}}{\Delta x_{i'}} \left[(\varphi_{i_*})^2 \right]_{i_*=i'-1/2}^{i_*=i'+1/2} \right) \right]_{i'=i-1/2}^{i'=i+1/2} \right). \quad (4.15)$$

With $J_{i'}^{\text{adv}}(\varphi) = u_{i'} \tilde{\varphi}_{i'}$ and $J_{i'}^{\text{diff}}(\varphi) = -\frac{\nu_{i'}}{\Delta x_{i'}} [\varphi_{i_*}]_{i_*=i'-1/2}^{i_*=i'+1/2}$ being the advective and diffusive fluxes of first moment in (4.5), the corresponding fluxes in (4.15) are defined as $J_{i'}^{\text{adv}}(\varphi^2) = \tilde{\varphi}_{i'} J_{i'}^{\text{adv}}(\varphi)$ and $J_{i'}^{\text{diff}}(\varphi^2) = 2\frac{1}{2} (\varphi_{i'-1/2} + \varphi_{i'+1/2}) J_{i'}^{\text{diff}}(\varphi)$. The factor 2 in the latter originates from the discretisation of $2\varphi\nu\frac{\partial\varphi}{\partial x}$ instead of $\nu\frac{\partial}{\partial x}(\varphi^2)$ in (4.2). This difference does not matter for 1D diffusion, but will be important for the anisotropic 3D diffusion of momentum discussed in Section 4.2.4. With these fluxes the transported second moment is directly associated with the transported first moment, also for implicit and nonlinear schemes and for schemes based on fractional steps. Furthermore, (4.15) is consistent with the constraint (4.12) and the closed derivations for the 1D diffusion scheme (4.9) and the explicit FOU scheme (4.10).

4.2.3. Implementation into 3D ocean models

4.2.3.1. The 3D DVD analysis method of Burchard and Rennau (2008, BR08)

As already mentioned in Section 4.2.2.1 and presented by Burchard and Rennau (2008), the analysis method based on $(\hat{\varphi}^2)^{\text{BR08}}$ is easily applied in 3D, if the 1D transport scheme $\mathcal{T}\{\cdot\}_i$ in (4.14) is replaced by a 3D transport scheme $\mathcal{T}\{\cdot\}_{i,j,k}$. After the independent transport of $\varphi^{(n)}$ and $(\varphi^{(n)})^2$ the DVD rate $\chi^{\text{BR08},(n+1)}(\varphi)$ can be diagnosed from

$$\chi_{i,j,k}^{\text{BR08,(n+1)}}(\varphi) = \frac{\mathcal{T}\left\{(\varphi^{(n)})^2\right\}_{i,j,k}^{(n+1)} - \left(\mathcal{T}\left\{\varphi^{(n)}\right\}_{i,j,k}^{(n+1)}\right)^2}{\Delta t}. \quad (4.16)$$

The analysis method of Burchard and Rennau (2008) requires only minimal implementational effort, viz an additional call to the modular transport routine with $(\varphi^{(n)})^2$ and a final loop to calculate $\chi^{\text{BR08,(n+1)}}(\varphi)$ by means of (4.16). In contrast, the runtime overhead is high. Most of it originates from the additional advection of $(\varphi^{(n)})^2$, for common higher-order directional-split schemes dramatically increasing the communication between subdomains of parallelised model configurations.

4.2.3.2. The 3D extension of the alternative DVD analysis method (K13)

The extension of the alternative analysis method proposed in Section 4.2.2.2 to 3D is straightforward by simply considering the fluxes through the additional interfaces of the FV-cell in (4.15) to define $(\hat{\varphi}^2)_{i,j,k}^{\text{K13,(n+1)}}$. Since the fluxes used for the transport of $(\varphi^{(n)})^2$ are defined in terms of quantities calculated during the transport of $\varphi^{(n)}$, the quantification of DVD should be implemented directly in the transport routines where these quantities are available. If the integration is carried out in fractional steps (e.g., directional split and split into advection and diffusion), the overall DVD rate χ^{K13} can be obtained as the conservative sum of the individual DVD rates calculated within each step. As an example, a common directional Strang-splitting (Strang, 1968) of the advection equation is outlined:

$$\frac{V_{i,j,k}^{(n+1/5)} \varphi_{i,j,k}^{(n+1/5)} - V_{i,j,k}^{(n)} \varphi_{i,j,k}^{(n)}}{\Delta t} + \frac{1}{2} \left[A_{i',j,k} u_{i',j,k} \widetilde{\varphi^{(n)}}_{i',j,k} \right]_{i'=i-1/2}^{i'=i+1/2} = 0, \quad (4.17a)$$

$$\frac{V_{i,j,k}^{(n+2/5)} \varphi_{i,j,k}^{(n+2/5)} - V_{i,j,k}^{(n+1/5)} \varphi_{i,j,k}^{(n+1/5)}}{\Delta t} + \frac{1}{2} \left[A_{i,j',k} v_{i,j',k} \widetilde{\varphi^{(n+1/5)}}_{i,j',k} \right]_{j'=j-1/2}^{j'=j+1/2} = 0, \quad (4.17b)$$

$$\frac{V_{i,j,k}^{(n+3/5)} \varphi_{i,j,k}^{(n+3/5)} - V_{i,j,k}^{(n+2/5)} \varphi_{i,j,k}^{(n+2/5)}}{\Delta t} + \left[A_{i,j,k'} w_{i,j,k'} \widetilde{\varphi^{(n+2/5)}}_{i,j,k'} \right]_{k'=k-1/2}^{k'=k+1/2} = 0, \quad (4.17c)$$

$$\frac{V_{i,j,k}^{(n+4/5)} \varphi_{i,j,k}^{(n+4/5)} - V_{i,j,k}^{(n+3/5)} \varphi_{i,j,k}^{(n+3/5)}}{\Delta t} + \frac{1}{2} \left[A_{i,j',k} v_{i,j',k} \widetilde{\varphi^{(n+3/5)}}_{i,j',k} \right]_{j'=j-1/2}^{j'=j+1/2} = 0, \quad (4.17d)$$

$$\frac{V_{i,j,k}^{(n+1)} \varphi_{i,j,k}^{(n+1)} - V_{i,j,k}^{(n+4/5)} \varphi_{i,j,k}^{(n+4/5)}}{\Delta t} + \frac{1}{2} \left[A_{i',j,k} u_{i',j,k} \widetilde{\varphi^{(n+4/5)}}_{i',j,k} \right]_{i'=i-1/2}^{i'=i+1/2} = 0. \quad (4.17e)$$

Based on (4.11) and (4.15) the individual DVD rates associated with (4.17a)–(4.17e) are given by:

$$\chi_{i,j,k}^{n \rightarrow n+1/5} = -\frac{1}{V_{i,j,k}^{(n+1/5)}} \left(\frac{V_{i,j,k}^{(n+1/5)} \left(\varphi_{i,j,k}^{(n+1/5)} \right)^2 - V_{i,j,k}^{(n)} \left(\varphi_{i,j,k}^{(n)} \right)^2}{\Delta t} + \frac{1}{2} \left[A_{i',j,k} u_{i',j,k} \left(\widetilde{\varphi}_{i',j,k}^{(n)} \right)^2 \right]_{i'=i-1/2}^{i'=i+1/2} \right), \quad (4.18a)$$

$$\chi_{i,j,k}^{n+1/5 \rightarrow n+2/5} = -\frac{1}{V_{i,j,k}^{(n+2/5)}} \left(\frac{V_{i,j,k}^{(n+2/5)} \left(\varphi_{i,j,k}^{(n+2/5)} \right)^2 - V_{i,j,k}^{(n+1/5)} \left(\varphi_{i,j,k}^{(n+1/5)} \right)^2}{\Delta t} + \frac{1}{2} \left[A_{i,j',k} v_{i,j',k} \left(\widetilde{\varphi}_{i,j',k}^{(n+1/5)} \right)^2 \right]_{j'=j-1/2}^{j'=j+1/2} \right), \quad (4.18b)$$

$$\chi_{i,j,k}^{n+2/5 \rightarrow n+3/5} = -\frac{1}{V_{i,j,k}^{(n+3/5)}} \left(\frac{V_{i,j,k}^{(n+3/5)} \left(\varphi_{i,j,k}^{(n+3/5)} \right)^2 - V_{i,j,k}^{(n+2/5)} \left(\varphi_{i,j,k}^{(n+2/5)} \right)^2}{\Delta t} + \left[A_{i,j,k'} w_{i,j,k'} \left(\widetilde{\varphi}_{i,j,k'}^{(n+2/5)} \right)^2 \right]_{k'=k-1/2}^{k'=k+1/2} \right), \quad (4.18c)$$

$$\chi_{i,j,k}^{n+3/5 \rightarrow n+4/5} = -\frac{1}{V_{i,j,k}^{(n+4/5)}} \left(\frac{V_{i,j,k}^{(n+4/5)} \left(\varphi_{i,j,k}^{(n+4/5)} \right)^2 - V_{i,j,k}^{(n+3/5)} \left(\varphi_{i,j,k}^{(n+3/5)} \right)^2}{\Delta t} + \frac{1}{2} \left[A_{i,j',k} v_{i,j',k} \left(\widetilde{\varphi}_{i,j',k}^{(n+3/5)} \right)^2 \right]_{j'=j-1/2}^{j'=j+1/2} \right), \quad (4.18d)$$

$$\chi_{i,j,k}^{n+4/5 \rightarrow n+1} = -\frac{1}{V_{i,j,k}^{(n+1)}} \left(\frac{V_{i,j,k}^{(n+1)} \left(\varphi_{i,j,k}^{(n+1)} \right)^2 - V_{i,j,k}^{(n+4/5)} \left(\varphi_{i,j,k}^{(n+4/5)} \right)^2}{\Delta t} + \frac{1}{2} \left[A_{i',j,k} u_{i',j,k} \left(\widetilde{\varphi}_{i',j,k}^{(n+4/5)} \right)^2 \right]_{i'=i-1/2}^{i'=i+1/2} \right). \quad (4.18e)$$

The overall DVD rate consistent with (4.11) can be obtained as:

$$\chi_{i,j,k}^{\text{K13},(n+1)}(\varphi) = \frac{\left(\widehat{\varphi}^2 \right)_{i,j,k}^{\text{K13},(n+1)} - \left(\varphi_{i,j,k}^{(n+1)} \right)^2}{\Delta t} = \frac{1}{V_{i,j,k}^{(n+1)}} \sum_{m=1}^5 V_{i,j,k}^{(n+m/5)} \chi_{i,j,k}^{n+(m-1)/5 \rightarrow n+m/5}. \quad (4.19)$$

Although the calculation of individual DVD rates directly within the transport routines slightly increases the implementational effort, the runtime performance of the model is only marginally affected by the alternative analysis method, because no additional communication between subdomains is required.

The directional split scheme (4.17a)–(4.17e) does not utilise cross-fluxes. However, the alternative analysis method can also be applied for schemes with cross-fluxes, e.g. the J7 scheme presented by Arakawa and Lamb (1977), if the contributions of the cross-fluxes are considered accordingly.

4.2.4. 3D dissipation analysis

Both DVD analysis methods presented in Sections 4.2.3.1 and 4.2.3.2 can be applied to any transported quantity, including single velocity components. As recently demonstrated in 1D by Burchard (2012), the half DVD rate of velocity is the rate at which discrete specific kinetic energy is dissipated. On a 3D C-grid (Arakawa and Lamb, 1977) the specific kinetic energy within a FV-cell can be calculated in terms of the energies defined at the corresponding interfacial velocity points:

$$\left(\frac{1}{2}\mathbf{u}^2\right)_{i,j,k} = \frac{1}{V_{i,j,k}} \left\{ \begin{aligned} &\frac{1}{2} \left[V_{i-1/2,j,k} \left(\frac{1}{2}u_{i-1/2,j,k}^2 \right) + V_{i+1/2,j,k} \left(\frac{1}{2}u_{i+1/2,j,k}^2 \right) \right] \\ &+ \frac{1}{2} \left[V_{i,j-1/2,k} \left(\frac{1}{2}v_{i,j-1/2,k}^2 \right) + V_{i,j+1/2,k} \left(\frac{1}{2}v_{i,j+1/2,k}^2 \right) \right] \\ &+ \frac{1}{2} \left[V_{i,j,k-1/2} \left(\frac{1}{2}w_{i,j,k-1/2}^2 \right) + V_{i,j,k+1/2} \left(\frac{1}{2}w_{i,j,k+1/2}^2 \right) \right] \end{aligned} \right\}. \quad (4.20)$$

Therefore, the *discrete rate* at which specific kinetic is dissipated can be obtained from the individual DVD rates associated with the transport of the single velocity components u , v , w :

$$\left(\frac{1}{2}\chi_{i,j,k}(\mathbf{u})\right) = \frac{1}{V_{i,j,k}} \left\{ \begin{aligned} &\frac{1}{2} \left[V_{i-1/2,j,k} \left(\frac{1}{2}\chi_{i-1/2,j,k}(u) \right) + V_{i+1/2,j,k} \left(\frac{1}{2}\chi_{i+1/2,j,k}(u) \right) \right] \\ &+ \frac{1}{2} \left[V_{i,j-1/2,k} \left(\frac{1}{2}\chi_{i,j-1/2,k}(v) \right) + V_{i,j+1/2,k} \left(\frac{1}{2}\chi_{i,j+1/2,k}(v) \right) \right] \\ &+ \frac{1}{2} \left[V_{i,j,k-1/2} \left(\frac{1}{2}\chi_{i,j,k-1/2}(w) \right) + V_{i,j,k+1/2} \left(\frac{1}{2}\chi_{i,j,k+1/2}(w) \right) \right] \end{aligned} \right\}. \quad (4.21)$$

4.2.4.1. Dissipation due to a transversely isotropic stress tensor

In ocean models the turbulent stirring down to the viscous scales where molecular viscosity dissipates kinetic into internal energy according to the classical theory of cascading energy (Reynolds, 1895) cannot be resolved. Because at the smallest resolved scale molecular viscosity cannot yet act efficiently, the energy transfer to smaller scales is truncated. To avoid nonphysical energy accumulation, the

transfer of energy to the unresolved scales and its final dissipation are usually parameterised in terms of eddy-viscosity. Taking into account the spatial anisotropy between modelled horizontal and vertical scales, the turbulent forces in the momentum equations can be derived from a deviatoric stress tensor based on a transversely isotropic 4th-order eddy-viscosity tensor (Kamenkovich, 1967; Kirwan, 1969; Williams, 1972; Wajsowicz, 1993; Smith and McWilliams, 2003). As explained in Section 3.1, under the hydrostatic pressure assumption² the forces (F_x, F_y) in the balance of horizontal momentum are given in terms of a constant molecular as well as horizontal and vertical (kinematic) eddy-viscosities ν , $\nu^{\text{turb,h}}$ and $\nu^{\text{turb,v}}$, respectively,

$$F_\alpha = \frac{\partial}{\partial x_\beta} \left\{ \nu \frac{\partial u_\alpha}{\partial x_\beta} \right\} + \frac{\partial}{\partial x_\beta} \left\{ 2\nu^{\text{turb,h}} S_{\alpha\beta} \right\} + \frac{\partial}{\partial z} \left\{ \left(\nu + \nu^{\text{turb,v}} \right) \frac{\partial u_\alpha}{\partial z} \right\}, \quad (4.22)$$

with the horizontal deformation rate tensor

$$S_{\alpha\beta} = \frac{1}{2} \left(\frac{\partial u_\alpha}{\partial x_\beta} + \frac{\partial u_\beta}{\partial x_\alpha} \right). \quad (4.23)$$

Again, in (4.22) and in the following, summation is carried out over repeated indices with $\alpha, \beta \in \{x, y\}$ and $x_x = x$, $x_y = y$, $u_x = u$ and $u_y = v$. Similar to the diffusion terms in (4.1) and (4.2), with (4.22) the analytical and discrete rates at which specific kinetic energy is dissipated can be obtained from multiplication with $2u_\alpha$:

$$\begin{aligned} 2u_\alpha F_\alpha &= \frac{\partial}{\partial x_\beta} \left\{ 2u_\alpha \nu \frac{\partial u_\alpha}{\partial x_\beta} \right\} + \frac{\partial}{\partial x_\beta} \left\{ 2u_\alpha 2\nu^{\text{turb,h}} S_{\alpha\beta} \right\} + \frac{\partial}{\partial z} \left\{ 2u_\alpha \left(\nu + \nu^{\text{turb,v}} \right) \frac{\partial u_\alpha}{\partial z} \right\} \\ &\quad - 2 \left(\nu \left(\frac{\partial u_\alpha}{\partial x_\beta} \right)^2 + 2\nu^{\text{turb,h}} S_{\alpha\beta} \frac{\partial u_\alpha}{\partial x_\beta} + \left(\nu + \nu^{\text{turb,v}} \right) \left(\frac{\partial u_\alpha}{\partial z} \right)^2 \right) \end{aligned} \quad (4.24a)$$

$$\begin{aligned} &= \frac{\partial}{\partial x_\beta} \left\{ \left(\nu + \nu^{\text{turb,h}} \right) \frac{\partial (u_\alpha^2)}{\partial x_\beta} \right\} + \frac{\partial}{\partial x_\beta} \left\{ 2u_\alpha \nu^{\text{turb,h}} \frac{\partial u_\beta}{\partial x_\alpha} \right\} + \frac{\partial}{\partial z} \left\{ \left(\nu + \nu^{\text{turb,v}} \right) \frac{\partial (u_\alpha^2)}{\partial z} \right\} \\ &\quad - 2 \left(\nu \left(\frac{\partial u_\alpha}{\partial x_\beta} \right)^2 + 2\nu^{\text{turb,h}} S_{\alpha\beta} S_{\alpha\beta} + \left(\nu + \nu^{\text{turb,v}} \right) \left(\frac{\partial u_\alpha}{\partial z} \right)^2 \right). \end{aligned} \quad (4.24b)$$

²In this context the contribution of the vertical velocity w to the kinetic energy in (4.20) is neglected. Furthermore, $\chi_{i,j,k\pm 1/2}(w) = 0$ in (4.21), because no transport of w is carried out.

The nonconservative terms in (4.24a) and (4.24b) correspond with the analytical dissipation ϕ_{qh} derived in (A.11) and (A.20) and thus represent the *analytical rate* at which specific kinetic energy is dissipated:

$$\begin{aligned}
 \frac{1}{2}\chi^{\text{ana}}(\mathbf{u}) &= \nu \left(\frac{\partial u_\alpha}{\partial x_\beta} \right)^2 + 2\nu^{\text{turb,h}} S_{\alpha\beta} S_{\alpha\beta} + \left(\nu + \nu^{\text{turb,v}} \right) \left(\frac{\partial u_\alpha}{\partial z} \right)^2 \\
 &= \nu \left(\left(\frac{\partial u}{\partial x} \right)^2 + \left(\frac{\partial v}{\partial x} \right)^2 + \left(\frac{\partial u}{\partial y} \right)^2 + \left(\frac{\partial v}{\partial y} \right)^2 \right) \\
 &\quad + \nu^{\text{turb,h}} \left(2 \left(\frac{\partial u}{\partial x} \right)^2 + \left(\frac{\partial u}{\partial y} + \frac{\partial v}{\partial x} \right)^2 + 2 \left(\frac{\partial v}{\partial y} \right)^2 \right) \\
 &\quad + \left(\nu + \nu^{\text{turb,v}} \right) \left(\left(\frac{\partial u}{\partial z} \right)^2 + \left(\frac{\partial v}{\partial z} \right)^2 \right). \tag{4.25}
 \end{aligned}$$

For fixed α the discrete analogues to the conservative terms in (4.24a) and (4.24b) represent the contributions due to diffusion to the corresponding DVD rate $\chi_i(u_\alpha)$. However, the analysis method of Burchard and Rennau (2008) would be based on $\frac{\partial}{\partial x_\beta} \left\{ \nu^{\text{turb,h}} \frac{\partial}{\partial x_\alpha} (u_\beta^2) \right\}$ instead of $\frac{\partial}{\partial x_\beta} \left\{ 2u_\alpha \nu^{\text{turb,h}} \frac{\partial u_\beta}{\partial x_\alpha} \right\}$ as derived in (4.24b). In contrast, following the outline in Section 4.2.2.2, within the alternative analysis method the diffusive fluxes of second moments are calculated as

$$J_{i,j,k}^{\text{diff}}(u^2) = 2 \frac{1}{2} \left(u_{i-1/2,j,k} + u_{i+1/2,j,k} \right) J_{i,j,k}^{\text{diff}}(u), \tag{4.26a}$$

$$J_{i+1/2,j+1/2,k}^{\text{diff}}(u^2) = 2 \frac{1}{2} \left(u_{i+1/2,j,k} + u_{i+1/2,j+1,k} \right) J_{i+1/2,j+1/2,k}^{\text{diff}}(u), \tag{4.26b}$$

$$J_{i+1/2,j,k+1/2}^{\text{diff}}(u^2) = 2 \frac{1}{2} \left(u_{i+1/2,j,k} + u_{i+1/2,j,k+1} \right) J_{i+1/2,j,k+1/2}^{\text{diff}}(u), \tag{4.26c}$$

$$J_{i+1/2,j+1/2,k}^{\text{diff}}(v^2) = 2 \frac{1}{2} \left(v_{i,j+1/2,k} + v_{i+1,j+1/2,k} \right) J_{i+1/2,j+1/2,k}^{\text{diff}}(v), \tag{4.26d}$$

$$J_{i,j,k}^{\text{diff}}(v^2) = 2 \frac{1}{2} \left(v_{i,j-1/2,k} + v_{i,j+1/2,k} \right) J_{i,j,k}^{\text{diff}}(v), \tag{4.26e}$$

$$J_{i,j+1/2,k+1/2}^{\text{diff}}(v^2) = 2 \frac{1}{2} \left(v_{i,j+1/2,k} + v_{i,j+1/2,k+1} \right) J_{i,j+1/2,k+1/2}^{\text{diff}}(v). \tag{4.26f}$$

With (4.26a)–(4.26f) explicitly defined in terms of the diffusive fluxes in the momentum equations,

$$J_{i,j,k}^{\text{diff}}(u) = -A_{i,j,k}^x \frac{\nu + 2\nu_{i,j,k}^{\text{turb,h}}}{\Delta x_{i,j,k}} [u_{i^*,j,k}]_{i^*=i-1/2}^{i^*=i+1/2}, \quad (4.27a)$$

$$J_{i+1/2,j+1/2,k}^{\text{diff}}(u) = -A_{i+1/2,j+1/2,k}^y \left(\frac{\nu + \nu_{i+1/2,j+1/2,k}^{\text{turb,h}}}{\Delta y_{i+1/2,j+1/2,k}} [u_{i+1/2,j^*,k}]_{j^*=j}^{j^*=j+1} + \frac{\nu_{i+1/2,j+1/2,k}^{\text{turb,h}}}{\Delta x_{i+1/2,j+1/2,k}} [v_{i^*,j+1/2,k}]_{i^*=i}^{i^*=i+1} \right), \quad (4.27b)$$

$$J_{i+1/2,j,k+1/2}^{\text{diff}}(u) = -A_{i+1/2,j,k+1/2}^z \frac{\nu + \nu_{i+1/2,j,k+1/2}^{\text{turb,v}}}{\Delta z_{i+1/2,j,k+1/2}} [u_{i+1/2,j,k^*}]_{k^*=k}^{k^*=k+1}, \quad (4.27c)$$

$$J_{i+1/2,j+1/2,k}^{\text{diff}}(v) = -A_{i+1/2,j+1/2,k}^x \left(\frac{\nu_{i+1/2,j+1/2,k}^{\text{turb,h}}}{\Delta y_{i+1/2,j+1/2,k}} [u_{i+1/2,j^*,k}]_{j^*=j}^{j^*=j+1} + \frac{\nu + \nu_{i+1/2,j+1/2,k}^{\text{turb,h}}}{\Delta x_{i+1/2,j+1/2,k}} [v_{i^*,j+1/2,k}]_{i^*=i}^{i^*=i+1} \right), \quad (4.27d)$$

$$J_{i,j,k}^{\text{diff}}(v) = -A_{i,j,k}^y \frac{\nu + 2\nu_{i,j,k}^{\text{turb,h}}}{\Delta y_{i,j,k}} [v_{i,j^*,k}]_{j^*=j-1/2}^{j^*=j+1/2}, \quad (4.27e)$$

$$J_{i,j+1/2,k+1/2}^{\text{diff}}(v) = -A_{i,j+1/2,k+1/2}^z \frac{\nu + \nu_{i,j+1/2,k+1/2}^{\text{turb,v}}}{\Delta z_{i,j+1/2,k+1/2}} [v_{i,j+1/2,k^*}]_{k^*=k}^{k^*=k+1}, \quad (4.27f)$$

all conservative terms in (4.24a) and (4.24b) are captured correctly.

4.3. Applications

In this Section the mixing and dissipation analyses presented and developed in the preceding Section are applied to three different test cases. In an idealised 1D test case the DVD caused by popular TVD-schemes is diagnosed. Additional 3D simulations were carried out with the General Estuarine Transport Model (GETM, described in Chapter 3). In a benchmark test case without any physical diffusivities, the combined effects of spurious dissipation and mixing are investigated. Finally, results comparing the physically and numerically induced mixing and dissipation for a realistic Western Baltic Sea model are presented. For the applications in the present Chapter the traditional hydrostatic pressure assumption is valid.

4.3.1. Analysis of 1D TVD-schemes

From (4.5) the discrete 1D advection equation can be obtained as

$$\frac{V_i^{(n+1)} \varphi_i^{(n+1)} - V_i^{(n)} \varphi_i^{(n)}}{\Delta t} + [A_{i'} u_{i'} \tilde{\varphi}_{i'}]_{i'=i-1/2}^{i'=i+1/2} = 0. \quad (4.28)$$

A variety of explicit upstream-biased advection schemes can be formulated based on

$$u_{i'} \tilde{\varphi}_{i'} = u_{i'}^+ \left(\varphi_{i'-1/2}^{(n)} + \psi_{i'}^+ \tilde{\varphi}_{i'}^+ \right) + u_{i'}^- \left(\varphi_{i'+1/2}^{(n)} + \psi_{i'}^- \tilde{\varphi}_{i'}^- \right), \quad (4.29)$$

with

$$u_{i'}^+ = \max \{0, u_{i'}\}, \quad (4.30a)$$

$$u_{i'}^- = \min \{u_{i'}, 0\}. \quad (4.30b)$$

In (4.29) the diffusive FOU flux is combined with an antidiffusive Lax-Wendroff correction with

$$\tilde{\varphi}_{i'}^\pm = \frac{1}{2} (1 - \text{CFL}_{i'} (\pm u_{i'}^\pm)) \left(\varphi_{i' \pm 1/2}^{(n)} - \varphi_{i' \mp 1/2}^{(n)} \right), \quad (4.31)$$

defined in terms of the Courant number

$$\text{CFL}_{i'}(u) = \frac{u \Delta t}{\Delta x_{i'}}. \quad (4.32)$$

The contribution of the Lax-Wendroff correction is limited by the nonnegative limiter $\psi_{i'}^\pm$.

The TVD-schemes analysed in the present study are recovered for (see e.g. Pietrzak (1998)):

$$\psi_{i'}^{\text{FOU},\pm} = 0, \quad (4.33a)$$

$$\psi_{i'}^{\text{minmod},\pm} = \max(0, \min(r_{i'}^{\pm}, 1)), \quad (4.33b)$$

$$\psi_{i'}^{\text{Superbee},\pm} = \max(0, \min(2r_{i'}^{\pm}, 1), \min(r_{i'}^{\pm}, 2)), \quad (4.33c)$$

$$\psi_{i'}^{\text{P2-PDM},\pm} = \max\left(0, \min\left(\frac{2r_{i'}^{\pm}}{\text{CFL}_{i'}(\pm u_{i'}^{\pm})}, \psi_{i'}^{\text{P2},\pm}, \frac{2}{1 - \text{CFL}_{i'}(\pm u_{i'}^{\pm})}\right)\right), \quad (4.33d)$$

with

$$r_{i'}^{\pm} = \frac{(\varphi_{i' \mp 1/2}^{(n)} - \varphi_{i' \mp 3/2}^{(n)})}{(\varphi_{i' \pm 1/2}^{(n)} - \varphi_{i' \mp 1/2}^{(n)})}, \quad (4.34)$$

and

$$\psi_{i'}^{\text{P2},\pm} = 1 - \frac{1}{3} (1 + \text{CFL}_{i'}(\pm u_{i'}^{\pm})) (1 - r_{i'}^{\pm}). \quad (4.35)$$

To compare the performance of these schemes, the dimensionless advection of a box and a Gaussian profile by a uniform velocity of $u = 1$ through a periodic domain of length $L = 100$ is simulated. Figure 4.1a shows the profiles obtained after 200 time steps for a spatio-temporal resolution of $\Delta x = 1$ and $\Delta t = 0.5$. As expected, the explicit FOU scheme smoothed gradients rather fast and thus did not preserve the shape of the initial profiles. In contrast, the higher-order TVD-schemes show a better convergence towards the analytical profiles.

Based on (4.11), (4.14) and (4.15) the associated DVD rates were calculated according to:

$$\chi_i^{\text{BR08},(n+1)}(\varphi) = -\frac{1}{\Delta t V_i^{(n+1)}} \left(V_i^{(n+1)} (\varphi_i^{(n+1)})^2 - V_i^{(n)} (\varphi_i^{(n)})^2 + \Delta t [A_{i'} u_{i'} (\widetilde{\varphi^2})_{i'}]_{i'=i-1/2}^{i'=i+1/2} \right), \quad (4.36a)$$

$$\chi_i^{\text{K13},(n+1)}(\varphi) = -\frac{1}{\Delta t V_i^{(n+1)}} \left(V_i^{(n+1)} (\varphi_i^{(n+1)})^2 - V_i^{(n)} (\varphi_i^{(n)})^2 + \Delta t [A_{i'} u_{i'} (\widetilde{\varphi}_{i'})^2]_{i'=i-1/2}^{i'=i+1/2} \right). \quad (4.36b)$$

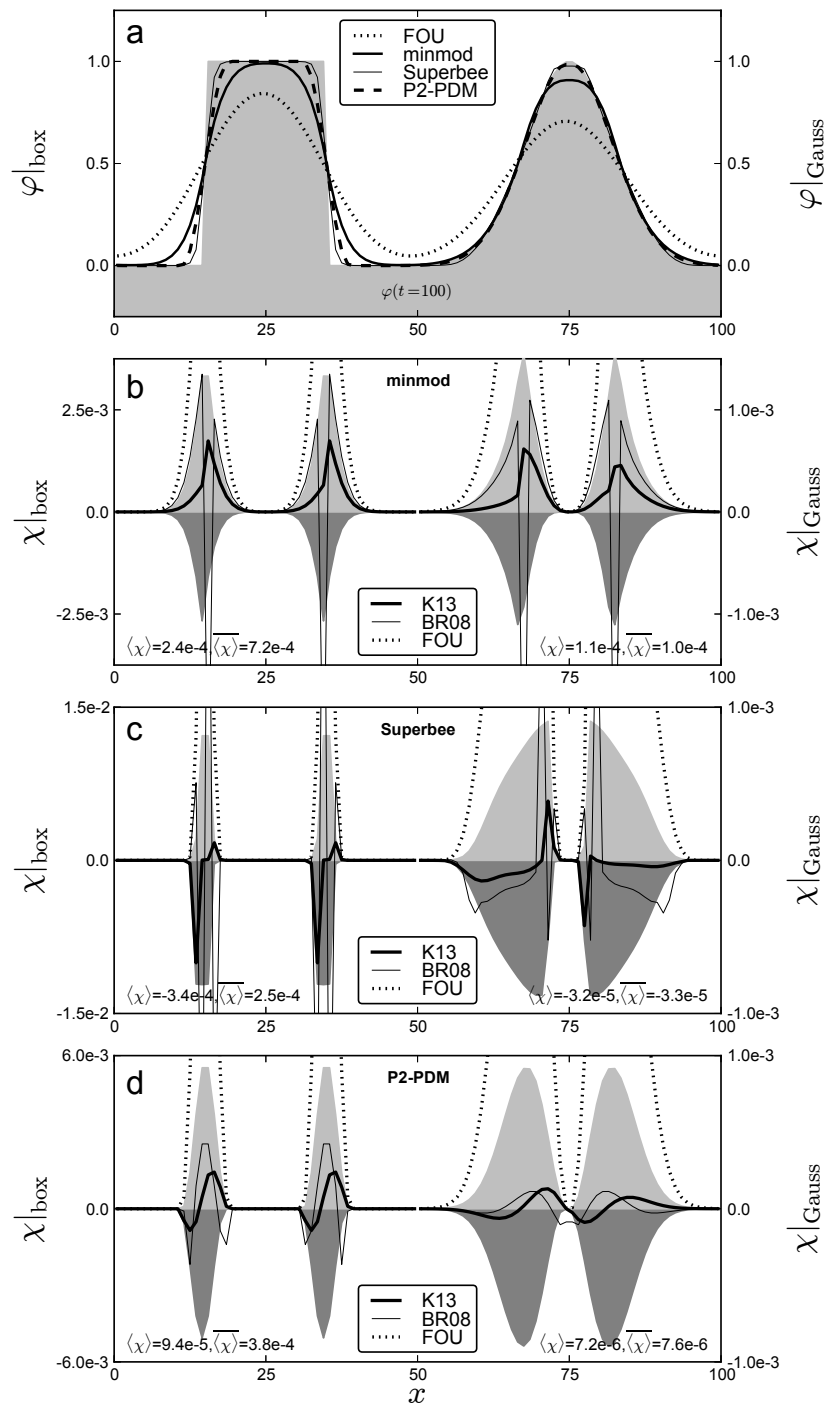


Figure 4.1.: Analysis of 1D TVD-schemes: Numerical solutions obtained from different TVD-schemes in comparison to the analytical solution (light grey shape, a) and with diagnosed DVD rates (b-d). In b-d the contributions to χ_i^{K13} due to variance growth during decomposition $-\frac{1}{\Delta t} (\Delta \sigma^2)_i^{d,(n)}$ and decay during recombination $-\frac{1}{\Delta t} (\Delta \sigma^2)_i^{r,(n+1)}$ are shown by dark and light grey shapes, respectively. The dotted lines in b-d depict the analytically calculated DVD rate of the explicit FOU scheme for the actual profile. The measures $\langle \chi \rangle$ and $\overline{\langle \chi \rangle}$ quantify the average and mean average DVD rates.

		box profile			Gaussian profile			
		Δt	0.3125	0.5000	0.6250	0.3125	0.5000	0.6250
		Δx	$\langle \chi \rangle$			$\langle \chi \rangle$		
FOU	0.625		1.3e-3	8.0e-4	—	5.4e-4	2.6e-4	—
	1.000		1.8e-3	1.6e-3	1.4e-3	8.7e-4	7.3e-4	6.1e-4
	1.250		2.0e-3	1.8e-3	1.7e-3	1.0e-3	9.1e-4	8.3e-4
minmod	0.625		5.3e-4	3.9e-4	—	3.6e-5	1.3e-5	—
	1.000		8.1e-4	7.2e-4	6.5e-4	1.4e-4	1.0e-4	7.5e-5
	1.250		9.6e-4	8.9e-4	8.3e-4	2.6e-4	1.9e-4	1.6e-4
Superbee	0.625		1.6e-4	1.5e-4	—	-1.6e-5	-8.1e-6	—
	1.000		2.5e-4	2.5e-4	2.5e-4	-4.4e-5	-3.3e-5	-2.5e-5
	1.250		3.1e-4	3.1e-4	3.1e-4	-6.6e-5	-5.6e-5	-4.8e-5
P2-PDM	0.625		2.7e-4	2.1e-4	—	1.8e-6	7.0e-7	—
	1.000		4.1e-4	3.8e-4	3.6e-4	1.0e-5	7.6e-6	5.6e-6
	1.250		5.0e-4	4.7e-4	4.5e-4	2.1e-5	1.8e-5	1.5e-5

Table 4.1.: Analysis of 1D TVD-schemes: Diagnosed mean average DVD rates $\langle \chi \rangle$. Experiments with $CFL = 0.5$ are denoted by bold entries. Missing entries represent a vanishing DVD rate, originating from $CFL = 1$.

Only for the explicit FOU scheme $(\widetilde{\varphi^2})_{i'} \equiv (\widetilde{\varphi}_{i'})^2$ holds and (4.36a) and (4.36b) coincide. For the other schemes χ_i^{BR08} and χ_i^{K13} strongly differ (Figure 4.1b–d). A quantitative comparison of the DVD rates and the average DVD rates $\langle \chi \rangle = (L/2)^{-1} \int_{(L/2)} \chi dx$ between the schemes is not meaningful, because the DVD rates are not associated with the advection of the identical profile of φ anymore. For this reason, the DVD rates for the explicit FOU scheme drawn in Figure 4.1b–d were calculated by means of (B.15) for the corresponding actual profile. In contrast, the mean average DVD rate $\langle \chi \rangle = \frac{1}{T} \int_T \langle \chi \rangle dt$ provides a meaningful measure for direct intercomparison. In this context, it should be noted that the integration domain $(L/2)$ was not fixed, but represents the domain moved with the box or Gaussian profile. For the higher-order TVD-schemes the contribution of the antidiffusive fluxes significantly decreased $\langle \chi \rangle$. The Superbee scheme (Figure 4.1c) showed the smallest $\langle \chi \rangle$, even a negative value for the Gaussian profile. Negative DVD rates indicate artificial steepening of gradients due to dominating antidiffusive fluxes. Among the investigated schemes in this study, the Superbee scheme was the only scheme showing negative $\langle \chi \rangle$. However, as obvious for the box profile, a negative $\langle \chi \rangle$ at a particular instant of time did not imply a negative $\langle \chi \rangle$. Among the investigated schemes the P2-PDM schemes showed optimal performance for both the box and the Gaussian profile. For the box profile the $\langle \chi \rangle$ caused by the P2-PDM scheme was only marginally larger than the minimum value caused by the Superbee scheme. The minimum shape deformation of the Gaussian profile by the P2-PDM scheme is mirrored in a $\langle \chi \rangle$ of minimum order of magnitude.

Based on the alternative derivation of (4.36b), outlined in B.4, the decreased DVD rates for the higher-order TVD-schemes can also be explained by variance growth during the decomposition, additionally compensating to a large extent the already decreased variance decay during the recombination (grey shapes in Figure 4.1b–d). The resulting χ_i^{K13} smoothly connects these regions. In contrast, χ_i^{BR08} shows disproportional over- and undershoots. Their symmetry for $CFL = 0.5$ also indicates a missing dependence on the direction of the frontal propagation.

Additional experiments were carried out to investigate the dependence of $\langle \chi \rangle$ on the spatio-temporal resolution (Table 4.1). For all experiments the magnitude of $\langle \chi \rangle$ decreased with an improved spatial resolution, but increased with an improved temporal resolution. The former tendency also dominated if the Courant number was kept constant. For the explicit FOU scheme further experiments with only

one profile showed that the impact of the marginal interaction between the box and Gaussian profiles on the quantified $\overline{\langle \chi \rangle}$ was negligible.

Improvement of GETM's 2D-mode The investigated superiority of higher-order advection schemes motivated their application also for the depth-averaged velocities in (3.13b) and (3.13c) in the 2D-mode of GETM. This missing feature was implemented by the author and is part of the official GETM code since release v2.2 from April 2012. Due to the shift of 3D velocity profiles, see (3.19a) and (3.19b), the improved treatment of the depth-averaged velocities directly implies a more accurate transport of quantities within the 3D-mode.

4.3.2. Analysis of an idealised mesoscale eddy

In a comprehensive series of laboratory experiments Griffiths and Linden (1981) studied mixed baroclinic/barotropic instabilities during the geostrophic adjustment of a cylindrical patch of less dense fluid. James (1996) adopted the experimental setup and designed a test case on estuarine scales to assess advection schemes of ocean models. For this test case Tartinville et al. (1998) demonstrated the sensitivity of the number of growing vortices to the scheme for lateral advection of momentum. A derived relation between the order of the dominating baroclinic instability and the ratio of kinetic to available potential energy also indicated why dissipative schemes caused a mode 4 instability instead of the expected mode 2 instability.

The setup investigated here was identical to the one of Tartinville et al. (1998), including the 4 km wide sponge layer framing the 30 km \times 30 km \times 20 m quadrangular basin. The horizontal resolution was 1 km and in the vertical 20 equidistant σ -layers were used. In contrast to Tartinville et al. (1998), the cylindrical patch of less salty fluid was located directly in the centre of the basin to avoid any axis-asymmetric forcing due to the boundaries. A reference simulation was performed with all lateral and vertical advection carried out with the Superbee scheme (case TVD-TVD). This combination was also successfully investigated by James (1996). Subsequent simulations were performed with either the lateral advection of momentum carried out with the explicit FOU scheme (case FOU-TVD), or the lateral advection of salinity carried out with the explicit FOU scheme (case TVD-FOU), or both carried out with the explicit FOU scheme (case FOU-FOU). Since all simulations were performed without explicit physical diffusion of momentum and salt, the diagnosed DVD is purely of numerical origin and can be utilised to elucidate the influence of the different advection schemes.

The interplay of both numerical dissipation and mixing, the latter increasing the background potential energy (Fringer et al., 2005), provokes an analysis of the energy composition which was only incompletely presented by Tartinville et al. (1998). In this context the 3D dissipation analysis developed in Section 4.2.4 provides a missing piece of information to assess the energy conservation of an ocean model.

For all simulations Figure 4.2 shows the evolution of the global energy composition. At the beginning of the simulations there is only Available Potential Energy (APE). The near-inertial pulsation of the freshwater patch during the geostrophic adjustment and the associated energy transfer between available potential energy and Kinetic Energy (KE) is obvious. It is the induced high velocity (gradients) during this adjustment period that triggered the increase of numerically dissipated energy (ND). Caused by the momentum advection with FOU this numerical dissipation is enhanced for case FOU-TVD (also compare Figures 4.3b,c). Although momentum advection was performed with FOU as well, for case FOU-FOU less kinetic energy than for case FOU-TVD was dissipated because the salinity advection with FOU smoothed the baroclinic pressure gradients and thus decreased the resulting

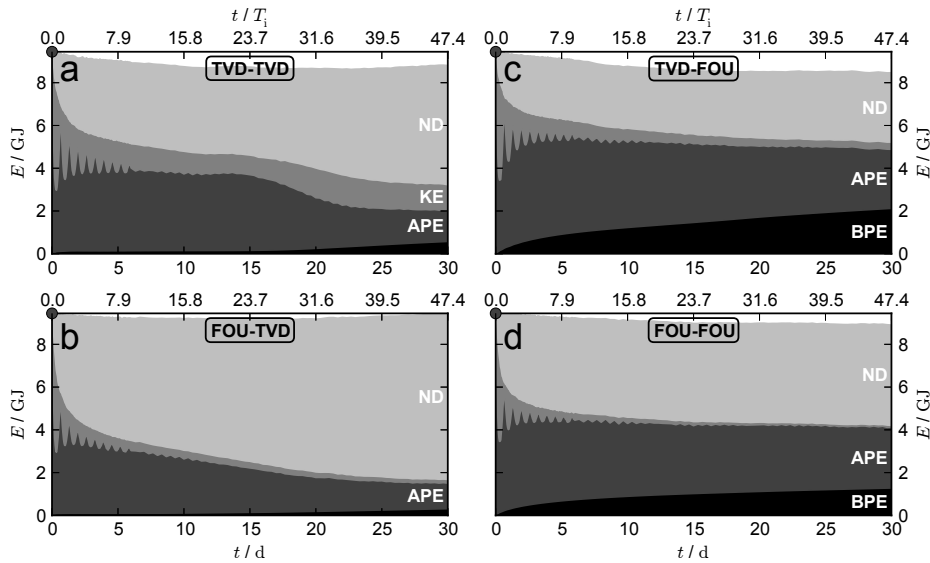


Figure 4.2.: Analysis of an idealised mesoscale eddy: Evolution of global energy composition. Stacked plots with contour shapes showing Background Potential Energy (BPE, black), Available Potential Energy (APE, dark grey), Kinetic Energy (KE, grey) and numerically dissipated energy (ND, light grey). Time is given in days and inertial periods. The initial APE is indicated by the dark grey circle.

shear of the flow field. Salinity advection with FOU also enhanced numerical mixing (compare Figures 4.3e,f), increasing the background potential energy (BPE). However, the reduced stirring due to the momentum advection with FOU for case FOU-FOU provided a smaller surface for the mixing of salinity gradients than for case TVD-FOU. The decreased growth of background potential energy due to increased numerical dissipation coincides with similar findings of Ilicak et al. (2012). Slight deviations from the constancy of the sum of potential, kinetic and numerically dissipated energy are assumed to be mainly caused by the additional sponge layer. Furthermore, they might also indicate an inconsistent model discretisation, those identification would be beyond the scope of the present study.

Since FOU was used only for the lateral advection of salinity for cases TVD-FOU and FOU-FOU, the associated numerical mixing only marginally changed the total potential energy and the increase of the background potential energy was balanced by a decrease of available potential energy. However, a more important sink for available potential energy was the transformation into kinetic energy. This transformation was enhanced by strong baroclinic pressure gradients preserved by salinity advection with Superbee. Therefore and because of weak dissipation due to momentum advection with Superbee, only the reference simulation (case TVD-TVD) provided a ratio of kinetic to available potential energy large enough to promote the formation of a mode-2 instability (compare Figures 4.4b,c,f). The growth of unstable vortices was associated with the further enhanced transformation of available potential energy into kinetic energy and its subsequent dissipation between days 15 and 23 (Figure 4.2a).

These results are consistent with the findings of James (1996) and Tartinville et al. (1998). For case TVD-TVD James (1996) also reported the formation of a mode-2 instability. Except for the scheme of vertical momentum advection, case FOU-TVD coincides with an experiment in Tartinville et al. (1998) also showing a mode-4 instability. This demonstrates again the strong sensitivity to the scheme for lateral advection of momentum identified by Tartinville et al. (1998).

Figures 4.3 and 4.4 show snapshots of both the numerical dissipation and mixing diagnosed in the

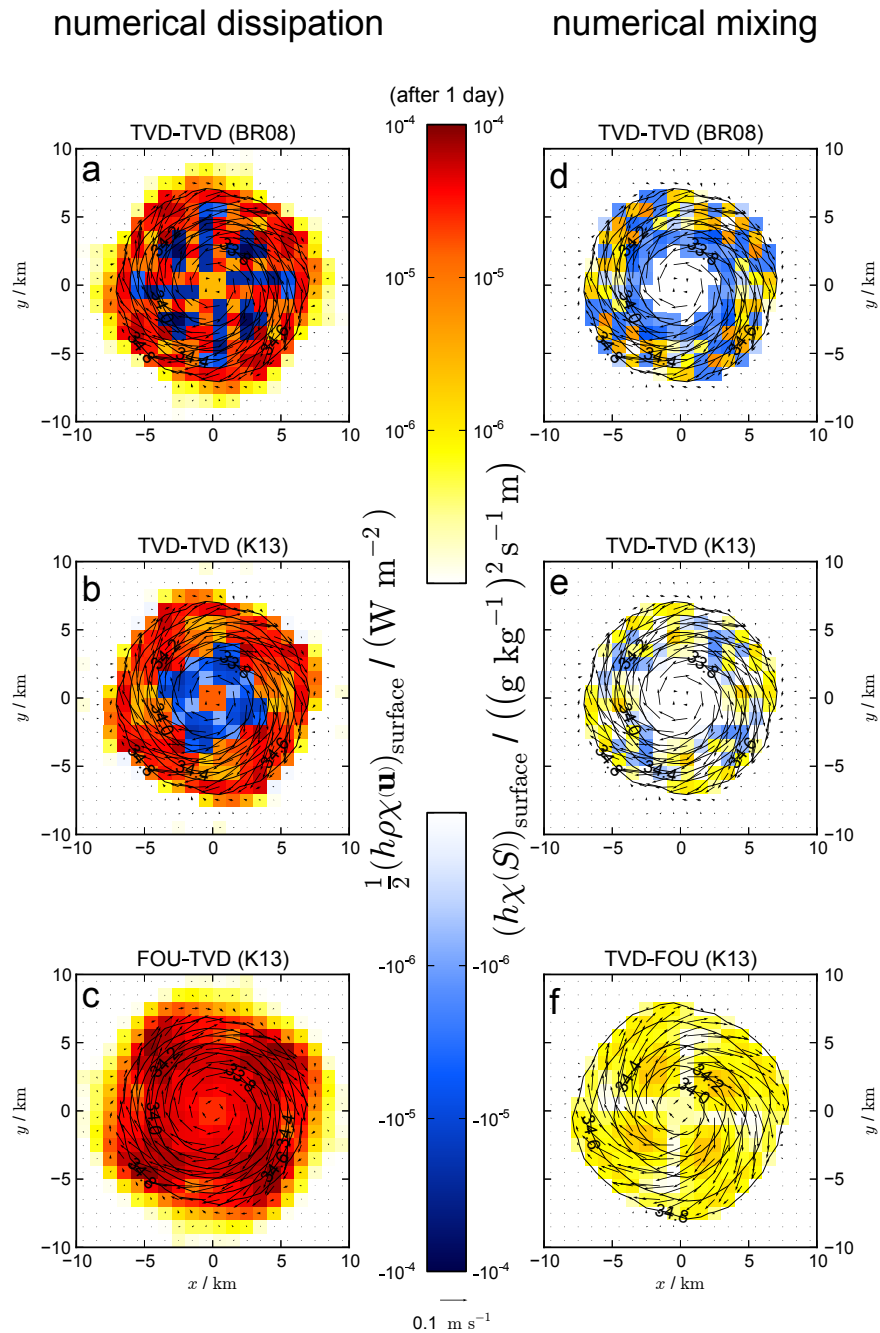


Figure 4.3.: Analysis of an idealised mesoscale eddy: Dissipation and mixing analysis (after 1 day). Snapshots of the flow field (arrows) with isohalines (contour lines) and diagnosed numerical dissipation and mixing (coloured, a–c and d–f, respectively) integrated over the surface layer obtained by different simulations. For the reference simulation the quantities diagnosed according to Burchard and Rennau (2008, BR08) are shown in a and d. The ticks on the left side of the colorbars refers to a–c, the ticks on the right to d–f.

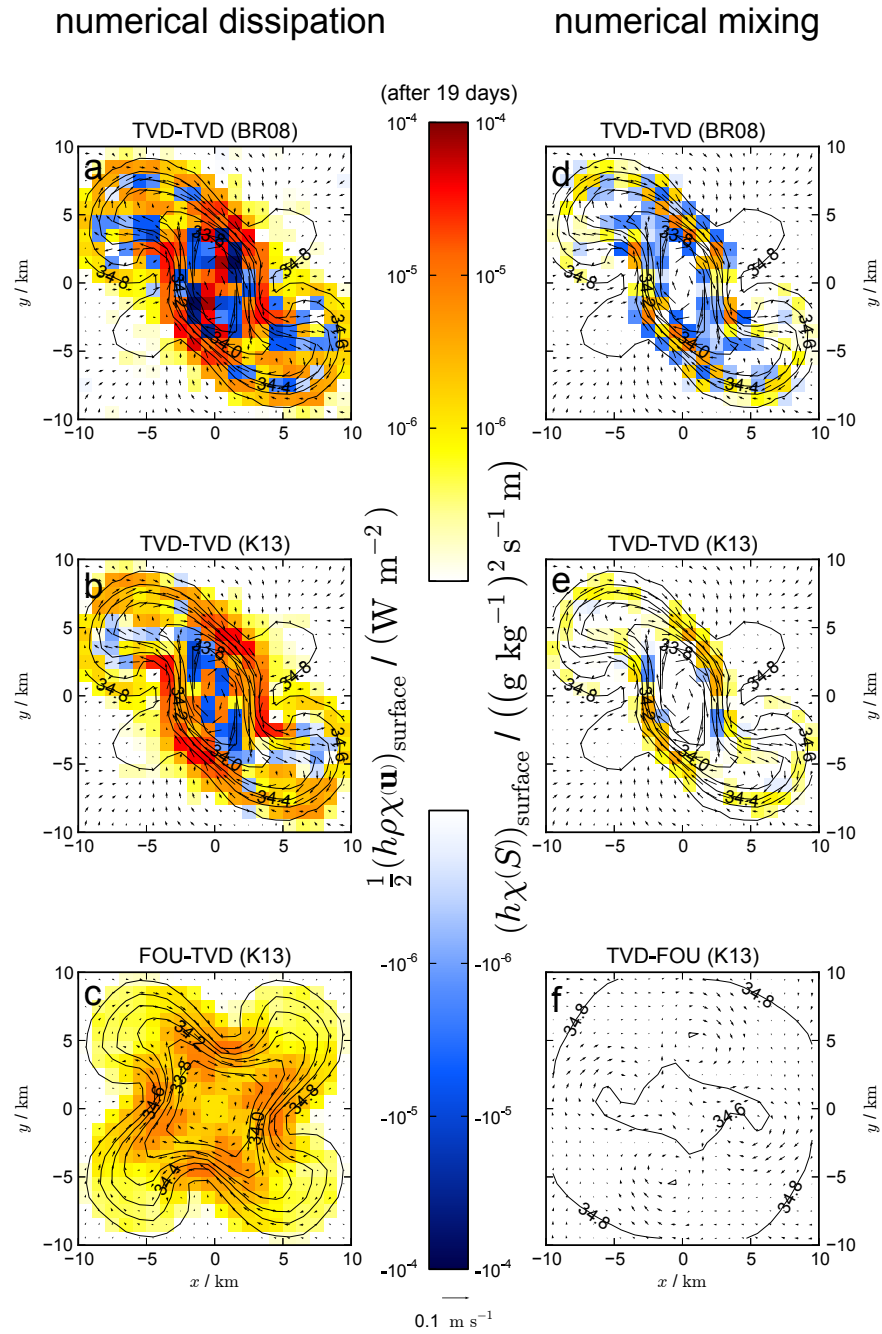


Figure 4.4.: Analysis of an idealised mesoscale eddy: Dissipation and mixing analysis (after 19 days). See caption of Figure 4.3.

surface layer after 1 and 19 days, respectively. For the reference simulation (case TVD-TVD) the comparison of the alternative analysis method (see Figures 4.3b,e and 4.4b,e) with the analysis method of Burchard and Rennau (2008, BR08) (see Figures 4.3a,d and 4.4a,d) highlights a rather noisy pattern for the latter. Figures 4.3,4.4b indicates strong negative numerical dissipation rates in the core of the eddy, enhancing the kinetic energy and thus promoting the baroclinic mode-2 instability.

4.3.3. Analysis of a realistic Western Baltic Sea model

The Baltic Sea is a large semi-enclosed marginal sea on the North-European shelf with the narrow and shallow Danish Straits being its only connection to the North Sea and the Atlantic Ocean. The transport of dense and oxygenated water from the Kattegat, located between the Danish Straits and the North Sea, through this bottleneck into and further across shallow sills within the Western Baltic Sea (see Figure 4.5) is of crucial importance for the ecological state of the deep basins in the Baltic Proper. River runoff and net precipitation into the Baltic Sea establish a surface outflow of brackish water through and a permanent lateral salinity gradient towards and across the Danish Straits. The latter drives an estuarine circulation with near-bottom inflow of saline water from and enhanced surface outflow into the Kattegat. However, the drainage of the inflowing dense bottom water into the chain of Baltic basins is hampered by shallow sills. Significant overflows of dense water are irregularly triggered by two opposite meteorological conditions. During persistent periods of calm conditions the saline bottom water entering through the Great Belt and passing the Fehmarn Belt is not diluted due to wind mixing and can spill over the 18 m deep Darss Sill. These *baroclinic inflows* cannot occur across the only 7 m deep Drogden Sill south of the Øresund. In contrast, *barotropic inflows* are driven by sealevel differences across the Danish Straits, set up by a specific sequence of wind regimes. Depending on the strength and duration of the sealevel differences, barotropic inflows occur only across Drogden Sill or across both Drogden and Darss Sill. Contrary to baroclinic inflows, they cause a net inflow of water volume. After passing the sills, inflowing dense water forms a bottom gravity current with the potential of subsequently replacing old water masses in the adjacent downstream basins. This potential is determined by its density and volume. Reissmann et al. (2009) reviewed different mixing mechanisms affecting these properties during the penetration of the bottom gravity current.

Started with an idealised GETM setup of Burchard et al. (2005), in the recent years a validated high resolution setup of the Western Baltic Sea had been established to study the dynamics in the transition area between the Kattegat and the deep basins of the Baltic Proper (Burchard et al., 2009; Rennau and Burchard, 2009; Rennau et al., 2012; Gräwe and Burchard, 2012; Gräwe et al., 2013; Burchard and Gräwe, 2013). Based on two different measures for vertical mixing, one of them being the discrete AVD rate (B.12), Burchard et al. (2009) identified regions of enhanced physical mixing. Yet, Rennau and Burchard (2009) diagnosed spurious (*numerical*) mixing of the same order. After switching to adaptive vertical meshes (Hofmeister et al., 2010) and with an improved lateral resolution Burchard and Gräwe (2013) reported a slight dominance of physical mixing.

For the present study the setup of Burchard and Gräwe (2013) was used with a slightly extended model domain, covering a larger part of the Kattegat and a larger part east of the Bornholm Basin (Figure 4.5). In a future project this setup and high-resolution nestings therein should be utilised to investigate near-inertial waves in the Bornholm Basin. The model-based quantification of enhanced dissipation and mixing rates associated with localised shear bands observed by field campaigns (van der Lee and Umlauf, 2011) should lead to a better bulk parameterisation for coarser models. For this purpose a reliable diagnostic tool for the local quantification of physically and numerically induced dissipation and mixing is essential. Here the alternative DVD analysis method outlined in Sections 4.2.2.2 and 4.2.3.2 in conjunction with the 3D dissipation analysis developed in Section 4.2.4 is

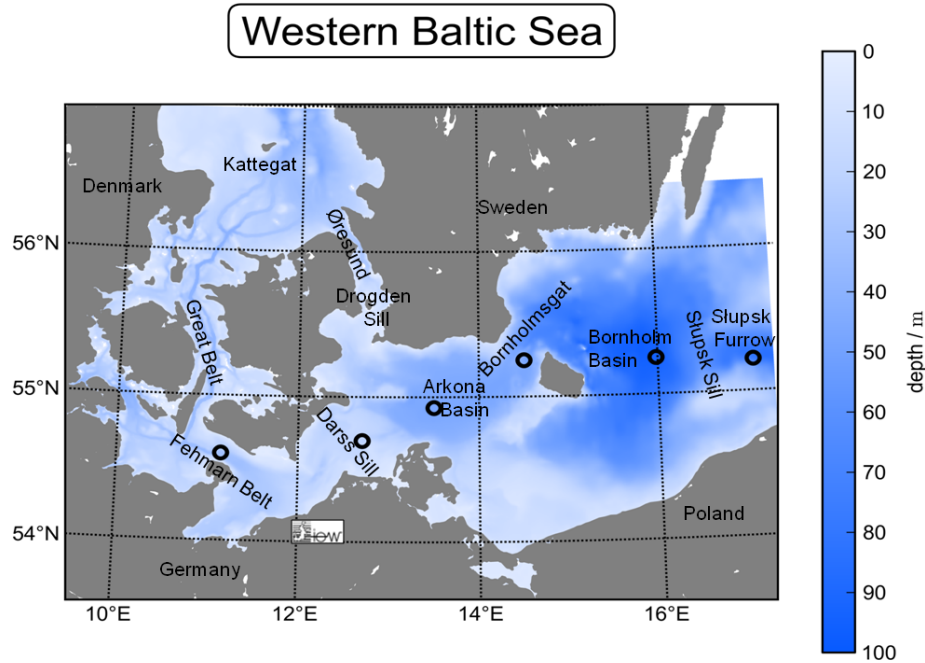


Figure 4.5.: Analysis of a realistic Western Baltic Sea model: Map of model domain

demonstrated to be such a tool. Results are presented for the period 19-28 September 2008, covering a field campaign in the Bornholm Basin.

Because the analysis method of Burchard and Rennau (2008) fails for the transversely isotropic stress tensor (see Section 4.2.4.1), the DVD due to diffusion was not quantified as outlined in Section 4.2.4.1 and B.2. To compare all DVD analyses in a consistent way, the physical dissipation was calculated by means of a discrete analogue to the analytical dissipation rate (4.25), the physical mixing in terms of the discrete AVD rate (B.12) and the numerical contributions to the DVD due to diffusion, e.g. (B.13), were neglected. The numerical dissipation and mixing due to advection were quantified as described in (4.21) and Section 4.2.3. Lateral diffusivities are parameterised according to Smagorinsky (1963, 1993) based on a discrete analogue to (4.25), a feature recently implemented by the author for the future higher-resolution nestings³. Vertical turbulence was parameterised by a dynamic $k - \varepsilon$ -model coupled to the algebraic second-order closure of Canuto et al. (2001, "Model A"). In a reference simulation lateral advection was carried out with the P2-PDM scheme, whereas in the vertical the Superbee scheme was applied due to stability problems with P2-PDM (for a possible explanation see Appendix B.1). The horizontal resolution was approximately 600 m and in the vertical 40 adaptive layers (Hofmeister et al., 2010) were used. The model sufficiently reproduced the dynamics in the Western Baltic Sea, exemplary shown for the inflows into the Arkona Basin in Figure 4.6.

The impact of the Superbee scheme, used for the vertical advection, manifested in large areas of negative mean depth-integrated numerical mixing rates (Figures 4.7, 4.8b), not present in the simulation of Rennau and Burchard (2009) performed with the P2-PDM scheme in the vertical. In agreement with the results of the idealised test case in Section 4.3.1, the origin of these negative mixing rates were pronounced vertical gradients (Figures 4.7, 4.8d). In particular in the interior of the Bornholm Basin, their locations were determined by the permanent halocline around 60 m depth, the seasonal

³The decrease of numerical variance decay for improved resolutions and higher-order schemes was demonstrated in Table 4.1. This decrease offers and also requires the implementation of physically induced variance decay, hitherto neglected because of the high numerical variance decay. In contrast to constant diffusivities, Smagorinsky-diffusivities scale with the resolution and the resolved dissipation and converge to zero for very high resolution.

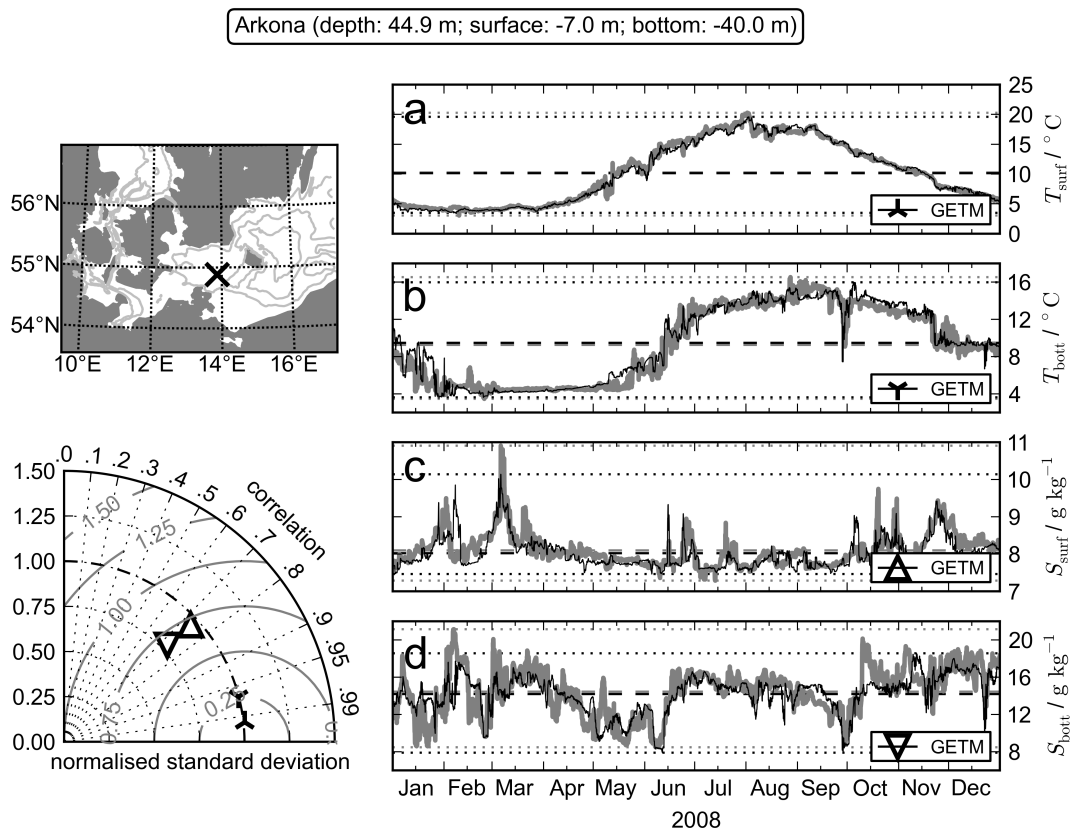


Figure 4.6.: Analysis of a realistic Western Baltic Sea model: Longterm validation against mooring data from the Arkona Basin. The position of the station is marked in the map. Time series of hourly data from the mooring (solid grey lines) and GETM (solid black lines) for surface temperature (a), bottom temperature (b), surface salinity (c) and bottom salinity (d) are shown. Correspondingly coloured dotted and dashed lines depict extreme and mean values, respectively. The Taylor diagram (Taylor, 2001) is based on all data from 2008.

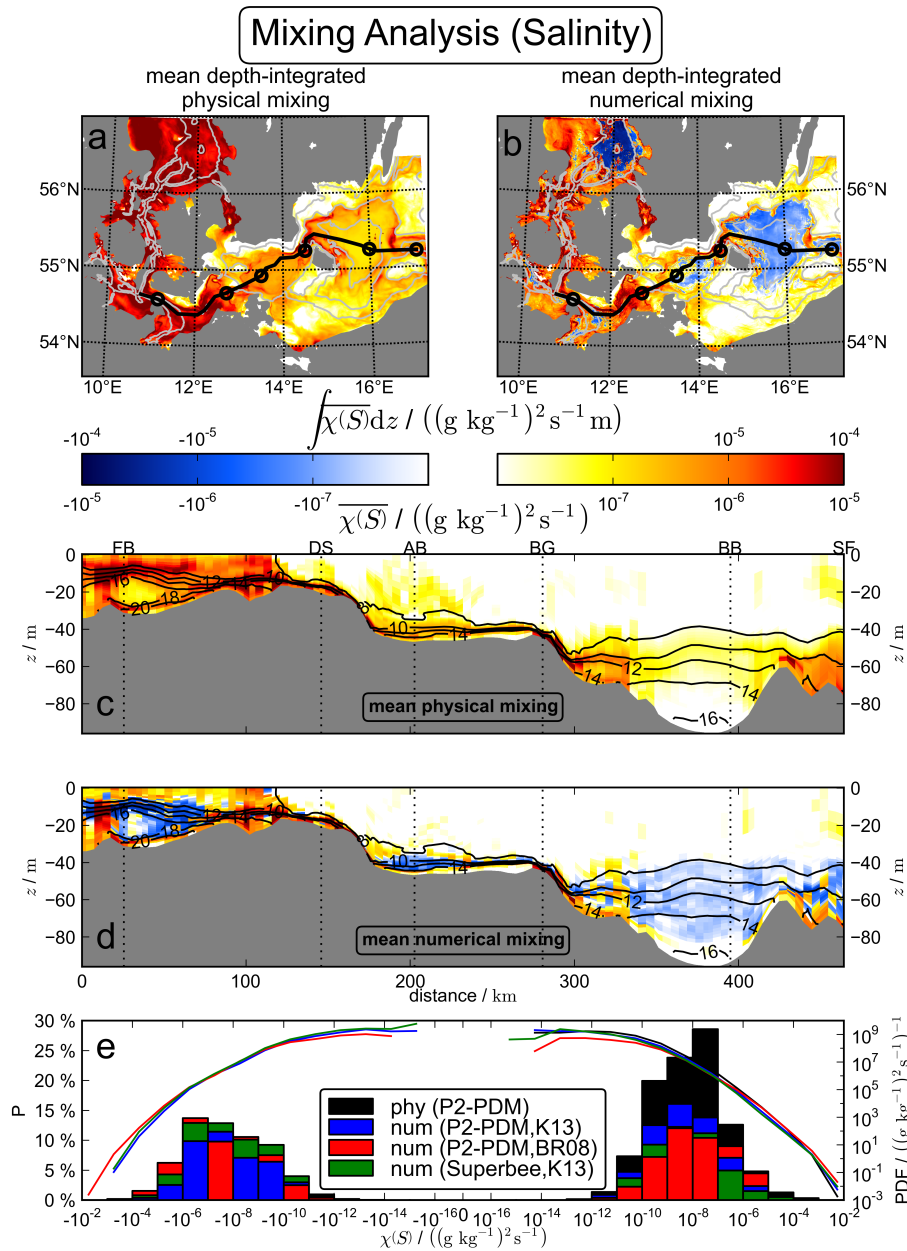


Figure 4.7.: Analysis of a realistic Western Baltic Sea model: Mixing analysis (salinity). Depth-integrated and depth-resolved mixing rates averaged over the period 19-28 Sep 2008 are shown in a,b and c,d, respectively. Results in b,d are based on K13. The ticks above the colorbars refer to a,b, the ticks below to c,d. In a,b isobaths with an interval of 25 m are depicted by grey contour lines and the black line with markers locates the transect with important stations presented in c,d. The stations are Fehmarn Belt (FB), Darss Sill (DS), Arkona Basin (AB), Bornholmshgat (BG), Bornholm Basin (BB) and Słupsk Furrow (SF). Contour lines in c,d depict isohalines. Based on hourly data along the transect, in e the statistical distribution of the physical and the numerical mixing rates diagnosed by the different analysis methods (K13, BR08) is shown for the reference simulation (lateral advection with P2-PDM) and an additional simulation (lateral advection with Superbee). Bars depict the probability (P) of a certain order of magnitude. The different bars for one order of magnitude are ordered by size, i.e. the bars with the smallest probability are in the foreground. Lines depict the PDF.

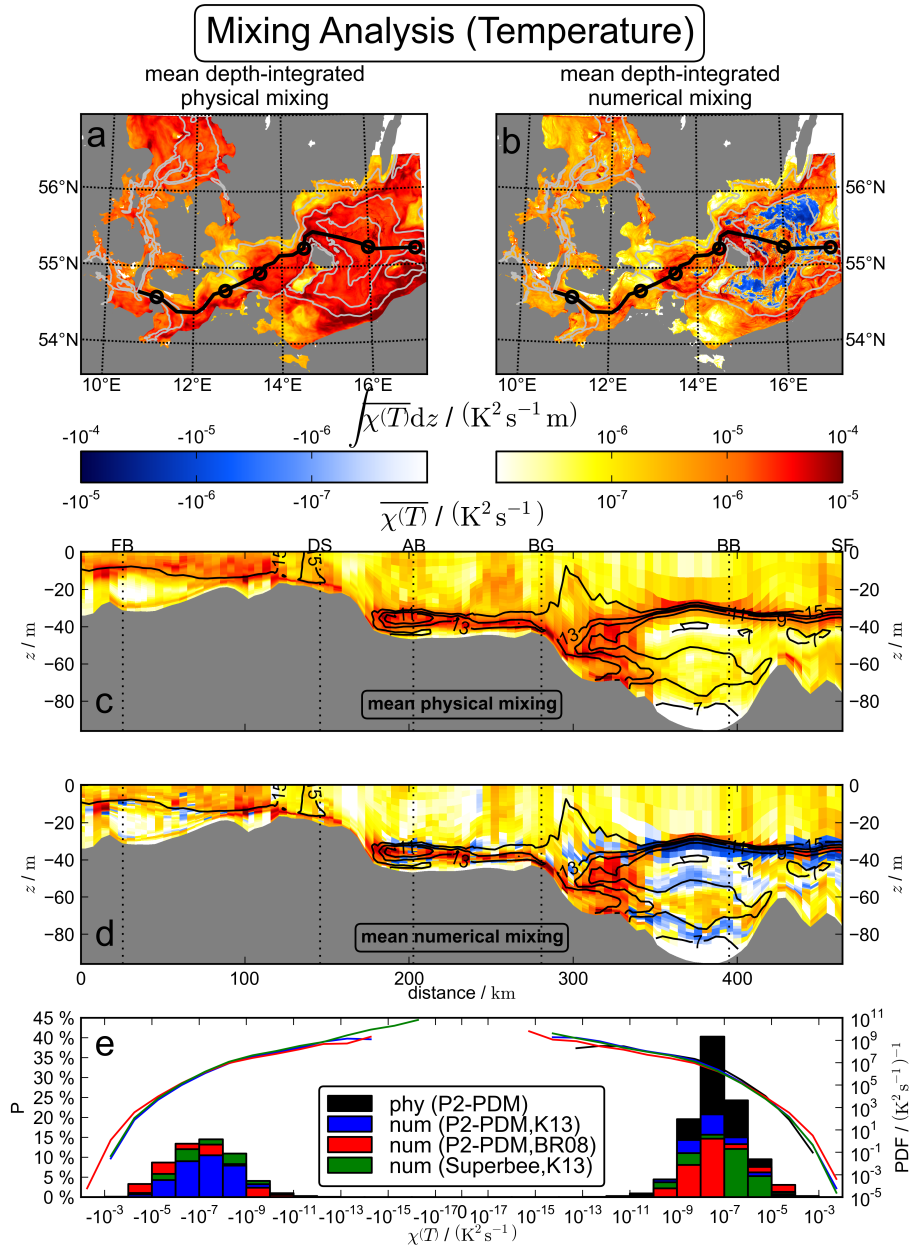


Figure 4.8.: Analysis of a realistic Western Baltic Sea model: Mixing analysis (temperature). As Figure 4.7, but in c,d with contour lines depicting the isotherms.

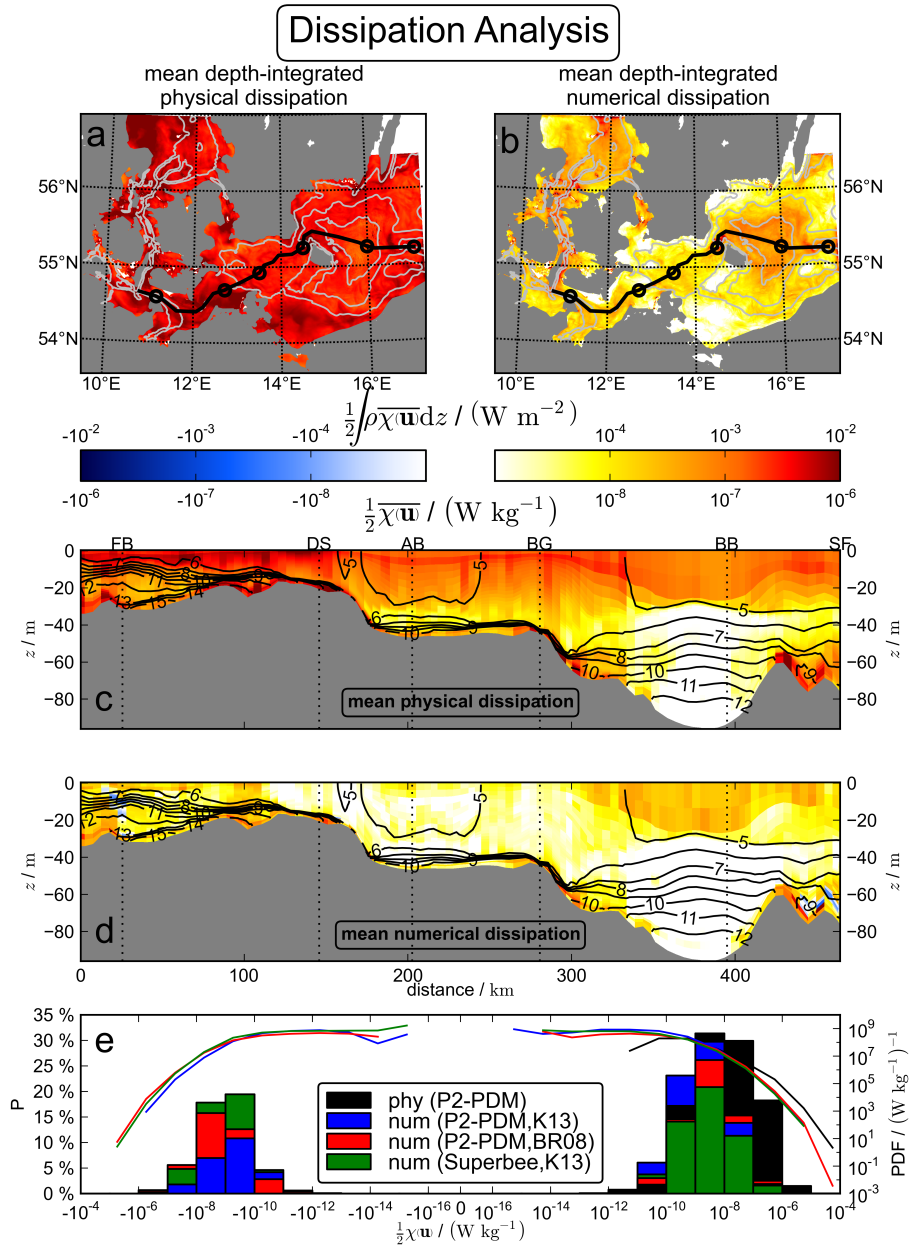


Figure 4.9.: Analysis of a realistic Western Baltic Sea model: Dissipation analysis. As Figure 4.7, but in c,d with contour lines depicting the isopycnals.

thermocline around 30 m depth and by the gradients above and below a warm intrusion. Both the halocline and thermocline were subject to physical mixing (Figures 4.7,4.8c), caused by weak shear of partly resolved near-inertial waves. The physical mixing at the thermocline also originated from wind-generated turbulence. In the shallow area between the Fehmarn Belt and the Darss Sill, near-surface wind mixing and shear due to the near-surface outflow affected both the salinity and the temperature (Figures 4.7,4.8c). Vertical advection of the sharp halocline in this area is indicated by negative numerical mixing rates (Figure 4.7d).

The slopes east of the Darss Sill, Bornholmsgat (BG) and the 60 m deep Słupsk Sill, the latter separating the 95 m deep Bornholm Basin in the east from the 90 m deep Słupsk Furrow, can also be identified as regions of strong physical mixing (Figures 4.7,4.8c). This indicates that the turbulence model captured the enhanced turbulent mixing due to differential advection and entrainment associated with bottom gravity currents (Burchard et al., 2009). This strong physical mixing was overlaid by strong numerical mixing. Due to bottom-following coordinates the transport down the slopes was performed by lateral advection causing positive numerical mixing rates (Figures 4.7,4.8d). Especially at the slopes of the Bornholm Basin the tilted model layers intersected with nearly horizontal isohalines, causing a salinity gradient along the layers and further increasing the numerical mixing induced by lateral advection. In this context, also artificial currents driven by internal pressure gradient errors contributed to the numerical mixing in sloping model layers (Hofmeister et al., 2011).

Nausch et al. (2009) reported the set in of a baroclinic inflow on 19 September 2008 and its further intensification on 25 September 2008. However, relative to the pool of saline water in the Arkona Basin, mainly originating from two earlier inflows during summer, in terms of salinity the inflow was insignificant. However, the modelled warm inflow was saline enough to intrude below colder pool water (see isotherms in Figure 4.8c). The negative numerical mixing rate of salinity suggests an uplift of the pool water above (Figure 4.7d). The positive numerical mixing rate of temperature (Figure 4.8d) also indicates lateral dynamics not represented in the analysed transect. The inflow into the Arkona Basin maintained the nearly permanent outflow of pool water into the Bornholm Basin (Burchard et al., 2009). In agreement with Rennau and Burchard (2009) and Hofmeister et al. (2011), the transverse circulation of this outflow within the sloped channel at Bornholmsgat caused a hotspot of physical and numerical mixing. In Figure 4.7c the saline inflows into the Arkona Basin and the Bornholm Basin are indicated by constricted isohalines following the topography downstream of Darss Sill and Bornholmsgat and their spreading further downstream of Bornholmsgat. In terms of temperature the inflow of warm saline water into the Bornholm Basin was more complex and associated with strong physical and positive numerical mixing rates (Figure 4.8c,d). The model results suggest that after this mixing an intrusion interleaved at its corresponding density level.

To summarise, in large areas of the model domain the diagnosed numerical mixing rates were in the same order of magnitude as their physical counterparts. The simultaneous occurrence of both vertical gradients and vertical velocities induced strong antidiffusive fluxes, indicated by negative numerical mixing rates. In contrast, the numerical dissipation of kinetic energy was at least one order of magnitude smaller than the physical one (Figure 4.9a–d). This can also be seen in the shift of frequent positive numerical dissipation rates towards lower orders of magnitude than the frequent physical dissipation rates (blue and black bars on the right-hand side of Figure 4.9e). The tails of the PDFs indicate the dominance of extreme physically induced dissipation events over extreme numerical ones. The numerically induced dissipation shows only marginal effects of vertical antidiffusive fluxes (Figure 4.9d). The order of magnitude of the most frequent negative numerical dissipation rates was still smaller than those of the most frequent physically induced dissipation rates (Figure 4.9e). In contrast, the order of magnitude of the most frequent negative numerical mixing rates coincided with those of the most frequent physically induced ones (Figures 4.7,4.8e).

Strong physical and numerical dissipation was diagnosed in dynamic near-bottom regions and in the

surface-mixed layer above the thermocline (Figure 4.9c,d). In contrast, Figure 4.9c does not show any significant mean physical dissipation in the interior of the Bornholm Basin. However, from the timeseries for the station in the Bornholm Basin (BB) periods of enhanced physical dissipation near the halocline and thermocline could be identified (not shown). Their occurrence was correlated with enhanced vertical shear, mirroring the presence of partly resolved near-inertial waves. Compared with measurements of van der Lee and Umlauf (2011) the modelled shear was too small, indicating that only an insufficient number of wave-modes could be resolved by the model. Indeed, even for near-inertial frequencies the missing higher modes are associated with horizontal wavelengths below the actual model resolution (Holtermann et al., in prep.). Thus, to sufficiently resolve near-inertial wave dynamics high-resolution nestings are necessary.

Similar to the test cases presented in Sections 4.3.1 and 4.3.2, the analysis method of Burchard and Rennau (2008) diagnosed a rather noisy distribution of dissipation and mixing rates (not shown). This results in a more frequent occurrence of large negative numerical dissipation and mixing rates (red bars on the left-hand side of Figures 4.7–4.9e). Also a shift of frequent positive numerical dissipation and mixing rates towards higher orders of magnitude can be seen.

In an additional simulation also the horizontal advection was carried out with the Superbee scheme. This change increased the regions of diagnosed negative numerical dissipation and mixing rates (not shown). The green bars in Figures 4.7–4.9e show a more frequent occurrence of these negative rates and a less frequent occurrence of the positive ones.

4.4. Conclusions

Motivated by the closed derivation of analytical variance decay (AVD), in this Chapter a general analysis of discrete variance decay (DVD) caused by advective and diffusive fluxes was established. In the lack of a general closed derivation for the local DVD rate, two methods to quantify local DVD were presented. The analysis method of Burchard and Rennau (2008) was shown to fail for implicit transport schemes and for the transversely isotropic momentum diffusion usually applied in ocean models. Furthermore, it was argued to cause significant runtime overhead. In contrast to the analysis method of Burchard and Rennau (2008), the alternative analysis method proposed in this Chapter is not based on an independent discretisation of the prognostic equation for the second moment. Instead, the fluxes of second moment are directly defined in terms of fluxes of first moment. As shown in B.4, this treatment recovers the original physically sound definition of DVD by Morales Maqueda and Holloway (2006). The alternative analysis method can be applied to implicit and nonlinear schemes and to schemes based on fractional steps. In addition to its sound foundation and its missing limitations, the proposed alternative analysis method also shows much better runtime performance. The diagnosed DVD could be separated into physical and numerical (spurious) contributions. The former represents the discrete AVD, whereas the latter originates from discretisation errors. Based on the DVD analysis, a 3D dissipation analysis was developed to quantify the loss of kinetic energy in ocean models.

In an idealised test case for 1D advection the DVD caused by popular TVD-schemes was analysed. Based on the diagnosed DVD rates, among the investigated schemes the P2-PDM scheme was concluded to have optimal shape-preserving properties for both smooth and sharp gradients. In contrast to the proposed alternative analysis method, the analysis method of Burchard and Rennau (2008) diagnosed a strongly oscillating local DVD rate, obviously complicating its interpretation.

For a benchmark test case without any physically induced DVD the interplay of both numerical dissipation and mixing provoked an analysis of the energy composition. Numerically dissipated energy could be quantified by means of the developed 3D dissipation analysis. In this context, with physical

sources and sinks of energy properly considered, the inconstancy of the global sum of potential, kinetic and dissipated energy indicates the presence of an inconsistent model discretisation. Recently Marsaleix et al. (2008) identified such inconsistencies within the ocean model SYMPHONIE. Also for this test case, with the analysis method of Burchard and Rennau (2008) rather noisy local dissipation and mixing rates were diagnosed.

Finally, the physically and numerically induced dissipation and mixing in a realistic Western Baltic Sea model were analysed. In particular the results of the analysed transect along the pathway of inflows and the results of the dissipation analysis add to the findings of Rennau and Burchard (2009); Hofmeister et al. (2011); Burchard and Gräwe (2013). In contrast to the diagnosed mixing, within the analysed simulation period of this highly dynamic region the numerical dissipation was at least one order of magnitude lower than the physically induced one.

As demonstrated in all test cases, the proposed alternative DVD analysis method provides a reliable diagnostic tool for the local quantification of physically and numerically induced dissipation and mixing. The developed 3D dissipation analysis offers the assessment of momentum advection schemes and subgrid-scale closures in ocean models. Both are crucial for the simulation of mesoscale and submesoscale dynamics. Furthermore, models with unstructured grids can optimise their meshes based on the diagnosed numerical DVD (Holleman et al., 2013).

The quantification of physically and numerically induced DVD offers an estimation of their individual contribution to the total (physical and numerical) DVD. However, their mutual influence inhibits conclusions about their absolute impact on the total DVD. For example, improved schemes might decrease the numerically induced DVD, leaving sharper gradients to the physically induced DVD, and thus still can cause a similar total DVD. Nevertheless, an increased contribution of physically induced DVD based on calibrated turbulence parameterisations is of course preferable (Hofmeister et al., 2011). The spatio-temporal influence further complicates the interpretation, e.g. in downstream areas improved schemes can cause stronger DVD than poor schemes, because the latter already smoothed gradients upstream (Rennau and Burchard, 2009).

The developed DVD analysis does distinguish between the directions of the interfacial fluxes, not between along- and across-isopycnal directions. Therefore, a future challenge will be the local quantification of diapycnal mixing of an individual tracer, providing more detailed information than global measures utilised by Griffies et al. (2000); Getzlaff et al. (2010, 2012); Ilicak et al. (2012).

Chapter 5.

Inclusion of nonhydrostatic dynamics

The increasing demand for the investigation of nonhydrostatic dynamics in ocean modelling requires crucial modifications to models applying the hydrostatic pressure assumption. Within many studies the capability of the pressure-correcting projection method for the inclusion of the missing nonhydrostatic pressure contribution into an existing hydrostatic model kernel was verified. It provides accurate results but also requires computational (and implementational) effort for solving a Poisson equation for the pressure correction.

In contrast, some studies were based on an alternative approach that does not require the inversion of a Poisson equation. Within this alternative approach the nonhydrostatic pressure contribution is calculated by an explicit vertical integration of the additional nonhydrostatic terms in the balance of vertical momentum. Since ocean models are not intended to replace classical engineering tools and are usually applied to nearly hydrostatic flows, this straight-forward extension of the hydrostatic procedure is an interesting option. However, the feasibility of the alternative approach was not tested within a full 3D explicit mode-splitting model yet. Furthermore, the nonhydrostatic capability of the alternative approach has so far not been validated against well known nonhydrostatic benchmark test cases. In order to assess the potential of the alternative approach for future ocean modelling applications, in the present study these required but still missing investigations are carried out.

To demonstrate the necessary modifications to an explicit mode-splitting hydrostatic model kernel, the extension of the General Estuarine Transport Model (GETM) is outlined. The simulation results of laboratory and idealised oceanic test cases are presented and compared to analytical theory, laboratory experiments and other numerical simulations. This validation indicates the nonhydrostatic capability of the extended GETM. However, stability issues limited the efficiency and the applicability of the straight-forward inclusion of nonhydrostatic dynamics.

5.1. Introduction

Except for a few strongly idealised cases, the governing equations of fluid dynamics cannot be solved analytically. Thus, in addition to laboratory experiments and field campaigns, numerical simulations have become an important part of the scientific investigation of fluid dynamics.

In Computational Fluid Dynamics (CFD) the deployment of accurate approximations and the development of efficient numerical procedures is essential in order to limit the computational effort and thereby to facilitate the practical use of numerical models for a certain kind of applications. The *hydrostatic pressure assumption* is a widespread approximation in geophysical disciplines. The degeneration of the balance of vertical momentum from a prognostic equation for the vertical velocity to a diagnostic equation for the hydrostatic pressure greatly simplifies the governing Navier-Stokes Equations. Furthermore, this approximation implies significant numerical advantages: in compressible fluids vertical acoustic waves are eliminated, permitting a less restrictive numerical time step, and

in incompressible fluids the expensive solution of a Poisson equation for the pressure can be avoided (Durran, 2010).

However, by neglecting the nonhydrostatic pressure contribution the governing equations are missing a piece of physics that may become important, especially within today's feasible high numerical resolutions and also for diverse processes apart from classical engineering applications. For example, the hydrostatic pressure assumption implies the traditional approximation. However, not only for mesoscale applications the neglected accelerations proportional to the horizontal Coriolis parameter can be relevant (Mahadevan et al., 1996; Gerkema et al., 2008). In general the correct simulation of the vertical velocity is essential to study flow separation and the formation of recirculation patterns, which is relevant for sediment transport (Johns, 1991). Besides hydrostatic also nonhydrostatic internal waves are an important transport mechanism for energy in the ocean and lakes. These are usually generated by tides and wind (Shen and Evans, 2004; Xing and Davies, 2007; Carter et al., 2012). Especially during nonhydrostatic shoaling and breaking events at sloping boundaries, internal waves contribute to mixing (Horn et al., 2000; Legg and Adcroft, 2003; Thiem and Berntsen, 2009; Venayagamoorthy and Fringer, 2012) and can affect the ecosystem (Lai et al., 2010a). Further, nonhydrostatic processes occur in connection with strong buoyancy-driven flows, including convection events (Kämpf and Backhaus, 1998; Marshall et al., 1998) and entraining plumes caused by exchange flows over sills and shelf edges (Özgökmen and Chassignet, 2002; Heggelund et al., 2004).

Thus, the option to relax the hydrostatic pressure assumption will greatly extend the applicability of ocean models. There are several solution methods available for the incompressible Navier-Stokes Equations including the additional nonhydrostatic terms. Although very accurate solutions without any decoupling errors can be obtained, for practical ocean modelling applications an implicit discretisation seems to still be limited by today's computational power (Yuan and Wu, 2004; Labeur and Pietrzak, 2005). Streamfunction-vorticity-methods provide a suitable treatment of the incompressible Navier-Stokes Equations (Shen and Evans, 2004), but they increase the number of unknown quantities in 3D and aggravate the prescription of boundary conditions (Fletcher, 1988). Adopting solution methods for compressible flows, Chorin (1967a) proposed the Artificial Compressibility Method (ACM). Principally intended for steady flows, the ACM can be applied to unsteady flows (Chorin, 1967b; Lee et al., 2006), but may become unstable due to the high stiffness of the modified incompressibility constraint. Based on the projection approach (Chorin, 1968; Témam, 1969), van Kan (1986) proposed the pressure-correcting projection method. Moukalled and Darwish (2000) showed that the popular SIMPLE-methods of engineering CFD are iterative pressure-correction methods. Klingbeil (2009) reviewed the projection approach and how the pressure-correcting projection method can be built on top of an existing hydrostatic model kernel to include the missing nonhydrostatic pressure contribution.

In the past several former hydrostatic models were extended according to the pressure-correcting projection method. Jankowski (1999) extended the TELEMAC-3D model of Janin et al. (1992). Kanarska and Maderich (2003) presented the first extension of an explicit mode-splitting model (POM; Blumberg and Mellor, 1987). In the following years other explicit mode-splitting models were modified as well. The inclusion of the nonhydrostatic pressure contribution into BOM (Berntsen, 2000) was proposed by Heggelund et al. (2004) and simplified by Berntsen and Furnes (2005). Kanarska et al. (2007) extended ROMS (Shchepetkin and McWilliams, 2005), Lai et al. (2010b) modified FVCOM (Chen et al., 2003), and recently Auclair et al. (2011) presented in detail the nonhydrostatic extension of SYMPHONIE (Marsaleix et al., 2008).

Although the pressure-correcting projection method completely uses the existing hydrostatic model kernel, the implementational and computational effort to solve the additional Poisson equation must be considered. In 3D the matrix to invert has already 7 diagonals within z -coordinates, but even 15 diagonals in σ -coordinates (Keilegavlen and Berntsen, 2009).

Within many ocean and estuarine flows the dominant part of the dynamic relevant pressure is hydro-

static. In these cases nonhydrostatic effects rather represent a small correction to the leading-order processes and solution methods that track the nonhydrostatic pressure contribution less complex might be sufficient. A straight-forward inclusion of the missing nonhydrostatic pressure contribution into existing hydrostatic model kernels can be based on the explicit vertical integration of the additional nonhydrostatic terms within the balance of vertical momentum and on the subsequent consideration in the horizontal pressure gradient. Although this alternative approach omits the solution of a Poisson equation, its application was reported only in a few publications.

Based on the dispersion relation for internal gravity waves and series expansion in terms of the aspect ratio, Orlanski (1981) showed that the hydrostatic inviscid equations are only a zeroth-order approximation. He derived a system of equations including also the first-order terms. Within the final algorithm implemented into an atmospheric model the hydrostatic quantities were corrected based on the alternative approach sketched above. Numerical experiments of atmospheric front dynamics and convection were satisfying.

Dietrich et al. (1987) mentioned the inclusion of vertically integrated nonhydrostatic terms for the simulation of mild nonhydrostatic processes in the framework of the (hydrostatic) rigid-lid ocean modelling system SOMS. First nonhydrostatic results were presented by Lin and Dietrich (1994) for convective adjustment experiments on different scales. Also the succeeding rigid-lid DieCAST model (Dietrich and Ko, 1994) was extended according to this approach with an iterative adjustment of the vertical acceleration (Dietrich and Lin, 2002).

Johns (1991) and Johns and Xing (1993) simulated the 2D-Vertical (2DV) cross-sectional and 3D flow separation over the lee slope of sandwaves. The prognostic integration was continued until a steady state solution was achieved. At each stage an iterative procedure subsequently adjusted both the steady part of the nonhydrostatic pressure and the velocity field. Li and Johns (2001) extended the 2DV model of Johns (1991) to unsteady flows. Therefore a new prognostic variable was defined as the combination of the horizontal velocity and the unsteady component of the horizontal nonhydrostatic pressure gradient. The use of a double-iterative procedure at each time stage increased the computational effort. The model was applied to weakly nonhydrostatic surface waves propagating over variable topography.

Gaarhuis (1995) analysed iterative procedures for unsteady 2DV equations in both z - and σ -coordinates. The final surface elevation, the final velocity and the final nonhydrostatic pressure contribution were calculated subsequently from the linearised and horizontally inviscid equations until convergence occurred. The convergence for the alternative approach was argued to be more efficient than that for the ACM. Contrary to the projection method, for a decreasing aspect ratio the efficiency of the alternative approach increased. However, in σ -coordinates it was impossible to simulate a standing wave in a basin.

Within the studies mentioned above the straight-forward inclusion of nonhydrostatic dynamics was applied either to rigid-lid (Dietrich et al., 1987; Dietrich and Lin, 2002), steady-state (Johns, 1991; Johns and Xing, 1993), 2DV (Li and Johns, 2001) or governing equations with other limitations (Gaarhuis, 1995). However, the straight-forward extension of a full 3D explicit mode-splitting model was not tested yet. Furthermore, the nonhydrostatic capability of the straight-forward inclusion has not yet been validated against well known nonhydrostatic benchmark test cases. In order to assess the potential of the straight-forward inclusion of nonhydrostatic dynamics for future ocean modelling applications, these required but still missing investigations are carried out in the present study.

The governing equations, the hydrostatic pressure assumption, its (in)validity and an outline for the straight-forward extension of the hydrostatic procedure are presented in Section 5.2. Details of the implementation into the existing explicit mode-splitting model kernel of the General Estuarine Transport Model (GETM) are provided in Section 5.3. Numerical results that demonstrate the nonhydrostatic

capability of the extended GETM are presented in Section 5.4. A critical discussion of the straight-forward inclusion of nonhydrostatic dynamics is given in Section 5.5. In Section 5.6 the Chapter is summarised and an outlook is given.

5.2. Basics

5.2.1. Breakdown of the hydrostatic pressure assumption

The validity of the hydrostatic pressure assumption, introduced in Section 2.2.2, is limited and in general the inherent traditional approximation is not justified. For example, the argumentation of Phillips (1966) based on thin-layer geometry was disproved by Veronis (1968). White and Bromley (1995) estimated the limits for the validity of the traditional approximation. Different phenomena that cannot be described under the traditional approximation are discussed by Gerkema et al. (2008). The hydrostatic pressure assumption can be relaxed to the *quasi-hydrostatic approximation* by neglecting all terms except $f_h u$ in (2.9) and by retaining $f_h w$ in (2.1b) (White and Bromley, 1995; Marshall et al., 1997).

The other terms in (2.9) are not negligible, if significant vertical velocity on small spatio-temporal scales is present. Local vertical velocity may be initialised by e. g. interaction with structures, steep waves or a rapidly varying bottom topography, weak or unstable stratification or simply by small-scale spatio-temporal fluctuations (caused by e. g. waves and turbulence). More conditions for the breakdown of the hydrostatic pressure assumption can be deduced from (2.17). Of course, these are only general guidelines and the (in)validity of the hydrostatic pressure assumption must be assessed for every process individually.

Again the need for sufficiently high spatio-temporal resolution is addressed to resolve the small-scale characteristics mentioned above and thus to simulate possible nonhydrostatic effects at all. Vice versa, the continuous improvement of the resolution of a numerical model demands the inclusion of nonhydrostatic dynamics. For linear surface gravity waves with wavenumber k the shallow water approximation is valid if $kH \ll 1$. Within a numerical discretisation of resolution Δx the maximum resolved wavenumber is given by $k = \mathcal{O}(\Delta x^{-1})$. Thus, if the necessary condition $\frac{H}{\Delta x} \ll 1$ is violated, the hydrostatic pressure assumption is already invalid. In this case nonhydrostatic dynamics must be considered to avoid a wrong hydrostatic modelling of inherently nonhydrostatic waves present within the given resolution.

5.2.2. Outline of a straight-forward nonhydrostatic extension

In Section 3.1 the governing equations under the hydrostatic pressure assumption were summarised. According to (2.10b) a straight-forward inclusion of the missing nonhydrostatic pressure contribution can be based on the explicit vertical integration of the additional nonhydrostatic terms in the balance of vertical momentum (already collected in (2.9) as b_{nh}),

$$p_{nh} = \int_z^{\eta} \rho_0 b_{nh} dz, \quad (5.1)$$

and the subsequent inclusion into the balance of horizontal momentum (3.2b) and (3.2c) via (2.8).

The individual integration of b_{nh} and the subsequent evaluation of the corresponding horizontal pressure gradient can be omitted. Since these operations are already carried out for the buoyancy b in (2.13), they would be redundant and would wastefully increase the computational (and implementational) effort. Instead, the combination of (2.8), (5.1) and (2.13) yields

$$p = p \Big|_{z=\eta} + \rho_0 g (\eta - z) - \rho_0 \int_z^\eta (b - b_{\text{nh}}) dz \quad (5.2)$$

and suggests the use of a corrected buoyancy ($b - b_{\text{nh}}$). Thus, if the buoyancy b in (2.13) is replaced by the corrected buoyancy ($b - b_{\text{nh}}$), the nonhydrostatic pressure contribution is included into an existing hydrostatic model kernel in a consistent way. Furthermore, (5.1) and thus (5.2) inherits the analytical Dirichlet condition for the nonhydrostatic pressure contribution exactly at the free surface $p_{\text{nh}} \Big|_{z=\eta} = 0$.

The just described inclusion of the nonhydrostatic pressure contribution into the hydrostatic equations (3.2a)–(3.2c) and the inclusion of the additional Coriolis component $f_{\text{h}}w$ in (3.2b) yields the following nonhydrostatic governing equations:

$$0 = \frac{\partial u}{\partial x} + \frac{\partial v}{\partial y} + \frac{\partial w}{\partial z}, \quad (5.3a)$$

$$\begin{aligned} & \frac{\partial u}{\partial t} + \frac{\partial}{\partial x} \{uu\} + \frac{\partial}{\partial y} \{vu\} + \frac{\partial}{\partial z} \{wu\} + f_{\text{h}}w - f_{\text{v}}v \\ &= - \frac{\partial}{\partial x} \left\{ \frac{p \Big|_{z=\eta}}{\rho_0} \right\} - g \frac{\partial \eta}{\partial x} + \frac{\partial}{\partial x} \int_z^\eta (b - b_{\text{nh}}) dz + \frac{\partial}{\partial z} \left\{ (\nu + \nu^{\text{turb,v}}) \frac{\partial u}{\partial z} \right\} + F_{\text{x}}^{\text{h}}, \end{aligned} \quad (5.3b)$$

$$\begin{aligned} & \frac{\partial v}{\partial t} + \frac{\partial}{\partial x} \{uv\} + \frac{\partial}{\partial y} \{vv\} + \frac{\partial}{\partial z} \{wv\} + f_{\text{v}}u \\ &= - \frac{\partial}{\partial y} \left\{ \frac{p \Big|_{z=\eta}}{\rho_0} \right\} - g \frac{\partial \eta}{\partial y} + \frac{\partial}{\partial y} \int_z^\eta (b - b_{\text{nh}}) dz + \frac{\partial}{\partial z} \left\{ (\nu + \nu^{\text{turb,v}}) \frac{\partial v}{\partial z} \right\} + F_{\text{y}}^{\text{h}}, \end{aligned} \quad (5.3c)$$

with

$$b_{\text{nh}} = \frac{\partial w}{\partial t} + \frac{\partial}{\partial x} \{uw\} + \frac{\partial}{\partial y} \{vw\} + \frac{\partial}{\partial z} \{ww\} - f_{\text{h}}u - \frac{\partial}{\partial z} \left\{ \nu \frac{\partial w}{\partial z} \right\}. \quad (5.4)$$

These equations are equivalent to the original equations (2.1a)–(2.1d), except for the forces originating from the divergence of the deviatoric stress tensor. Since the applications in the present thesis

are either DNS-like simulations (without turbulent stresses) or close to hydrostatic, for the forces originating from the divergence of the turbulent stress tensor still the hydrostatic pressure assumption is applied. Anyhow, the effect of these neglected diffusive terms is assumed to be small.

The resulting algorithm can be outlined as follows (initialisation of b_{nh} to zero):

1. Calculation of the pressure p by means of (5.2),
2. Prognostic integration of (u, v) according to (5.3b) and (5.3c),
3. Diagnosing of the vertical velocity w by means of (2.19),
4. Calculation of b_{nh} according to (5.4),
5. Integration of tracer equations and update of the buoyancy b (2.12),
6. Restart with step 1.

The only difference to the hydrostatic procedure is the additional step 4.

It should be noted that, in contrast to the projection method (based on the coupling of the incompressibility constraint and the momentum equations), this straight-forward extension decouples the balance of horizontal momentum (step 2), the incompressibility constraint (step 3) and the balance of vertical momentum (step 4).

5.3. Straight-forward extension of the General Estuarine Transport Model

5.3.1. Transformation to general vertical coordinates and layer integration

Layer-integration of the extended governing equations (5.3a)–(5.3c) yields equations similar to (3.5a)–(3.5c), except for the corrected buoyancy ($b-b_{nh}$) and the additional Coriolis term:

$$0 = \frac{\partial h_k}{\partial t} + \frac{\partial}{\partial x} \{h_k u_k\} + \frac{\partial}{\partial y} \{h_k v_k\} + \left(w_{k+1/2}^s - w_{k-1/2}^s \right), \quad (5.5a)$$

$$\begin{aligned} & \frac{\partial}{\partial t} \{h_k u_k\} + \frac{\partial}{\partial x} \{h_k u_k u_k\} + \frac{\partial}{\partial y} \{h_k v_k u_k\} + \left(w_{k+1/2}^s u_{k+1/2} - w_{k-1/2}^s u_{k-1/2} \right) + f_h h_k w_k - f_v h_k v_k \\ &= -h_k \frac{\partial}{\partial x} \left\{ \frac{p|_{z=\eta}}{\rho_0} \right\} - h_k g \frac{\partial \eta}{\partial x} + \left(\tau_{x,k+1/2}(u, v) - \tau_{x,k-1/2}(u, v) \right) + h_k \tilde{F}_x^h(u_k, v_k, h_k) \\ & \quad + h_k F_{x,k}^{IP}(b-b_{nh}), \end{aligned} \quad (5.5b)$$

$$\begin{aligned} & \frac{\partial}{\partial t} \{h_k v_k\} + \frac{\partial}{\partial x} \{h_k u_k v_k\} + \frac{\partial}{\partial y} \{h_k v_k v_k\} + \left(w_{k+1/2}^s v_{k+1/2} - w_{k-1/2}^s v_{k-1/2} \right) + f_v h_k u_k \\ &= -h_k \frac{\partial}{\partial y} \left\{ \frac{p|_{z=\eta}}{\rho_0} \right\} - h_k g \frac{\partial \eta}{\partial y} + \left(\tau_{y,k+1/2}(u, v) - \tau_{y,k-1/2}(u, v) \right) + h_k \tilde{F}_y^h(u_k, v_k, h_k) \\ & \quad + h_k F_{y,k}^{IP}(b-b_{nh}). \end{aligned} \quad (5.5c)$$

According to (5.4) the layer-averaged nonhydrostatic buoyancy is calculated in terms of both, the grid-related vertical velocity w^s and the vertical velocity w , with the latter provided by (3.9):

$$\begin{aligned} b_{nh,k} = \frac{1}{h_k} \left[\frac{\partial}{\partial t} \{h_k w_k\} + \frac{\partial}{\partial x} \{h_k u_k w_k\} + \frac{\partial}{\partial y} \{h_k v_k w_k\} + \left(w_{k+1/2}^s w_{k+1/2} - w_{k-1/2}^s w_{k-1/2} \right) \right. \\ \left. - f_h h_k u_k - \left(\nu \frac{\partial w}{\partial z} \Big|_{z=z_{k+1/2}} - \nu \frac{\partial w}{\partial z} \Big|_{z=z_{k-1/2}} \right) \right]. \end{aligned} \quad (5.6)$$

5.3.2. Explicit mode-splitting

The replacement of the buoyancy b by the corrected buoyancy ($b - b_{\text{nh}}$) is also mirrored in the interaction terms (3.14b), changing to:

$$S_{\alpha}^{\text{B}} = - \sum_{k=1}^{k_{\text{max}}} h_k F_{\alpha,k}^{\text{IP}} (b - b_{\text{nh}}). \quad (5.7)$$

5.3.3. Implementation

Since GETM already provides modular routines for the calculation of the vertical velocity (in the hydrostatic model kernel only used for output) and for the explicit calculation of the advection terms,

$$\text{ADV}(w_k) = \frac{\partial}{\partial x} \{h_k u_k w_k\} + \frac{\partial}{\partial y} \{h_k v_k w_k\} + \left(w_{k+1/2}^s w_{k+1/2} - w_{k-1/2}^s w_{k-1/2} \right), \quad (5.8)$$

the straight-forward extension requires only minimal modifications to the existing hydrostatic model kernel. Actually, only the calculation of the nonhydrostatic buoyancy (5.6) must be implemented. The implementation of complicated numerical algorithms (e. g. parallelised Poisson solver as needed for the projection method) is not necessary.

The spatial discretisation of (5.6) is based on the same concepts as described in Burchard and Bolding (2002) for the hydrostatic kernel. Similar to the spatial staggering, in GETM the equations are staggered also in time. Velocities are defined at half time stages $^{(n+1/2)}$ and all other quantities at full time stages $^{(n+1)}$. The temporal discretisation of (5.6) is given by

$$b_{\text{nh},k}^{(n,l)} \approx \frac{1}{h_k^{(n+1/2)}} \left[\frac{(h_k w_k)^{(n+1/2)} - (h_k w_k)^{(n-1/2)}}{\Delta t_{3\text{D}}} + \text{ADV} \left(w_k^{(n+1/2)} \right) - f_{\text{h}} (h_k u_k)^{(n+1/2)} - \left(\nu \frac{\partial w}{\partial z} \Big|_{z=z_{k+1/2}}^{(n+1/2)} - \nu \frac{\partial w}{\partial z} \Big|_{z=z_{k-1/2}}^{(n+1/2)} \right) \right]. \quad (5.9)$$

with index $l \in [1, N_{\text{it}}]$ denoting the iteration loop (see algorithm below).

The time lag induced by this discretisation shows the decoupled treatment of the governing equations mentioned at the end of Section 5.2.2. However, due to a sufficiently small time step or an iteration procedure the time lag can be minimised and convergence can be forced.

With N_{it} being a predefined number of iterations, the final algorithm implemented in GETM for this study is given by:

1. Cycle of depth-averaged integrations,
2. Update of layer heights $h_k^{(n+1)}$ and $h_k^{(n+1/2)}$,
3. Iteration cycle for $l = 1, N_{\text{it}}$:
 - a) Integration of (5.5b) and (5.5c) with $b_{\text{nh}}^{(n,l-1)}$ and shifting of $(u, v)^{(n+1/2)}$ -profiles,
 - b) Diagnosing of the grid-related vertical velocity $w^{s,(n+1/2)}$ by means of (5.5a),
 - c) Diagnosing of the vertical velocity $w^{(n+1/2)}$ by means of (3.9) and calculation of $b_{\text{nh}}^{(n,l)}$ according to (5.9),
4. Integration of tracer equations and update of the buoyancy $b^{(n+1)}$ (2.12),
5. Update of interaction terms (e. g. (5.7) with $b_{\text{nh}}^{(n+1,0)} = b_{\text{nh}}^{(n,N_{\text{it}})}$) and restart with step 1.

Since $b_{\text{nh}}^{(0,0)} = 0$, the original hydrostatic algorithm can simply be recovered by $N_{\text{it}} = 1$ and skipping step 3c).

5.3.4. Stability issues

The decoupling of the incompressibility constraint and the Navier-Stokes Equations does not only raise convergence issues but also stability issues. To suppress temporal fluctuations induced and amplified by (5.9), the following cumulative filter with weight $\theta \in]0, 1]$ can be optionally applied to b_{nh} :

$$\bar{b}_{\text{nh}}^{(n,l)} = \theta b_{\text{nh}}^{(n,l)} + (1 - \theta) \bar{b}_{\text{nh}}^{(n,l-1)}. \quad (5.10)$$

As derived in Appendix C, the filter weight θ and the number of iterations N_{it} determine the temporal resolution of nonhydrostatic effects Δt_{nh} . This can be improved either by decreasing the internal time step Δt_{3D} or by increasing the number of iterations N_{it} .

Most of the computational effort originates in the higher-order directional-split advection of the different quantities. Within the iteration cycle only the three velocity components are advected, whereas outside the iteration cycle the thermodynamic quantities and in complex simulations also the turbulent and a number of biogeochemical tracers are advected. In this context the computational effort of the iteration cycle is only a fraction of the effort of a whole model time step. Thus, the increase of the number of iterations N_{it} is preferable.

5.4. Simulations with the extended GETM

Despite a growing number of realistic 3D applications (e.g. Tseng et al., 2005; Jachec et al., 2006; Tseng and Breaker, 2007; Wang et al., 2009; Zhang et al., 2011; Kang and Fringer, 2012), non-hydrostatic simulations are still mainly limited to idealised research purposes. But before applying a

model to idealised or even realistic scenarios, its nonhydrostatic capability must be verified. In this Section the nonhydrostatic capability of the extended GETM is assessed by different nonhydrostatic benchmark test cases. In addition results of an idealised application to tidally induced internal waves in the lee of a sill are presented. Finally, with the extended GETM the importance of nonhydrostatic effects in a realistic application to the Western Baltic Sea is investigated.

5.4.1. Dispersing interfacial waves

With this test case the soliton regime of the laboratory experiments from Horn et al. (2001) is simulated. In the laboratory a closed rectangular tank, filled with two stably stratified fluids of different density, was reset quickly from a tilted position to set up an inclined pycnocline. This position of the pycnocline determined the magnitude of shear and nonlinear steepening and therefore the regime of the resulting flow. Recently, nonhydrostatic simulations of Wadzuk (2004), Stashchuk et al. (2005), Kanarska et al. (2007) and Bergh and Berntsen (2010) could reproduce several regimes of interfacial waves and instabilities investigated by Horn et al. (2001).

The experiment of the soliton regime presented in Fig. 4 of Horn et al. (2001) was chosen for DNS-like rigid-lid computations with full-slip conditions at all boundaries. The spatio-temporal resolution was adopted from Kanarska et al. (2007): $\Delta t_{3D} = 0.05$ s, $\Delta x = 15$ mm and $\Delta z = 3.625$ mm. A filter weight of $\theta = 1\%$ and $N_{it} = 50$ implied $\Delta t_{nh} = 0.5$ s as the temporal resolution of nonhydrostatic effects. The horizontal resolution is fine enough to sufficiently suppress artificial dispersion due to numerical truncation errors (Vitousek and Fringer, 2011). For these settings 93% of the total runtime were caused by the additional nonhydrostatic computations.

The simulation under the hydrostatic pressure assumption failed due to the lack of physical dispersion (not shown). In contrast, the nonhydrostatic GETM simulation agrees well with the laboratory experiment of Horn et al. (2001) and indicates the need for the nonhydrostatic pressure contribution to model correctly the balance of nonlinear steepening and the dispersive effects needed for the disintegration into solitary waves (Figures 5.1 and 5.2). The propagation speed of the solitary wave train coincided with the laboratory experiment. However, slightly increased amplitudes and missing trailing waves at the end of the simulation indicate a slight deviation between the simulated ratio of dispersive to nonlinear effects and the one observed by Horn et al. (2001).

5.4.2. Lock-exchange

The classical setup of a withdrawn vertical gate between two fluids of different density initialises idealised gravity currents (Simpson, 1982). Under the hydrostatic pressure assumption a wave equation for the depth of the pycnocline can be derived from the linearised equations, whose d'Alembert solution predicts a pair of rectangular fronts propagating in opposite directions (Jankowski, 1999). However, the typical shape of the heads and the instabilities at the shear interface, observed in numerous laboratory experiments and (nonhydrostatic) numerical simulations (e.g. by Härtel et al., 2000; Kanarska and Maderich, 2003; Berntsen et al., 2006; Fringer et al., 2006), cannot be described by this solution.

DNS-like rigid-lid computations (but with viscosities and diffusivities set to $1 \times 10^{-6} \text{ m}^2\text{s}^{-1}$) for the setup described in Berntsen et al. (2006) were carried out with $\Delta t_{3D} = 0.025$ s, $\Delta x = 2$ mm and $\Delta z = 1$ mm. A filter weight of $\theta = 0.1\%$ and $N_{it} = 30$ implied $\Delta t_{nh} = 3.85$ s as the 99%-interval of nonhydrostatic effects. For these settings 89% of the total runtime were caused by the additional nonhydrostatic computations.

As shown in Figure 5.3, the nonhydrostatic GETM simulation could reproduce the speed of the front and the number and size of the typical Kelvin-Helmholtz billows at the shear interface.

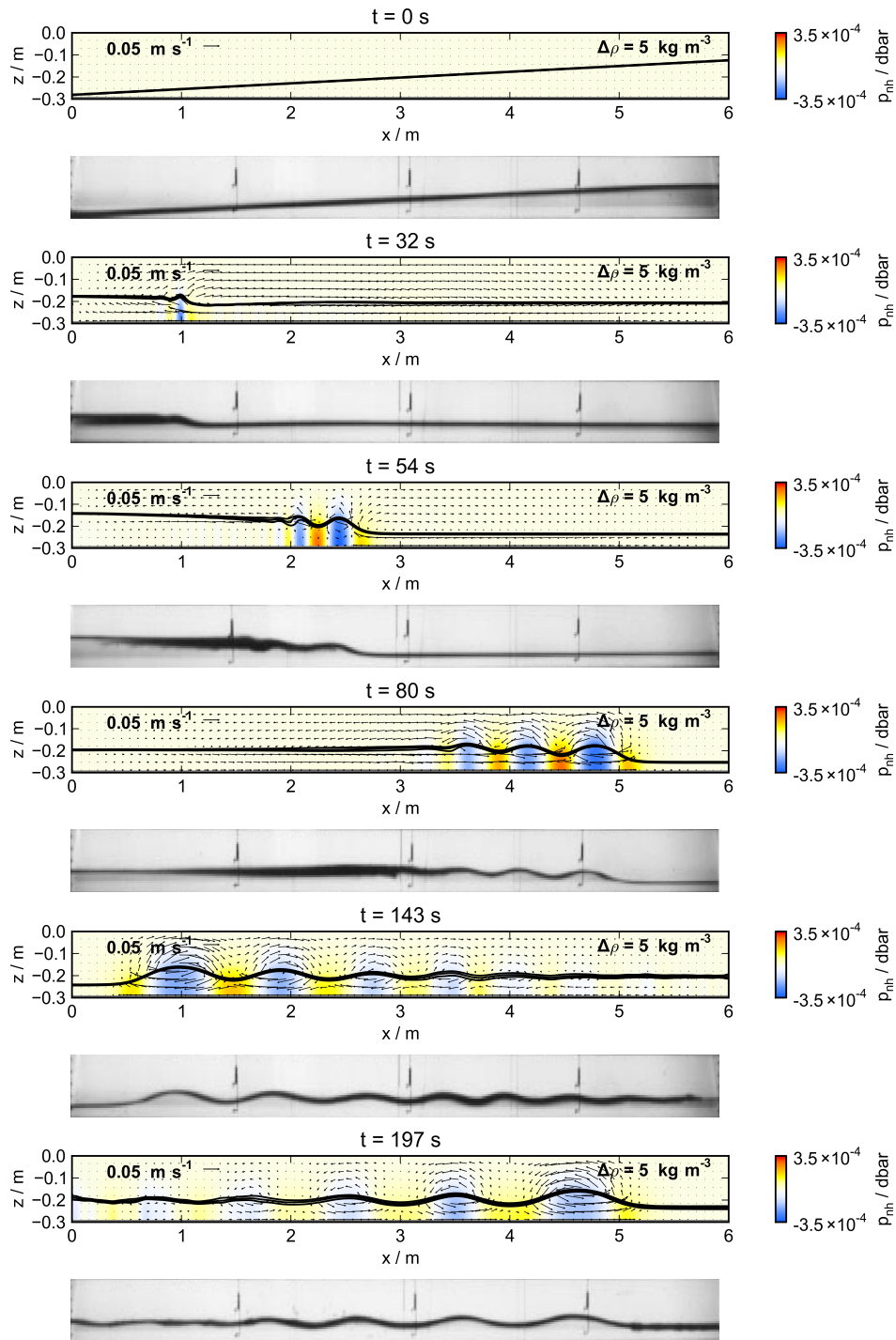


Figure 5.1.: Dispersing interfacial waves: Snapshots. Series of snapshots from the non-hydrostatic GETM simulation and from the laboratory experiment of Horn et al. (2001). The simulation results include isopycnals (black lines with $\Delta\rho = 5 \text{ kg m}^{-3}$), the nonhydrostatic pressure contribution (coloured) and the velocity (arrows). The photographs of the laboratory experiments show the pycnocline and are taken from Fig. 4 of Horn et al. (2001).

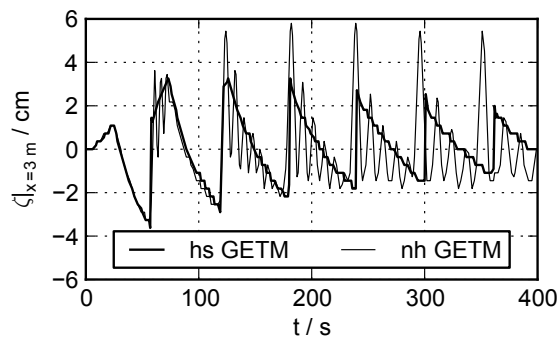


Figure 5.2.: Dispersing interfacial waves: Interface displacement.

5.4.3. Sloshing basin waves

5.4.3.1. 2D setup

In this test case the sloshing of an inviscid fluid with $\rho \equiv \rho_0 = 1025 \text{ kg m}^{-3}$ in a rectangular basin of length $L = 10 \text{ m}$ and of still water depth $H = 10 \text{ m}$ was simulated. The flow was driven by an initial surface elevation of constant slope ($x \in [0 \text{ m}, L]$):

$$\eta|_{t=0}(x) = \hat{\eta} \left(2 \frac{x}{L} - 1 \right). \quad (5.11)$$

Instead of initiating only one mode (see e.g. Gaarhuis, 1995), an infinite number of modes was set up due to this initial condition. Fourier analysis in terms of standing modes with wavenumber

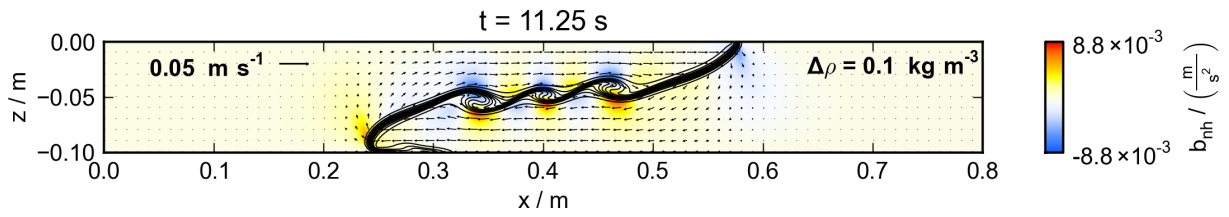
$$k_l = \frac{2\pi}{2L} l, \quad l \in \mathbb{N}_0 \quad (5.12)$$

and with the dispersion relation

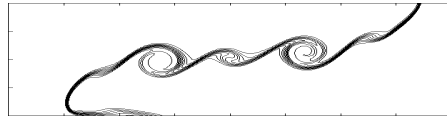
$$\omega(k) = \sqrt{gk \tanh(kH)} \quad (5.13)$$

yields the analytic solution for the surface elevation of the linearised problem,

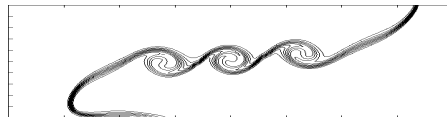
$$\eta(x, t) = \sum_{l=1,3,\dots} \eta_l(x, t), \quad (5.14)$$



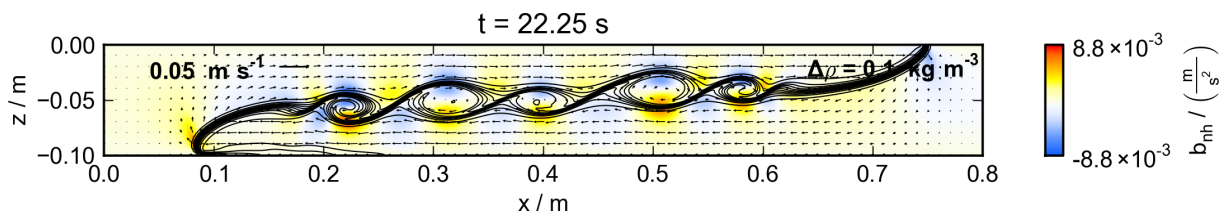
(a1) nonhydrostatic GETM



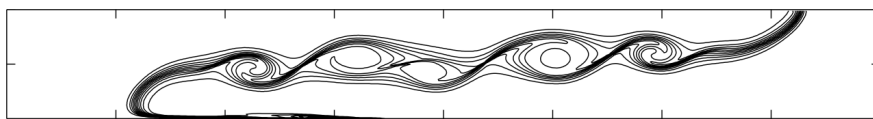
(a2) MITgcm: figure 1(a) from Berntsen et al. (2006)



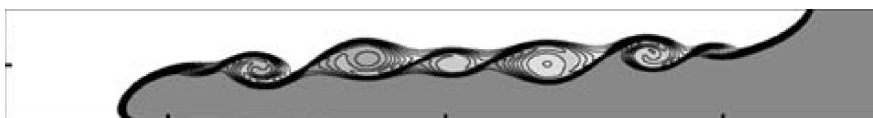
(a3) nonhydrostatic BOM: figure 1(b) from Berntsen et al. (2006)



(b1) nonhydrostatic GETM



(b2) SUNTANS: figure 11(b) from Fringer et al. (2006)



(b3) nonhydrostatic POM: figure 7 from Kanarska and Maderich (2003)

Figure 5.3.: Lock-exchange: Snapshots from nonhydrostatic simulations with GETM and other ocean models. The GETM results include isopycnals (black lines with $\Delta\rho = 0.1 \text{ kg m}^{-3}$), the nonhydrostatic buoyancy correction b_{nh} (coloured) and the velocity (arrows).

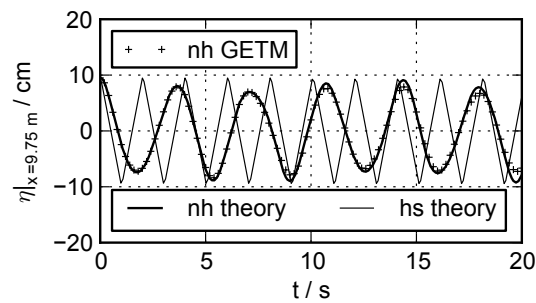


Figure 5.4.: 2D Sloshing basin waves: Evolution of surface elevation.

with

$$\eta_l(x, t) = -\frac{8\hat{\eta}}{(k_l L)^2} \cos(k_l x) \cos(\omega(k_l) t). \quad (5.15)$$

For $\hat{\eta} = 0.1$ m linear theory is valid (Ursell, 1953) and the superposition of the first 10 modes¹ is shown for the (nonhydrostatic) dispersion relation (5.13) and for its hydrostatic limit $\omega = \sqrt{gH}k$ in Figure 5.4. The great deviations between both analytical solutions already indicate the invalidity of the hydrostatic pressure assumption for this test case.

The analytical nonhydrostatic pressure contribution can be derived as

$$p_{\text{nh}}(x, z, t) = \rho_0 g \sum_{l=1,3,\dots} \eta_l(x, t) \left(\frac{\cosh(k_l(z+h))}{\cosh(k_l H)} - 1 \right). \quad (5.16)$$

Although consistency to the analytical solution requires the setup of an initial nonhydrostatic pressure contribution, the simulation was initialised only by the linearly inclined surface (5.11) with $\hat{\eta} = 0.1$ m. (Nonlinear) computations were carried out on a mesh with $\Delta x = 0.5$ m and 20 uniformly distributed σ -layers. For stability a filter weight of $\theta = 0.1\%$ was necessary. In order to compensate for the dissipation caused by this small filter weight, a time step of $\Delta t_{2D} = \Delta t_{3D} = 1 \times 10^{-5}$ s was chosen. Without additional iteration the temporal resolution of nonhydrostatic effects $\Delta t_{\text{nh}} \approx 4.6 \times 10^{-2}$ s was similar to time steps used in other publications. For these settings 24% of the total runtime were caused by the additional nonhydrostatic computations.

As shown in Figure 5.4 the simulated surface elevation agrees well with the nonhydrostatic analytical solution and the results of Casulli and Stelling (1998); Casulli (1999); Casulli and Zanolli (2002) and Kanarska et al. (2007). Despite slight deviations from the analytical solution in terms of amplitude, the simulated surface elevation proves its consistent coupling to the nonhydrostatic pressure contribution via the interaction terms (5.7).

¹Since the Fourier coefficients for the triangle-function rapidly tend to zero for higher-order modes, this number of modes is sufficient to represent the analytical solution.

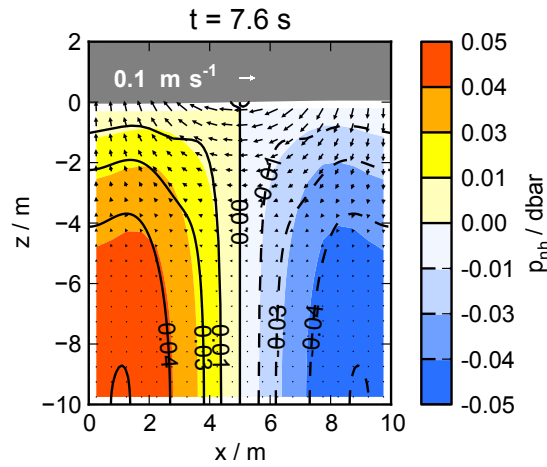


Figure 5.5.: 2D Sloshing basin waves: Snapshot after $t = 7.6$ s. The graphic shows the results from the nonhydrostatic GETM simulation including the nonhydrostatic pressure contribution (coloured) and the velocity (arrows). The analytical nonhydrostatic pressure contribution is added by contour lines.

Contrary to hydrostatic theory and simulation (not shown), the sloshing affected only the upper part of the basin. Phases of maximum nonhydrostatic pressure contribution near each wall were induced during periods of minimum surface elevation by decreasing downward velocity and subsequent increasing upward velocity. Figure 5.5 juxtaposes the analytical (by means of (5.16)) and the simulated nonhydrostatic pressure contribution.

The existence of an analytical solution offers a convergence analysis. Since the spatial discretisation of (5.9) coincides with that of tracers and therefore does not change the spatial convergence behaviour of the model, only the temporal convergence is analysed here. In Table 5.1 the RMS-error ϵ_{rms} is shown depending on both the time step Δt_{3D} and the number of iterations N_{it} . For several combinations a similar temporal resolution of nonhydrostatic effects is obtained and the corresponding errors are almost identical. Although a decreased time step slightly decreases the error more than an increased number of iterations does, the results show that the increase of the number of iterations has the same effect as a decrease of the model time step. As already mentioned at the end of Section 5.3.4, the former is preferable because the computational effort of the iteration cycle is only a fraction of that of a whole model time step. Figure 5.6 indicates a first-order truncation error.

N_{it}	1		2		4	
$\Delta t_{3D} / s$	$\Delta t_{nh} / s$	ϵ_{rms} / m	$\Delta t_{nh} / s$	ϵ_{rms} / m	$\Delta t_{nh} / s$	ϵ_{rms} / m
2.000e-4	—	—	4.604e-1	3.972e-2	2.302e-1	2.674e-2
1.000e-4	4.603e-1	3.970e-2	2.302e-1	2.671e-2	1.151e-1	1.547e-2
5.000e-5	2.301e-1	2.670e-2	1.151e-1	1.545e-2	5.755e-2	8.259e-3
2.000e-5	9.206e-2	1.266e-2	4.604e-2	6.790e-3	2.302e-2	4.478e-3
1.000e-5	4.603e-2	6.786e-3	2.302e-2	4.476e-3	—	—
5.000e-6	2.302e-2	4.475e-3	—	—	—	—

Table 5.1.: 2D Sloshing basin waves: Convergence analysis for $\eta|_{t=20s}$ with $\theta = 0.1\%$.

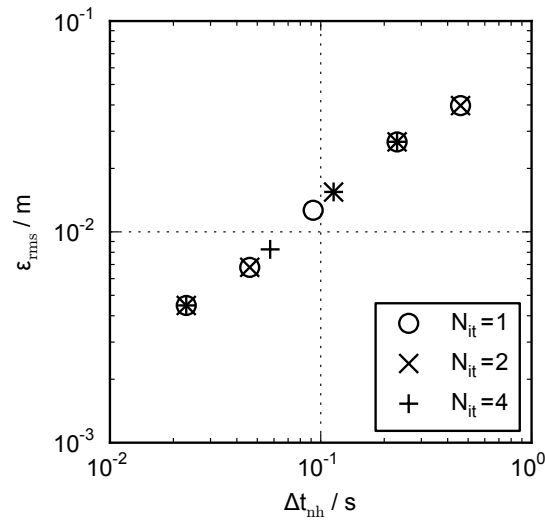


Figure 5.6.: 2D Sloshing basin waves: Graphical representation of Table 5.1.

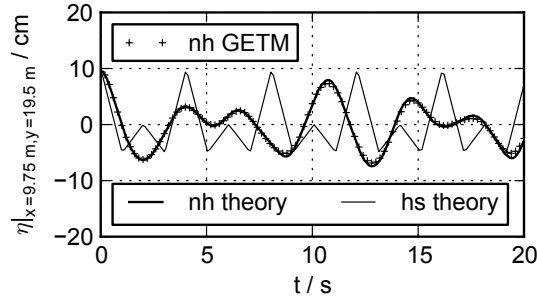


Figure 5.7.: 3D Sloshing basin waves

5.4.3.2. 3D setup

To test the feasibility of the alternative approach in 3D applications, the basin was extended along a width of $W = 20$ m. The initial surface elevation was given by $(x \in [0 \text{ m}, L], y \in [0 \text{ m}, W])$:

$$\eta|_{t=0}(x, y) = \hat{\eta} \left(\frac{x}{L} + \frac{y}{W} - 1 \right). \quad (5.17)$$

With the additional meridional wavenumber

$$m_n = \frac{2\pi}{2W} n, \quad n \in \mathbb{N}_0, \quad (5.18)$$

an analytical solution for the surface elevation of the linearised problem can be obtained:

$$\begin{aligned} \eta(x, y, t) = & -\hat{\eta} \left[\sum_{l=1,3,\dots} \frac{4}{(k_l L)^2} \cos(k_l x) \cos(\omega(k_l) t) \right. \\ & \left. + \sum_{n=1,3,\dots} \frac{4}{(m_n W)^2} \cos(m_n y) \cos(\omega(m_n) t) \right]. \end{aligned} \quad (5.19)$$

In Figure 5.7 this analytical solution is presented for the full (nonhydrostatic) and the hydrostatic dispersion relation. The great deviations show again the invalidity of the hydrostatic pressure assumption for this test case. With $\Delta y = 1$ m and all other parameters adopted from the 2D setup numerical results of the extended GETM were obtained that reproduce well the amplitude and phase of the analytical solution (Figure 5.7). For this 3D setup 19% of the total runtime were caused by the additional nonhydrostatic computations.

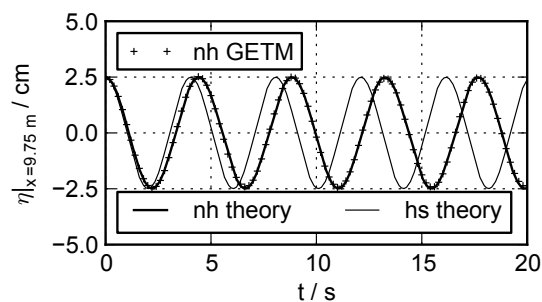


Figure 5.8.: A moderately nonhydrostatic standing wave

5.4.3.3. A moderately nonhydrostatic standing wave

The 2D setup described in Section 5.4.3.1 was modified to test the extended GETM in a less strong nonhydrostatic regime. Therefore the still water depth, the amplitude of the initial surface elevation and the number of vertical layers were reduced by a factor of 4 to $H = 2.5$ m, $\hat{\eta} = 0.025$ m and 5 uniformly distributed σ -layers. Furthermore, only the first mode with wavenumber k_1 according to (5.12) was initialised ($x \in [0 \text{ m}, L]$):

$$\eta|_{t=0}(x) = -\hat{\eta} \cos(k_1 x).$$

Based on the full dispersion relation (5.13) the period of this mode is given by $T_{\text{nh}} \approx 4.4$ s. Under the hydrostatic pressure assumption the period of this mode is underpredicted by nearly 10% ($T_{\text{hs}} \approx 4.0$ s), causing both solutions being out of phase after $t = 20$ s.

Compared to the setup described in 5.4.3.1, for this less strong nonhydrostatic regime ($k_1 H \approx 0.8$) the filter weight and the time step could be increased by two orders of magnitude to $\theta = 14\%$ and $\Delta t_{2D} = \Delta t_{3D} = 1 \times 10^{-3}$ s. Without additional iteration the temporal resolution of nonhydrostatic effects was $\Delta t_{\text{nh}} \approx 3.1 \times 10^{-2}$ s and only 17% of the total runtime were caused by the additional nonhydrostatic computations. As shown in Figure 5.8, the simulated surface elevation matches the correct analytical one in perfect agreement.

5.4.4. Tidally induced internal lee waves

Xing and Davies (2006) showed that a nonhydrostatic 2DV slice model with vanishing across-slice gradients can reproduce the major processes contributing to internal mixing in sill regions. The significance of nonhydrostatic dynamics and the necessity of their sufficient resolution were demonstrated by Xing and Davies (2007) and Berntsen et al. (2009).

The topography, frictional parameters and initial conditions were specified according to Berntsen et al. (2009). The domain of interest $-1500 \text{ m} \leq x \leq 2000 \text{ m}$ was discretised by $\Delta x = 10$ m. At the western end it was bounded by an open boundary cell, where the temperature was held fixed at its initial value. In the east a layer of 49 cells with Δx continuously stretched by a factor of 1.2 was added. The most eastern cell represented an open boundary with a vanishing lateral temperature

gradient. At the open boundaries barotropic forcing with a maximum transport of $\hat{Q} = 11.5 \text{ m}^2\text{s}^{-1}$ and with frequency ω given by the M_2 -tide was applied:

$$\int_{-H}^{\eta} u dz \equiv \hat{Q} \sin(\omega t). \quad (5.20)$$

In the vertical the domain was discretised by 100 uniformly distributed σ -layers.

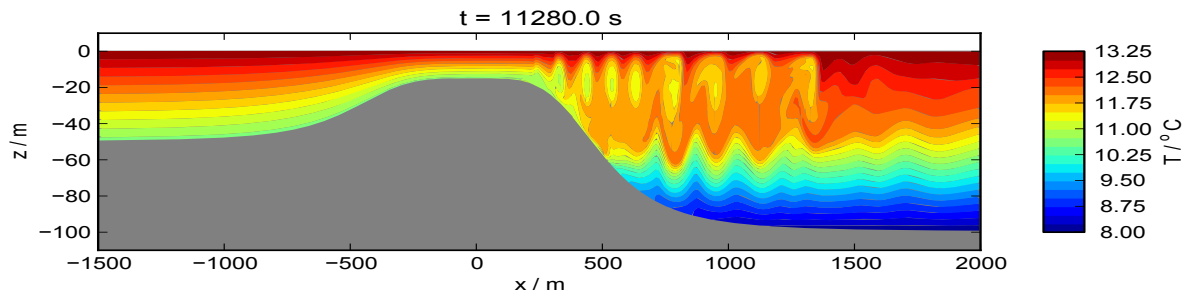
The simulation was carried out for half a tidal cycle with a time step of $\Delta t_{2D} = \Delta t_{3D} = 0.3 \text{ s}$ constrained by the barotropic CFL-criterion and similar to the time step used by Berntsen et al. (2008, 2009) ($\Delta t_{3D} = 0.56 \text{ s} = 30\Delta t_{2D}$). A filter weight of $\theta = 1\%$ and $N_{\text{it}} = 2$ iterations implied a temporal resolution of nonhydrostatic effects of $\Delta t_{\text{nh}} \approx 69 \text{ s}$. For these settings 33% of the total runtime were caused by the additional nonhydrostatic computations.

The beginning barotropic tide caused an upwelling of the isotherms in front of the sill and a downwelling of the isotherms behind the sill. The fluid at the shallow sill was accelerated faster than in the deep downstream basin. The hydraulic transition between the resulting supercritical conditions near the sill and the subcritical conditions in the downstream basin formed an internal bore. This was amplified when the first cold water masses from near the bottom of the upstream basin were flowing over the sill into the resting deeper downstream basin. Flow separation near the sill top caused convective overturning with warm fluid lifted up, thereby setting up an oscillation of the isotherms above, and enclosed by recirculating colder fluid. The recirculating eddy was advected away from the sill top and due to shear the enclosed fluid was mixed with the ambient fluid and formed a well mixed part of the water column. The downward oscillating isotherms in its back finally created an isolated patch that was further advected downstream with the propagating waves. These generation processes at the downstream side of the sill continued until flow reversal. The waves propagating through the the downstream basin were associated with shear and overturning (see Figure 5.9) and caused the upper part of the downstream basin to become nearly well mixed.

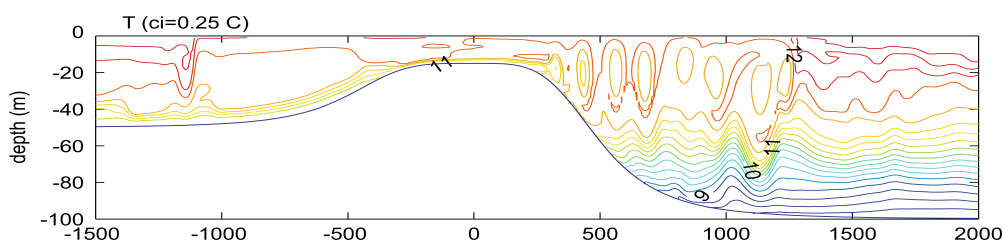
As shown in Figure 5.9, these findings are consistent with similar studies carried out with other nonhydrostatic ocean models (e.g. by Davies and Xing, 2007). Despite the use of GETM with its σ -coordinates and the associated different discretisation of advection and diffusion processes especially above the lee flank of the sill, the amplitude, wave length and celerity of the generated internal waves agree well with the simulation results of the MITgcm with z -coordinates. In this context, it is also interesting to view this agreement in the light of the effect of coinciding values of “horizontal” viscosity, since Berntsen et al. (2008) showed a rather strong sensitivity to “horizontal” viscosity (see their Figs. 7d and 15a,b).

Deviations from this general consistency can be caused not only by the alternative nonhydrostatic solver, but also by the missing tidal spin-up period and the missing associated modification of the initial stratification. Within the domain of interest the different treatment of the lateral boundaries will have an effect on the simulation results as well.

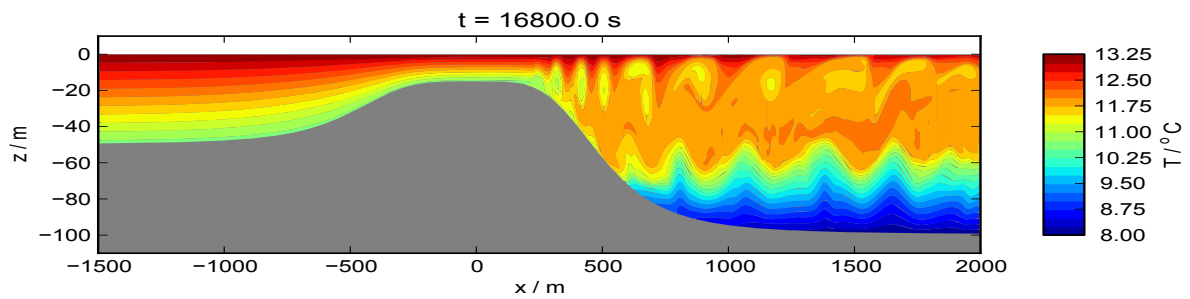
In the hydrostatic simulation (not shown) flow separation also generated well mixed patches that were advected away from the sill top. However, due to the missing nonhydrostatic effects nonlinear steepening occurred and larger vertical velocities caused enhanced mixing of these patches. The thereby weakened stratification altered the propagation of the waves and caused the patches to overroll. Due to the resulting stronger shear and convective overturning the upper part of the downstream basin was mixed much faster than in the nonhydrostatic simulation.



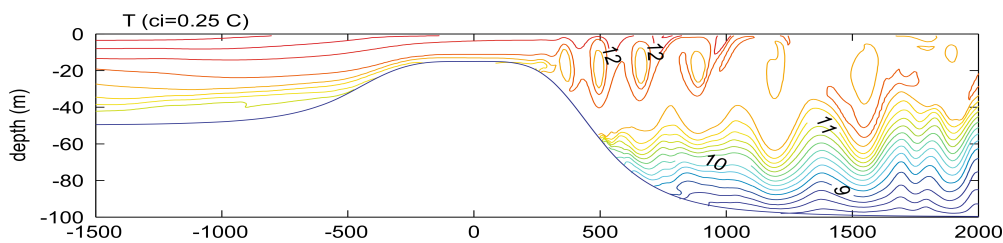
(a1) nonhydrostatic GETM



(a2) MITgcm: from figure 2b of Davies and Xing (2007)



(b1) nonhydrostatic GETM



(b2) MITgcm: from figure 2c(i) of Davies and Xing (2007)

Figure 5.9.: Tidally induced internal lee waves: Snapshots from nonhydrostatic simulations with GETM and MITgcm. The results show the temperature distribution after $2/8$ [$10/8$ for MITgcm] (a) and $3/8$ [$11/8$ for MITgcm] (b) of the tidal cycle.

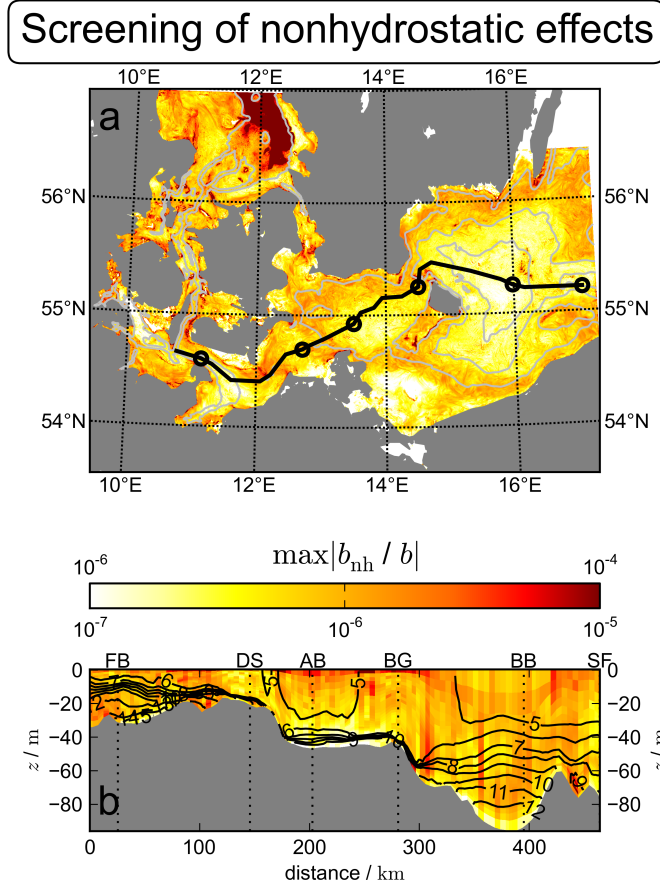


Figure 5.10.: Analysis of a realistic Western Baltic Sea model: Screening of nonhydrostatic effects. Based on hourly data the maximum screening parameter within the period 19-28 Sep 2008 is shown for the whole water column (a) and along a transect (b). The ticks above the colorbar refer to a, the ticks below to b. In a isobaths with an interval of 25 m are depicted by grey contour lines and the black line with markers locates the transect with important stations presented in b. The stations are Fehmarn Belt (FB), Darss Sill (DS), Arkona Basin (AB), Bornholmsgat (BG), Bornholm Basin (BB) and Słupsk Furrow (SF). Contour lines in b depict mean isopycnals.

5.4.5. Analysis of a realistic Western Baltic Sea model

The implemented alternative approach also offers a screening mode to estimate the importance of nonhydrostatic effects. In this mode the nonhydrostatic buoyancy b_{nh} is calculated, but not further incorporated into the dynamic equations. As derived in (2.14), the ratio of dynamic relevant pressure contributions can be equivalently calculated as the ratio $\frac{b_{nh}}{b}$. Therefore, this ratio defines a reasonable local screening parameter for nonhydrostatic effects (also see Wadzuk, 2004; Tseng et al., 2005).

For the realistic setup of the Western Baltic Sea described in Section 4.3.3 the importance of nonhydrostatic effects were estimated. The computational overhead was marginal (2%). For large parts of the model domain $\mathcal{O}\left\{\frac{b_{nh}}{b}\right\} \ll 1$ (see Figure 5.10) indicates the validity of the applied hydrostatic pressure assumption. Marginally increased, but still insignificant ratios can be identified in the vicinity of topographic features. Significant ratios of $\mathcal{O}\left\{\frac{b_{nh}}{b}\right\} = 1$ were diagnosed only in the deep part of the Kattegat (Figure 5.10a). These significant ratios were localised in the near bottom layers (not shown). In the Kattegat a complex circulation affected by tides and the near-surface outflow of the

Baltic Sea was present. However, the Kattegat is too close to the open boundaries to study this circulation in detail. Therefore, the origin of the strong induced nonhydrostatic pressure contributions in the deep Kattegat cannot be analysed with the present setup.

As described in Section 4.3.3, in a future project the analysed Western Baltic Sea model should be utilised to investigate near-inertial waves in the Bornholm Basin. Within the present lateral resolution of approximately 600 m no significant nonhydrostatic effects were diagnosed in the Bornholm Basin. However, already at the end of Section 4.3.3 the necessity of higher-resolution nestings to sufficiently resolve near-inertial wave dynamics in Bornholm Basin was concluded. Within these higher-resolution nestings so far unresolved nonhydrostatic dynamics can become important and the validity of the hydrostatic pressure assumption has to be verified again.

5.5. Discussion

The test cases demonstrate the nonhydrostatic capability of the extended GETM including applications in 3D, with a free surface and with variable topography. However, the straight-forward inclusion of nonhydrostatic dynamics strongly affected the stability of the simulations. The origin of the instabilities was the decoupling of the incompressibility constraint and the balance of momentum. Especially the explicit calculation of b_{nh} according to (5.9) was prone to instabilities. Fluctuations affected the first term $\Delta t_{3D}^{-1} \left[h_k^{(n+1/2)} w_k^{(n+1/2)} - h_k^{(n-1/2)} w_k^{(n-1/2)} \right]$ and due to the decoupled treatment the second term $ADV \left(w_k^{(n+1/2)} \right)$ could not balance this. The coupling and the convergence could be improved by an iteration. Furthermore, considering the sensitive response behaviour of the overall procedure, a cumulative temporal filter was appropriate to suppress instabilities. Its effect on the temporal resolution of nonhydrostatic effects could be estimated (Appendix C). For one test case (Section 5.4.3.1) the temporal convergence was analysed.

For the rather demanding benchmark test cases (Sections 5.4.1, 5.4.2, 5.4.3.1 and 5.4.3.2) a small filter weight was necessary for stability. A sufficient resolution of nonhydrostatic effects in turn required either a small time step or a high number of iterations and thus strongly hampered the efficiency.

For simulations without direct nonhydrostatic feedback to the layer heights, either due to a rigid-lid, or via the free surface elevation due to interaction terms (5.7) with b_{nh} being neglected (“hydrostatic free surface”; not shown), the first term on the right-hand side of (5.9) was more stable. Of course, for the correct simulation of surface waves the coupling of the free surface to the nonhydrostatic pressure contribution via the interaction terms including b_{nh} was essential (Section 5.4.3). In contrast, propagating internal waves were only marginally affected by a “hydrostatic free surface” or a rigid-lid (not shown).

The variable topography of the test case in Section 5.4.4 represents another source of errors. In sloping σ -layers the calculation of the horizontal pressure gradient force can be prone to truncation errors. However, although included according to (5.2), errors in b_{nh} are not expected to be substantially amplified because of a high spatial resolution and the accurate internal pressure scheme of Shchepetkin and McWilliams (2003) used in this test case.

The test case in Section 5.4.3.3 represents a less strong nonhydrostatic regime. Although the stability problems did not disappear, they could be handled by a moderate filter weight and thus a practical time step and a low nonhydrostatic overhead. These findings indicate an increasing efficiency of the straight-forward inclusion of nonhydrostatic dynamics in the transition to weak nonhydrostatic regimes.

Although not relevant for the presented test cases, an additional source of fluctuations can be given by the diagnostic adjustment of the vertical velocity according to (2.19). In nearly geostrophic flows the

vertical velocity calculated by means of (2.19) can contain numerical errors amplified by the inverse Rossby number (Browning et al., 1990).

The last test case presented in Section 5.4.5 demonstrated the utilisation of the extended GETM in screening mode to estimate the importance of nonhydrostatic effects in a realistic application to the Western Baltic Sea. In large parts of the model domain the diagnosed screening parameter indicated insignificant nonhydrostatic effects, which was reasonable for the used lateral resolution.

5.6. Conclusions

In this study the straight-forward inclusion of the missing nonhydrostatic pressure contribution into an existing hydrostatic model kernel was tested. Based on an explicit vertical integration of the additional nonhydrostatic terms within the balance of vertical momentum, this approach circumvents the classical Poisson equation for the nonhydrostatic pressure contribution. Its easy implementation into an explicit mode-splitting model kernel was outlined by means of the extension of the General Estuarine Transport Model (GETM).

The nonhydrostatic capability of the extended GETM was verified by several nonhydrostatic benchmark test cases. The results validate the feasibility to simulate even strongly nonhydrostatic regimes. However, stability issues hampered the efficiency and therefore limit the practical applicability.

These stability issues were caused by the decoupled treatment of the governing equations. In the transition to weakly nonhydrostatic flows the effect of this decoupling on stability and convergence was reduced. Less critical stability constraints offered larger time steps and better convergence behaviour significantly decreased the number of iterations necessary to force convergence.

Due to its limited practical applicability the straight-forward inclusion of nonhydrostatic dynamics cannot replace the pressure correcting projection method. However, it represents an easy to implement option for traditional hydrostatic ocean models to relax the hydrostatic pressure assumption in the limit of weak nonhydrostatic processes.

As future development the efficiency could be increased by the implementation of convergence criteria for the applied iteration and of an adaptive switch strategy between hydrostatic and nonhydrostatic computations to restrict the latter ones only to regions where nonhydrostatic effects are really important. For both the local screening parameter defined in Section 5.4.5 can be utilised.

Chapter 6.

Inclusion of wind wave effects

In Section 2.3 the importance of unresolved motions for the resolved mean flow was emphasised. In this context, wind-generated surface gravity waves (*wind waves*) have to be mentioned as well. Although wind waves already occur on much larger scales than turbulence (Mellor, 2003; Holthuijsen, 2007), within the resolution of practical coastal ocean modelling applications wind waves are still usually not resolved. But they can affect the mean flow in different ways: wave-enhanced surface and bottom stresses (Michaud et al., 2012), wave-enhanced turbulence (Craig and Banner, 1994; Burchard, 2001), wave-induced Stokes-drift (Longuet-Higgins, 1953) and wave-induced mean sealevel changes over sloping bottoms (“wave set-up”; Longuet-Higgins and Stewart, 1964). These effects on the mean flow should be considered by additional forcing terms. These terms depend on wave properties that can be provided by a wind wave model coupled to the ocean model.

In this Chapter necessary modifications to a hydrostatic coastal ocean model are outlined to include the 3D effects of unresolved wind waves.

6.1. Introduction

In the context of wind waves the mean flow represents a wave-averaged flow. For the wave-averaged depth-integrated Navier-Stokes Equations the additional forcing can be derived as a net wave-induced momentum flux, represented by the divergence of a 2D Radiation Stress tensor (Longuet-Higgins and Stewart, 1964).

Mellor (2003) extended this concept to a depth-dependent Radiation Stress tensor and presented a closed set of equations for the description of 3D wave-current interaction. However, due to a mistake in the transformation of the horizontal pressure gradient to σ -coordinates, the Radiation Stress tensor derived by Mellor (2003) was wrong. Mellor (2008) derived another depth-dependent Radiation Stress tensor including a singular surface term. This term was necessary for the consistency with the depth-integrated Radiation Stress tensor of Longuet-Higgins and Stewart (1964), but it originates in an inconsistent treatment of the pressure (Bennis and Ardhuin, 2011). Furthermore, within the momentum equations of Mellor (2008) the horizontal derivatives of the elements of the Radiation Stress tensor were taken in z -coordinates, resulting in depth-integrated equations inconsistent with Phillips (1977). Finally, based on the correct transformation of the horizontal pressure gradient in the equations of Mellor (2003) and with the Radiation Stress tensor of Mellor (2008), Mellor (2011a) presented a closed set of equations in σ -coordinates consistent with Longuet-Higgins and Stewart (1964) and Phillips (1977). Kumar et al. (2011) implemented the Radiation Stress formulation of Mellor (2011a) into the Regional Ocean Modeling System (ROMS; Shchepetkin and McWilliams, 2005) and confirmed that the equations captured the dynamics in the surfzone. However, they also stressed the occurrence of spurious flows in shoaling regions and due to the singular surface term in the Radiation Stress tensor.

A general framework for the derivation of 3D wave-averaged equations is provided by the Generalised Lagrangian Mean (GLM) theory of Andrews and McIntyre (1978a). Within the GLM theory a Lagrangian average (obtained along a Lagrangian trajectory) is referenced to the corresponding averaged position to provide a description within a Eulerian framework. The difference between the Lagrangian and Eulerian average (with the latter taken at a fixed position) defines the corresponding Stokes correction. Andrews and McIntyre (1978a) derived two equivalent sets of exact prognostic equations for both the Lagrangian and the quasi-Eulerian wave-averaged velocity ($\bar{\mathbf{u}}^L$ and $\bar{\mathbf{u}}^{qE}$ respectively). The latter was named by Jenkins (1989) and is defined as the difference between the Lagrangian wave-averaged velocity and the (specific) pseudomomentum of the waves (Andrews and McIntyre, 1978b). To lowest order the pseudomomentum of the waves differs from the Stokes drift $\bar{\mathbf{u}}^{\text{Stokes}} = \bar{\mathbf{u}}^L - \bar{\mathbf{u}}^E$ only by the vertical shear of the Eulerian wave-averaged velocity $\bar{\mathbf{u}}^E$ (Ardhuin et al., 2008).

As outlined by Andrews and McIntyre (1978a), the GLM equations for the Lagrangian wave-averaged velocity are forced by the divergence of a tensor that can indeed be identified with a depth-dependent Radiation Stress tensor under certain conditions. On the other hand, based on the GLM equations for the quasi-Eulerian wave-averaged velocity Leibovich (1980) could rederive the equations of Craik and Leibovich (1976) containing the Vortex Force $\bar{\mathbf{u}}^{\text{Stokes}} \times (\nabla \times \bar{\mathbf{u}}^E)$ for the description of Langmuir circulations. In this context the Radiation Stress and Vortex Force concepts seem to be formally equivalent. However, for practical use the different forcing terms within each set of GLM equations must be consistently closed up to a given order (Ardhuin et al., 2008). As argued by Ardhuin et al. (2008) and Bennis et al. (2011), a consistent closure of the GLM equations for the Lagrangian wave-averaged velocity is rather impractical. Furthermore, Lane et al. (2007) showed that the lowest-order Radiation Stress equations are asymptotically inconsistent, because they do not capture all dynamics of the corresponding Vortex Force equations.

Based on the GLM equations for the quasi-Eulerian wave-averaged velocity, Ardhuin et al. (2008) derived a closed set of equations that is consistent with the one of McWilliams et al. (2004) derived earlier by multiple asymptotic scale analysis. The latter was validated within ROMS by Uchiyama et al. (2010). Recently, Michaud et al. (2012) validated the formulation of Ardhuin et al. (2008) within the ocean model SYMPHONIE (Marsaleix et al., 2008). They also showed, that for weak vertical shear the simplified forcing proposed by Bennis et al. (2011) is sufficient.

6.2. Modified governing equations

The inclusion of wind wave effects into a coastal ocean model requires the modification of its governing equations. In this Section the modification is demonstrated by means of the hydrostatic layer-integrated equations of GETM (3.2a)–(3.2c). As mentioned in the introduction, two different formulations of the wave-averaged equations are possible. Therefore, the prognostic velocities $u_{\alpha,k}$ and the additional forcing terms $F_{\alpha,k}^{\text{wave}}$ in the following layer-integrated equations depend on the choice of formulation:

$$0 = \frac{\partial h_k}{\partial t} + \frac{\partial}{\partial x} \{h_k \bar{u}_k^L\} + \frac{\partial}{\partial y} \{h_k \bar{v}_k^L\} + \left(w_{k+1/2}^s - w_{k-1/2}^s\right), \quad (6.1a)$$

$$\begin{aligned} & \frac{\partial}{\partial t} \{h_k u_k\} + \frac{\partial}{\partial x} \{h_k \bar{u}_k^L u_k\} + \frac{\partial}{\partial y} \{h_k \bar{v}_k^L u_k\} + \left(w_{k+1/2}^s u_{k+1/2} - w_{k-1/2}^s u_{k-1/2}\right) - f_v h_k \bar{v}_k^L \\ &= -h_k \frac{\partial}{\partial x} \left\{ \frac{p|_{z=\eta}}{\rho_0} \right\} - h_k g \frac{\partial \eta}{\partial x} + (\tau_{x,k+1/2}(\bar{u}^{\text{qE}}, \bar{v}^{\text{qE}}) - \tau_{x,k-1/2}(\bar{u}^{\text{qE}}, \bar{v}^{\text{qE}})) + h_k \tilde{F}_x^{\text{h}}(\bar{u}_k^{\text{qE}}, \bar{v}_k^{\text{qE}}, h_k) \\ & \quad + h_k F_{x,k}^{\text{IP}}(b) + h_k F_{x,k}^{\text{wave}}, \end{aligned} \quad (6.1b)$$

$$\begin{aligned} & \frac{\partial}{\partial t} \{h_k v_k\} + \frac{\partial}{\partial x} \{h_k \bar{u}_k^L v_k\} + \frac{\partial}{\partial y} \{h_k \bar{v}_k^L v_k\} + \left(w_{k+1/2}^s v_{k+1/2} - w_{k-1/2}^s v_{k-1/2}\right) + f_v h_k \bar{u}_k^L \\ &= -h_k \frac{\partial}{\partial y} \left\{ \frac{p|_{z=\eta}}{\rho_0} \right\} - h_k g \frac{\partial \eta}{\partial y} + (\tau_{y,k+1/2}(\bar{u}^{\text{qE}}, \bar{v}^{\text{qE}}) - \tau_{y,k-1/2}(\bar{u}^{\text{qE}}, \bar{v}^{\text{qE}})) + h_k \tilde{F}_y^{\text{h}}(\bar{u}_k^{\text{qE}}, \bar{v}_k^{\text{qE}}, h_k) \\ & \quad + h_k F_{y,k}^{\text{IP}}(b) + h_k F_{y,k}^{\text{wave}}. \end{aligned} \quad (6.1c)$$

In (6.1a)–(6.1c) the *advecting* mass transport velocities are always given by the Lagrangian wave-averaged velocities $\bar{u}_{\alpha,k}^L$. In contrast, as argued by Ardhuin et al. (2008), viscous and turbulent stresses are always calculated in terms of the quasi-Eulerian wave-averaged velocities $\bar{u}_{\alpha,k}^{\text{qE}}$. Below the troughs the quasi-Eulerian wave-averaged velocities differ from the Eulerian wave-averaged velocities to lowest order only due to the vertical shear of the Eulerian wave-averaged velocity (Ardhuin et al., 2008). Thus, for weak vertical shear of the Eulerian wave-averaged velocity (as assumed by Bennis et al. (2011) and in the following), the Eulerian wave-averaged velocities can be identified with the quasi-Eulerian wave-averaged velocities. Therefore, the Lagrangian and quasi-Eulerian wave-averaged velocities can be related to each other by the Stokes drift according to:

$$\bar{u}_k^L - \bar{u}_k^{\text{qE}} \approx \bar{u}_k^L - \bar{u}_k^{\text{E}} = \bar{u}_k^{\text{Stokes}}, \quad (6.2a)$$

$$\bar{v}_k^L - \bar{v}_k^{\text{qE}} \approx \bar{v}_k^L - \bar{v}_k^{\text{E}} = \bar{v}_k^{\text{Stokes}}. \quad (6.2b)$$

For a monochromatic wave the Stokes drift is given by (see e.g. Kumar et al., 2012):

$$\bar{u}_k^{\text{Stokes}} \approx 2 \frac{k_x E}{c} \frac{\cosh(2 \|\mathbf{k}\| (z_k + H))}{\sinh(2 \|\mathbf{k}\| (\eta + H))}, \quad (6.3a)$$

$$\bar{v}_k^{\text{Stokes}} \approx 2 \frac{k_y E}{c} \frac{\cosh(2 \|\mathbf{k}\| (z_k + H))}{\sinh(2 \|\mathbf{k}\| (\eta + H))}, \quad (6.3b)$$

with $E = \frac{1}{16}gH_s^2$, $c = \frac{\lambda}{T}$, $\|\mathbf{k}\| = \frac{2\pi}{\lambda}$ and $(k_x, k_y) = \|\mathbf{k}\| (\cos \bar{\theta}, \sin \bar{\theta})$ being the (specific) wave-averaged wave energy, the wave celerity, the wave number and its corresponding directional components, respectively. Mean wave properties like significant wave height H_s , wave length λ , intrinsic wave period T and wave direction $\bar{\theta}$ are provided by the wave model.

6.2.1. Details of the Radiation Stress formulation

Within the Radiation Stress formulation of Mellor (2011a) the prognostic velocities can be interpreted as Lagrangian wave-averaged velocities $u_{\alpha,k} \equiv \bar{u}_{\alpha,k}^L$, related to Eulerian wave-averaged velocities within a wave-following vertical coordinate (Mellor, 2003). The forcing term is obtained as the divergence of a depth-dependent Radiation Stress tensor (Mellor, 2008, 2011b),

$$F_{\alpha,k}^{\text{wave}} = -\frac{1}{h_k} \frac{\partial}{\partial x_\beta} \left\{ h_k \|\mathbf{k}\| E \left[(f^{\text{cc}} f^{\text{cs}})_k \frac{k_\alpha k_\beta}{\|\mathbf{k}\|^2} - \delta_{\alpha\beta} \left((f^{\text{ss}} f^{\text{sc}})_k - \frac{f_k^{\text{RS}} (\eta - z_k)}{2 \|\mathbf{k}\| h_k} \right) \right] \right\}, \quad (6.4)$$

with

$$(f^{\text{cc}} f^{\text{cs}})_k = \frac{1}{h_k} \int_{z_{k-1/2}}^{z_{k+1/2}} f^{\text{cc}}(z+H) f^{\text{cs}}(z+H) dz, \quad (6.5a)$$

$$(f^{\text{ss}} f^{\text{sc}})_k = \frac{1}{h_k} \int_{z_{k-1/2}}^{z_{k+1/2}} f^{\text{ss}}(z+H) f^{\text{sc}}(z+H) dz, \quad (6.5b)$$

and

$$f^{\text{cc}}(\zeta) = \frac{\cosh(\|\mathbf{k}\| \zeta)}{\cosh(\|\mathbf{k}\| (\eta + H))}, \quad (6.6a)$$

$$f^{\text{cs}}(\zeta) = \frac{\cosh(\|\mathbf{k}\| \zeta)}{\sinh(\|\mathbf{k}\| (\eta + H))}, \quad (6.6b)$$

$$f^{\text{ss}}(\zeta) = \frac{\sinh(\|\mathbf{k}\| \zeta)}{\sinh(\|\mathbf{k}\| (\eta + H))}, \quad (6.6c)$$

$$f^{\text{sc}}(\zeta) = \frac{\sinh(\|\mathbf{k}\| \zeta)}{\cosh(\|\mathbf{k}\| (\eta + H))}. \quad (6.6d)$$

The function $f_k^{\text{RS}}(\zeta)$ appearing in the last term of (6.4) is still subject to discussion. Mellor (2008) originally proposed $f_k^{\text{RS}} = \delta_{k,k_{\text{max}}}$. In contrast, Kumar et al. (2011) applied a smooth distribution in the vertical to decrease spurious flow in shoaling regions.

6.2.2. Details of the Vortex Force formulation

The Vortex Force formulation of Arduin et al. (2008) is based on the GLM equations for the quasi-Eulerian wave-averaged velocities $u_{\alpha,k} \equiv \bar{u}_{\alpha,k}^{\text{qE}}$. The Vortex Force does not appear explicitly, because its contributions are incorporated into the advection term and the dynamic pressure. For weak vertical shear of the Eulerian wave-averaged velocities, the forcing was simplified according to Bennis et al. (2011):

$$F_{\alpha,k}^{\text{wave}} = \bar{u}_{\beta,k}^{\text{Stokes}} \left(\frac{\partial \bar{u}_{\beta,k}^{\text{qE}}}{\partial x_{\alpha}} \right)_z - \left(\frac{\partial}{\partial x_{\alpha}} \right)_z \left\{ \frac{\|\mathbf{k}\| E}{\sinh(2\|\mathbf{k}\|(\eta + H))} \right\} + F_{\alpha,k}^{\text{ds}}. \quad (6.7)$$

The terms $F_{\alpha,k}^{\text{ds}}$ represent sources of momentum transferred from the waves due to dissipation by bottom friction $S^{\text{ds,b}}$, surface breaking $S^{\text{ds,br}}$ and white capping $S^{\text{ds,w}}$ (all these dissipation rates are provided by the wave model):

$$F_{\alpha,k}^{\text{ds}} = \frac{1}{h_k} \frac{k_{\alpha} g}{\|\mathbf{k}\| c} \left(f_k^{\text{ds,b}}(z_k + H) S^{\text{ds,b}} + f_k^{\text{ds,s}}(\eta - z_k) S^{\text{ds,s}} \right), \quad (6.8)$$

with

$$S^{\text{ds,s}} = S^{\text{ds,br}} + S^{\text{ds,w}}. \quad (6.9)$$

The functions $f_k^{\text{ds,b}}(\zeta)$ and $f_k^{\text{ds,s}}(\zeta)$ distribute the resulting forces in the vertical (Uchiyama et al., 2010).

6.2.3. Vertical distribution of wave-induced forcing

In (6.4) and (6.8) the empirical functions $f_k^{\text{RS}}(\zeta)$, $f_k^{\text{ds,b}}(\zeta)$ and $f_k^{\text{ds,s}}(\zeta)$ were formally introduced without a closed specification. Following the vertical distribution of the Stokes drift in (6.3a) and (6.3b), Uchiyama et al. (2010) and Kumar et al. (2011) suggested

$$f_k^X(\zeta) \propto \cosh \left(\frac{\eta + H - \zeta}{\mathcal{L}^X} \right), \quad (6.10)$$

with $X \in \{(\text{RS}), (\text{ds, b}), (\text{ds, s})\}$.

The corresponding length scales \mathcal{L}^X can be given in terms of the significant wave height H_s and the thickness of the wave-induced bottom boundary layer δ_w (see Uchiyama et al. (2010) for the definition of δ_w):

$$\mathcal{L}^{\text{RS}} = \alpha^{\text{RS}} H_s, \quad (6.11a)$$

$$\mathcal{L}^{\text{ds,b}} = \alpha^{\text{ds,b}} \delta_w, \quad (6.11b)$$

$$\mathcal{L}^{\text{ds,s}} = \alpha^{\text{ds,s}} H_s. \quad (6.11c)$$

The parameters α^X can be calibrated by a sensitivity analysis (see e.g. Moghimi et al., 2012).

6.2.4. Further modifications

To account for the wave-enhanced turbulence, the surface and bottom roughness lengths have to be modified and also $S^{\text{ds,s}}$ defined in (6.9) has to be provided to the turbulence model for the proper injection of turbulent kinetic energy due to breaking waves. More details can be found in Moghimi et al. (2012).

6.3. Summary of Moghimi et al. (2012)

In the previous Sections the author's own contributions to the joint publication of Moghimi et al. (2012) were presented. For contributions from other coauthors reference to Moghimi et al. (2012) is given. For completeness, in this Section the results of Moghimi et al. (2012) are summarised by the author of this thesis.

Based on the modified equations presented in the preceding Section, Moghimi et al. (2012) implemented the Radiation Stress formulation of Mellor (2011a) and the Vortex Force formulation of Bennis et al. (2011) into GETM. Their implementation within the same ocean model offered a direct comparison of the performance of both formulations. Since both formulations are based on assumptions limiting their practical applicability (discussed in detail in the original publications), the aim was to investigate these limitations from the practical side. Findings in the results of the performed simulations could indeed be linked to the corresponding theoretical limitation.

Coupled to the third-generation wind wave model SWAN (Booij et al., 1999; Holthuijsen, 2007), several simulations were performed to validate the model system and to directly compare the Radiation Stress formulation of Mellor (2011a) and the Vortex Force formulation of Bennis et al. (2011). The validation was carried out against measurements obtained in different flume experiments, representing wave regimes ranging from short period waves to swell, and on a realistic barred beach. Data exchange between SWAN and GETM was realised by the Model Coupling Toolkit (MCT; Larson et al., 2005). For the direct comparison of both formulations the model system was operated in one-way mode, with GETM only receiving identical mean wave properties of a stationary wave field from SWAN. For the realistic application of the validated model system, GETM also provided the mean sealevel and the ambient currents to SWAN. This two-way coupling offered the investigation of the mutual 3D interaction of waves and currents.

Both, the Radiation Stress formulation of Mellor (2011a) and the Vortex Force formulation of Bennis et al. (2011) reproduced the available measurements to a large extent. However, in particular for long-period waves (swell) the results of both formulations showed shortcomings. Within the Radiation Stress formulation the near-surface offshore-directed momentum release in steep shoaling regions due to the term $-\frac{\partial}{\partial x_\alpha} \left\{ \frac{E}{2} f_k^{\text{RS}} (\eta - z_k) \right\}$ in (6.4) induced unrealistic strong near-surface currents into the opposite direction of the propagating waves. On the other hand, within the Vortex Force formulation the additional forcing term $\bar{u}_{\beta,k}^{\text{Stokes}} \left(\frac{\partial \bar{u}_{\beta,k}^{\text{QE}}}{\partial x_\alpha} \right)_z$ in (6.7) was identified to be strongly divergent around main breaking points, overestimating the set-down and the undertow. Since these results of the Vortex Force formulation were still physically reasonable, the Vortex Force formulation was argued to provide a better representation of wind wave effects for a wider range of applications.

6.4. Conclusions and Outlook

In this Chapter modifications to the prognostic equations of GETM were presented to include the effects of wind waves. These modifications offer the implementation of both the Radiation Stress formulation of Mellor (2011a) and the Vortex Force formulation of Ardhuin et al. (2008) and Bennis et al. (2011). In Moghimi et al. (2012) the performance of both successfully implemented formulations was directly compared. Nevertheless, the implementation of Moghimi et al. (2012) left space for improvements.

Although not explicitly discussed by Moghimi et al. (2012), the 2D-mode of GETM (3.13a)–(3.13c) was modified in a similar way as the 3D mode. An additional interaction term was implemented to incorporate the depth-integrated forcing terms $\sum_{k=1}^{k_{\text{max}}} h_k F_{\alpha,k}^{\text{wave}}$ into the 2D-mode. Yet, this treatment can be improved by including additional wave forcing terms, consistent with the depth-integrated theories of Longuet-Higgins and Stewart (1964) and Phillips (1977), directly into the prognostic equations for the depth-averaged velocities (3.13b) and (3.13c). These would be updated every external time step Δt_{2D} and could earlier reflect changes in water depth and depth-averaged velocities, with the latter relevant within the Vortex Force formulation. Furthermore, after these changes GETM could be operated only in 2D-mode and with effects of unresolved wind waves included.

For the test cases investigated in Moghimi et al. (2012) the calculation of the Stokes drift (6.3a) and (6.3b) as well as the wave-induced pressure, i.e. $\frac{\|\mathbf{k}\|E}{\sinh(2\|\mathbf{k}\|(\eta+H))}$ in (6.7), based on mean wave properties was sufficient. However, for more realistic applications with random wave fields these terms should be obtained by integration over the wave-spectrum instead of in terms of the bulk wave-averaged wave energy E .

Finally, within the Vortex Force formulation the simplified forcing of Bennis et al. (2011), based on the assumption of weak vertical shear of the Eulerian wave-averaged velocity, can be relaxed towards the original forcing derived by Ardhuin et al. (2008). The practical implementation of the additional forcing terms was outlined by Michaud et al. (2012).

Chapter 7.

Summary and Outlook

In this thesis three approaches for the improvement of transport processes in coastal ocean models were discussed. These approaches addressed different levels of the modelling procedure.

The first approach addressed the truncation errors due to the discretisation. In this context a general analysis of Discrete Variance Decay (DVD) caused by advective and diffusive fluxes was established. To assess the performance of advection schemes, a new diagnostic method to quantify local DVD was developed. Based on this DVD analysis method a 3D dissipation analysis for staggered grids was presented. Implemented into the General Estuarine Transport Model (GETM) and applied to different test cases, the developed analysis tool was shown to give reasonable and reliable results. For a realistic model of the Western Baltic Sea the DVD analysis indicated spurious mixing of the same order as physical mixing. In contrast, the diagnosed spurious dissipation was at least one order of magnitude lower than the physical one. Missing higher-order advection schemes were implemented into the 2D-mode of GETM, directly implying an improved transport of quantities in the 3D-mode. To account for the increasing importance of physically induced dissipation and mixing, a Smagorinsky-type parameterisation for lateral diffusivities was implemented as well.

The second approach addressed approximations to the governing equations. In the light of the limited validity of the hydrostatic pressure assumption an alternative inclusion of missing nonhydrostatic dynamics into a hydrostatic model kernel was presented. The nonhydrostatic capability of the extended GETM was verified and validated by several nonhydrostatic benchmark test cases. However, stability issues limited the practical applicability of the implemented straight-forward extension. The origin of these stability issues could be identified and for weak nonhydrostatic regimes the stability issues were demonstrated to be manageable. With the extended GETM the importance of nonhydrostatic effects in the realistic Western Baltic Sea model was estimated. For the used spatial resolution the validity of the applied hydrostatic pressure assumption could be confirmed.

The third approach addressed again the governing equations, but considered the effects of unresolved wind waves. The necessary modifications to the governing equations of GETM to include these effects were presented. The modified equations offered the implementation of two different wave-averaged formulations recently established within the ocean modelling community. For both formulations the required wave properties had to be provided from a statistical wind wave model, coupled to GETM. For a detailed validation of the developed model system and its application to a realistic barred beach reference to Moghimi et al. (2012) was given. Therein the improved transports due to the inclusion of wind wave effects was demonstrated. Finally, various future improvements of the implementation were identified.

For the first two approaches a realistic model of the Western Baltic Sea was applied. This now validated model will be used in future studies for the investigation of internal waves in the Bornholm Basin. With the help of the developed DVD and dissipation analyses a bulk parameterisation for internal wave effects should be developed. For the needed high-resolution nestings the implemented nonhydrostatic extension will enable the possibly required relaxation of the hydrostatic pressure assumption. Even

more realistic results can be expected after coupling a wave model to the Western Baltic Sea model, of course based on the presented modifications to the governing equations.

Appendix A.

Constitutive relations

A.1. The Stress tensor

In a general derivation of the balance of momentum a stress tensor \underline{T} is present (see e.g. Spurk and Aksel, 2008). This has to be specified by a constitutive relation. In a fluid at rest only normal stresses due to the thermodynamic pressure are existing (Spurk and Aksel, 2008). In a moving fluid additional viscous and in case of unresolved motions also turbulent stresses occur:

$$T_{i,j} = -p\delta_{i,j} + T_{i,j}^{\text{visc}} + T_{i,j}^{\text{turb}}. \quad (\text{A.1})$$

A.1.1. The viscous stress tensor

In Newtonian fluids Hook's law linearly relates the viscous stresses to the velocity gradient (see e.g. Griffies, 2004):

$$T_{i,j}^{\text{visc}} = T_{i,j}^{\text{visc}} \left(0 + \frac{\partial u_l}{\partial x_k} \right) \approx 0 + \underbrace{\frac{\partial T_{i,j}^{\text{visc}}}{\partial \left(\frac{\partial u_l}{\partial x_k} \right)} (0)}_{=\mu_{i,j,k,l}} \frac{\partial u_l}{\partial x_k}. \quad (\text{A.2})$$

There are several constraints on the viscous stress tensor and thus the viscosity tensor $\mu_{i,j,k,l}$.

Symmetric stress tensor The balance of angular momentum requires a symmetric stress tensor (Spurk and Aksel, 2008), implying

$$\mu_{i,j,k,l} \equiv \mu_{j,i,k,l}. \quad (\text{A.3})$$

No stresses in case of pure rigid body rotation (Wajsowicz, 1993) $T_{i,j}^{\text{visc}} = \mu_{i,j,k,l} \frac{\partial u_l}{\partial x_k} = 0$ for $u_l = \varepsilon_{l,m,n} \Omega_m x_n$ yields $\varepsilon_{l,m,k} \mu_{i,j,k,l} = 0$ and thus

$$\mu_{i,j,k,l} \equiv \mu_{i,j,l,k}. \quad (\text{A.4})$$

Dissipation due to viscous stress tensor The stress power $\frac{\partial u_j}{\partial x_i} T_{i,j}$ transforms between kinetic and internal energy (see e.g. Spurk and Aksel, 2008). Following Kirwan (1969), the contribution of the viscous stress tensor is constrained to only dissipate kinetic into internal energy:

$$\phi = \frac{\partial u_j}{\partial x_i} T_{i,j}^{\text{visc}} \geq 0. \quad (\text{A.5})$$

Equations (A.2)–(A.5) imply $\phi = \mu_{i,j,k,l} S_{i,j} S_{k,l}$ with the deformation rate tensor

$$S_{i,j} = \frac{1}{2} \left(\frac{\partial u_i}{\partial x_j} + \frac{\partial u_j}{\partial x_i} \right) \quad (\text{A.6})$$

being the symmetric part of the velocity gradient. Since only the symmetric part of the viscosity tensor contributes to ϕ and Kirwan (1969) argued that only terms contributing to the dissipation are important, it is reasonable to constrain

$$\mu_{i,j,k,l} \equiv \mu_{k,l,i,j}. \quad (\text{A.7})$$

In 3D the constraints (A.3)–(A.7) reduce the independent elements of the viscosity tensor from 81 to 21. Further reduction is possible in case of (partial) isotropy. According to Aris (1989), full 3D isotropy (material isotropy of viscous effects) requires

$$\mu_{i,j,k,l} = \eta \delta_{i,j} \delta_{k,l} + \mu \delta_{i,k} \delta_{j,l} + \tilde{\mu} \delta_{i,l} \delta_{j,k}, \quad (\text{A.8})$$

and because of each constraint (A.3), (A.4) and (A.7),

$$\mu \equiv \tilde{\mu}. \quad (\text{A.9})$$

Thus, the viscous stress tensor is given by the Cauchy-Poisson-Law

$$T_{i,j}^{\text{visc}} = 2\mu S_{i,j} + \eta \frac{\partial u_k}{\partial x_k} \delta_{i,j}, \quad (\text{A.10})$$

with μ and η as (dynamic) shear and volume viscosity, respectively. The dissipation derives as

$$\phi = 2\mu S_{i,j} S_{i,j} + \eta \left(\frac{\partial u_k}{\partial x_k} \right)^2 \quad (\text{A.11})$$

and the constraint (A.5) is fulfilled for $\mu \geq 0$ and $\eta \geq -2\mu$.

With the deviatoric viscous stress tensor $T_{i,j}^{\text{visc,d}}$ and the bulk viscosity κ the viscous stress tensor can be expressed as

$$T_{i,j}^{\text{visc}} = \underbrace{2\mu \left[S_{i,j} - \frac{1}{\delta_{l,l}} \nabla \cdot \underline{u} \delta_{i,j} \right]}_{=T_{i,j}^{\text{visc,d}}} + \underbrace{\left(2\mu \frac{1}{\delta_{l,l}} + \eta \right)}_{=\kappa} \nabla \cdot \underline{u} \delta_{i,j}. \quad (\text{A.12})$$

For incompressible fluids $\left(\frac{\partial u_k}{\partial x_k} \equiv 0 \right)$ the last term in (A.12) vanishes. For compressible fluids it would add to the pressure in (A.1), yet according to the Stokes' hypothesis the bulk viscosity is assumed to vanish ($\kappa = 0$; see e.g. Spurk and Aksel, 2008). Thus, for both incompressible and compressible fluids the viscous stress tensor is (for the latter assumed to be) deviatoric.

A.1.2. The turbulent stress tensor

In the lack of a closed theory, the turbulent stress tensor is parameterised similar to the viscous stress tensor. As shown at the end of the previous Section, the viscous stress tensor is (in case of a compressible fluid assumed to be) deviatoric.

Therefore, in a first step the turbulent stress tensor is split into its deviatoric part $T_{i,j}^{\text{turb,d}}$ and a pressure-like term originating from the turbulent energy E^{turb} (Lilly, 1966; Germano, 1992):

$$\begin{aligned}
 T_{i,j}^{\text{turb}} &= -\rho_0 [\langle u_i u_j \rangle - \langle u_i \rangle \langle u_j \rangle] \\
 &= -\rho_0 \underbrace{\left[\langle u_i u_j \rangle - \langle u_i \rangle \langle u_j \rangle - \frac{1}{\delta_{l,l}} \underbrace{(\langle u_k u_k \rangle - \langle u_k \rangle \langle u_k \rangle)}_{=2E^{\text{turb}}} \delta_{i,j} \right]}_{=T_{i,j}^{\text{turb,d}}} - \rho_0 \underbrace{\frac{1}{\delta_{l,l}} \underbrace{(\langle u_k u_k \rangle - \langle u_k \rangle \langle u_k \rangle)}_{=2E^{\text{turb}}} \delta_{i,j}}_{=p^{\text{turb}}}.
 \end{aligned} \tag{A.13}$$

The turbulent pressure p^{turb} can be added to the thermodynamic pressure in (A.1) to yield a macro pressure (Hinze, 1975).

For the deviatoric turbulent stress tensor a similar form as for the viscous stress tensor (A.2) is assumed (Kamenkovich, 1967; Kirwan, 1969):

$$T_{i,j}^{\text{turb,d}} = \mu_{i,j,k,l}^{\text{turb}} \frac{\partial \langle u_l \rangle}{\partial x_k}. \tag{A.14}$$

Furthermore, the emphasis of the vertical axis in geophysical applications motivates the assumption of *transverse isotropy*. In agreement with the formulas presented by Kamenkovich (1967), Kirwan (1969) and Smith and McWilliams (2003) a transversely isotropic 4th-order turbulent viscosity tensor under constraints (A.3), (A.4) and (A.7) is given by

$$\begin{aligned}
 \mu_{i,j,k,l}^{\text{turb}} &= C_1 \delta_{i,3} \delta_{j,3} \delta_{k,3} \delta_{l,3} \\
 &\quad + C_2 (\delta_{i,3} \delta_{j,3} \delta_{k,l} + \delta_{k,3} \delta_{l,3} \delta_{i,j}) \\
 &\quad + C_3 (\delta_{i,3} \delta_{k,3} \delta_{j,l} + \delta_{i,3} \delta_{l,3} \delta_{j,k} + \delta_{j,3} \delta_{k,3} \delta_{i,l} + \delta_{j,3} \delta_{l,3} \delta_{i,k}) \\
 &\quad + C_4 \delta_{i,j} \delta_{k,l} \\
 &\quad + C_5 (\delta_{i,k} \delta_{j,l} + \delta_{i,l} \delta_{j,k}).
 \end{aligned} \tag{A.15}$$

This implies

$$T_{1,1}^{\text{turb,d}} = 2C_5 \frac{\partial \langle u \rangle}{\partial x} + C_4 \nabla \cdot \langle \underline{u} \rangle + C_2 \frac{\partial \langle w \rangle}{\partial z}, \quad (\text{A.16a})$$

$$T_{1,2}^{\text{turb,d}} = T_{2,1}^{\text{turb,d}} = C_5 \left(\frac{\partial \langle u \rangle}{\partial y} + \frac{\partial \langle v \rangle}{\partial x} \right), \quad (\text{A.16b})$$

$$T_{1,3}^{\text{turb,d}} = T_{3,1}^{\text{turb,d}} = (C_3 + C_5) \left(\frac{\partial \langle u \rangle}{\partial z} + \frac{\partial \langle w \rangle}{\partial x} \right), \quad (\text{A.16c})$$

$$T_{2,2}^{\text{turb,d}} = 2C_5 \frac{\partial \langle v \rangle}{\partial y} + C_4 \nabla \cdot \langle \underline{u} \rangle + C_2 \frac{\partial \langle w \rangle}{\partial z}, \quad (\text{A.16d})$$

$$T_{2,3}^{\text{turb,d}} = T_{3,2}^{\text{turb,d}} = (C_3 + C_5) \left(\frac{\partial \langle v \rangle}{\partial z} + \frac{\partial \langle w \rangle}{\partial y} \right), \quad (\text{A.16e})$$

$$T_{3,3}^{\text{turb,d}} = (C_2 + C_4) \nabla \cdot \langle \underline{u} \rangle + (C_1 + C_2 + 4C_3 + 2C_5) \frac{\partial \langle w \rangle}{\partial z}. \quad (\text{A.16f})$$

The constraint of a deviatoric turbulent stress tensor further decreases the number of independent elements:

$$T_{i,l}^{\text{turb,d}} = (C_1 + 3C_2 + 4C_3) \frac{\partial \langle w \rangle}{\partial z} + (C_2 + 3C_4 + 2C_5) \nabla \cdot \langle \underline{u} \rangle = 0. \quad (\text{A.17})$$

In any case $C_1 + 3C_2 + 4C_3 = 0$ is required, replacing (A.16f) by

$$T_{3,3}^{\text{turb,d}} = (C_2 + C_4) \nabla \cdot \langle \underline{u} \rangle + 2(C_5 - C_2) \frac{\partial \langle w \rangle}{\partial z}. \quad (\text{A.18})$$

Incompressible fluids

Only for incompressible fluids ($\nabla \cdot \langle \underline{u} \rangle \equiv 0$) the condition above is sufficient to guarantee a deviatoric turbulent stress tensor. As shown by Kamenkovich (1967), for incompressible fluids 3 turbulent viscosities can be identified in (A.16a)–(A.16e) and (A.18):

$$\mu^{\text{turb,h}} = C_5, \quad (\text{A.19a})$$

$$\mu^{\text{turb,v}} = C_3 + C_5, \quad (\text{A.19b})$$

$$\mu^{\text{turb,*}} = C_2. \quad (\text{A.19c})$$

Under the quasi-hydrostatic approximation the dissipation due to the deviatoric turbulent stress tensor for incompressible fluids is given by ($\alpha \in \{1, 2\}, j \in \{1, 2, 3\}$):

$$\begin{aligned} \phi_{\text{qh}}^{\text{turb}} &= \frac{\partial \langle u_\alpha \rangle}{\partial x_j} T_{j,\alpha}^{\text{turb,d}} \\ &= 2\mu^{\text{turb,h}} \left[\left(\frac{\partial \langle u \rangle}{\partial x} \right)^2 + \left(\frac{\partial \langle v \rangle}{\partial y} \right)^2 + \frac{1}{2} \left(\frac{\partial \langle u \rangle}{\partial y} + \frac{\partial \langle v \rangle}{\partial x} \right)^2 \right] \\ &\quad + \mu^{\text{turb,v}} \left[\left(\frac{\partial \langle u \rangle}{\partial z} \right)^2 + \left(\frac{\partial \langle v \rangle}{\partial z} \right)^2 \right] \\ &\quad - \mu^{\text{turb,*}} \left(\frac{\partial \langle w \rangle}{\partial z} \right)^2. \end{aligned} \quad (\text{A.20})$$

Constraint (A.5) is fulfilled for $\mu^{\text{turb,h}} \geq 0$, $\mu^{\text{turb,v}} \geq 0$ and $\mu^{\text{turb,*}} = 0$, leading to

$$T_{1,1}^{\text{turb,d}} = 2\mu^{\text{turb,h}} \frac{\partial \langle u \rangle}{\partial x}, \quad (\text{A.21a})$$

$$T_{2,1}^{\text{turb,d}} = T_{1,2}^{\text{turb,d}} = \mu^{\text{turb,h}} \left(\frac{\partial \langle u \rangle}{\partial y} + \frac{\partial \langle v \rangle}{\partial x} \right), \quad (\text{A.21b})$$

$$T_{3,1}^{\text{turb,d}} = \mu^{\text{turb,v}} \frac{\partial \langle u \rangle}{\partial z}, \quad (\text{A.21c})$$

$$T_{2,2}^{\text{turb,d}} = 2\mu^{\text{turb,h}} \frac{\partial \langle v \rangle}{\partial y}, \quad (\text{A.21d})$$

$$T_{3,2}^{\text{turb,d}} = \mu^{\text{turb,v}} \frac{\partial \langle v \rangle}{\partial z}. \quad (\text{A.21e})$$

Compressible fluids

If the fluid is compressible the additional constraint $C_2 + 3C_4 + 2C_5 = 3(C_2 + C_4) + 2(C_5 - C_2) = 0$ must be fulfilled in (A.17). As shown by Smagorinsky (1993), also in this case 3 turbulent viscosities can be identified in (A.16a)–(A.16e) and (A.18):

$$\mu^{\text{turb,h}} = C_5, \quad (\text{A.22a})$$

$$\mu^{\text{turb,v}} = C_3 + C_5, \quad (\text{A.22b})$$

$$\mu^{\text{turb,*}} = C_2 + C_4. \quad (\text{A.22c})$$

Under the quasi-hydrostatic approximation the dissipation due to the deviatoric turbulent stress tensor for compressible fluids is given by ($\alpha \in \{1, 2\}, j \in \{1, 2, 3\}$):

$$\begin{aligned} \phi_{\text{qh}}^{\text{turb}} &= \frac{\partial \langle u_\alpha \rangle}{\partial x_j} T_{j,\alpha}^{\text{turb,d}} \\ &= \mu^{\text{turb,h}} \left[\left(\frac{\partial \langle u \rangle}{\partial x} - \frac{\partial \langle v \rangle}{\partial y} \right)^2 + \left(\frac{\partial \langle u \rangle}{\partial y} + \frac{\partial \langle v \rangle}{\partial x} \right)^2 \right] \\ &\quad + \mu^{\text{turb,v}} \left[\left(\frac{\partial \langle u \rangle}{\partial z} \right)^2 + \left(\frac{\partial \langle v \rangle}{\partial z} \right)^2 \right] \\ &\quad - \frac{\mu^{\text{turb,*}}}{2} \left(\nabla \cdot \underline{u} - 3 \frac{\partial \langle w \rangle}{\partial z} \right) \left(\frac{\partial \langle u \rangle}{\partial x} + \frac{\partial \langle v \rangle}{\partial y} \right). \end{aligned} \quad (\text{A.23})$$

Constraint (A.5) is fulfilled for $\mu^{\text{turb,h}} \geq 0$, $\mu^{\text{turb,v}} \geq 0$ and $\mu^{\text{turb,*}} = 0$, leading to

$$T_{1,1}^{\text{turb,d}} = -T_{2,2}^{\text{turb,d}} = \mu^{\text{turb,h}} \left(\frac{\partial \langle u \rangle}{\partial x} - \frac{\partial \langle v \rangle}{\partial y} \right), \quad (\text{A.24a})$$

$$T_{2,1}^{\text{turb,d}} = T_{1,2}^{\text{turb,d}} = \mu^{\text{turb,h}} \left(\frac{\partial \langle u \rangle}{\partial y} + \frac{\partial \langle v \rangle}{\partial x} \right), \quad (\text{A.24b})$$

$$T_{3,1}^{\text{turb,d}} = \mu^{\text{turb,v}} \frac{\partial \langle u \rangle}{\partial z}, \quad (\text{A.24c})$$

$$T_{3,2}^{\text{turb,d}} = \mu^{\text{turb,v}} \frac{\partial \langle v \rangle}{\partial z}. \quad (\text{A.24d})$$

A.2. The heat flux

As done for the stress tensor in the preceding Section, the heat flux \underline{q} in the balance of energy has to be specified by a constitutive relation (Spurk and Aksel, 2008). The heat flux consists of molecular and in case of unresolved motions also of turbulent contributions:

$$q_i = q_i^{\text{mol}} + q_i^{\text{turb}}. \quad (\text{A.25})$$

A.2.1. The molecular heat flux

According to the Fourier law, the molecular heat flux can be related linearly to the temperature gradient (also see Kirwan, 1969):

$$q_i^{\text{mol}} = q_i^{\text{mol}} \left(0 + \frac{\partial T}{\partial x_j} \right) \approx 0 - \underbrace{\left(- \frac{\partial q_i^{\text{mol}}}{\partial \left(\frac{\partial T}{\partial x_j} \right)} (0) \right)}_{=\lambda_{i,j}} \frac{\partial T}{\partial x_j}. \quad (\text{A.26})$$

Since heat fluxes should decrease temperature variance, the corresponding variance decay rate $\chi(T)$ should be nonnegative (also see Kirwan, 1969):

$$\frac{1}{2} \chi(T) = -q_i^{\text{mol}} \frac{\partial T}{\partial x_i} = \lambda_{i,j} \frac{\partial T}{\partial x_j} \frac{\partial T}{\partial x_i} \geq 0. \quad (\text{A.27})$$

Only the symmetric part of the conductivity tensor $\lambda_{i,j}$ contributes to $\chi(T)$, therefore the conductivity tensor should be symmetric (Kirwan, 1969):

$$\lambda_{i,j} \equiv \lambda_{j,i}. \quad (\text{A.28})$$

Material isotropy of the molecular effects requires full 3D isotropy

$$\lambda_{i,j} = \lambda \delta_{i,j}, \quad (\text{A.29})$$

with $\lambda \geq 0$ in order to fulfil (A.27).

A.2.2. The turbulent heat flux

In the lack of a closed theory, the turbulent heat flux is parameterised similar to the molecular heat flux (also see Kamenkovich, 1967):

$$\begin{aligned} q_i^{\text{turb}} &= \rho_0 [\langle u_i T \rangle - \langle u_i \rangle \langle T \rangle] \\ &= -\lambda_{i,j}^{\text{turb}} \frac{\partial \langle T \rangle}{\partial x_j}. \end{aligned} \quad (\text{A.30})$$

In Kamenkovich (1967) and Kirwan (1969), a transversely isotropic 2nd-order turbulent conductivity tensor is given by

$$\lambda_{i,j}^{\text{turb}} = \lambda^{\text{turb,h}} \delta_{i,j} + (\lambda^{\text{turb,v}} - \lambda^{\text{turb,h}}) \delta_{i,3} \delta_{j,3}, \quad (\text{A.31})$$

yielding

$$q_1^{\text{turb}} = -\lambda^{\text{turb,h}} \frac{\partial \langle T \rangle}{\partial x}, \quad (\text{A.32a})$$

$$q_2^{\text{turb}} = -\lambda^{\text{turb,h}} \frac{\partial \langle T \rangle}{\partial y}, \quad (\text{A.32b})$$

$$q_3^{\text{turb}} = -\lambda^{\text{turb,v}} \frac{\partial \langle T \rangle}{\partial z}. \quad (\text{A.32c})$$

Constraint (A.27) requires $\lambda^{\text{turb,h}} \geq 0$ and $\lambda^{\text{turb,v}} \geq 0$.

Appendix B.

Discrete Variance Decay

B.1. Comments on higher-order TVD-schemes

Under certain conditions the higher-order TVD-schemes applied and analysed in Section 4.3 can become non-TVD (Mercier and Delhez, 2010). The limiters (4.33b)–(4.33d) are based on TVD conditions derived for 1D uniform flow on uniform grids. Thus, except for the setup investigated in Section 4.3.1, these schemes may generate and amplify local extremes.

The derivation of generally sufficient TVD conditions can be based on generalised versions of (4.31), (4.32) and (4.34):

$$\tilde{\varphi}_{i'}^{\pm} = \frac{1}{2} \Delta x_{i' \mp 1/2} \left(1 - \text{CFL}_{i', i' \mp 1/2}^{(n)} (\pm u_{i'}^{\pm}) \right) \frac{\varphi_{i' \pm 1/2}^{(n)} - \varphi_{i' \mp 1/2}^{(n)}}{\Delta x_{i'}}, \quad (\text{B.1})$$

$$\text{CFL}_{i', i}^{(n)}(u) = \frac{\Delta t A_{i'} u}{V_i^{(n)}}. \quad (\text{B.2})$$

$$r_{i'}^{\pm} = \frac{\left(\varphi_{i' \mp 1/2}^{(n)} - \varphi_{i' \mp 3/2}^{(n)} \right) / \Delta x_{i' \mp 1}}{\left(\varphi_{i' \pm 1/2}^{(n)} - \varphi_{i' \mp 1/2}^{(n)} \right) / \Delta x_{i'}}. \quad (\text{B.3})$$

Linear higher-order schemes can be recovered for:

$$\psi_{i'}^{\text{LW}, \pm} = 1 \quad ; \text{Lax and Wendroff (1960)}, \quad (\text{B.4a})$$

$$\psi_{i'}^{\text{WB}, \pm} = r_{i'}^{\pm} \quad ; \text{Warming and Beam (1976)}, \quad (\text{B.4b})$$

$$\psi_{i'}^{\text{P2}, \pm} = 1 - \frac{1}{3} \left(1 + \text{CFL}_{i', i' \mp 1/2}^{(n)} (\pm u_{i'}^{\pm}) \right) \frac{\Delta x_{i' \mp 1/2}}{\Delta x_{i'}} (1 - r_{i'}^{\pm}); \text{QUICKEST (Leonard, 1979)}. \quad (\text{B.4c})$$

However, linear higher-order schemes are not monotonicity-preserving (Godunov, 1959, 1960) and consequently not TVD (Harten, 1983). In contrast, nonlinear higher-order schemes can be TVD. Harten (1983) proved a scheme to be TVD, if it can be cast to the form

$$\varphi_i^{(n+1)} - \varphi_i^{(n)} = C_i^- \left(\varphi_{i+1}^{(n)} - \varphi_i^{(n)} \right) - C_i^+ \left(\varphi_i^{(n)} - \varphi_{i-1}^{(n)} \right), \quad (\text{B.5})$$

with

$$C_i^\pm \geq 0, \quad (\text{B.6a})$$

$$C_i^- + C_i^+ \leq 1. \quad (\text{B.6b})$$

Use of the discrete incompressibility constraint (obtained from (4.28) for $\varphi \equiv 1$) offers the substitution of $V_i^{(n)}$ and the reformulation of (4.28) with (4.29) and (B.1) into the Harten form (B.5) with

$$\begin{aligned} C_i^\pm = & \text{CFL}_{i\mp 1/2,i}^{(n+1)} \left(\pm u_{i\mp 1/2}^\pm \right) \left(1 - \frac{1}{2} \frac{\Delta x_{i\mp 1}}{\Delta x_{i\mp 1/2}} \left(1 - \text{CFL}_{i\mp 1/2,i\mp 1}^{(n)} \left(\pm u_{i\mp 1/2}^\pm \right) \right) \psi_{i\mp 1/2}^\pm \right) \\ & + \text{CFL}_{i\pm 1/2,i}^{(n+1)} \left(\pm u_{i\pm 1/2}^\pm \right) \frac{1}{2} \frac{\Delta x_i}{\Delta x_{i\mp 1/2}} \left(1 - \text{CFL}_{i\pm 1/2,i}^{(n)} \left(\pm u_{i\pm 1/2}^\pm \right) \right) \frac{\psi_{i\pm 1/2}^\pm}{r_{i\pm 1/2}^\pm}. \end{aligned} \quad (\text{B.7})$$

In principle, from the constraints (B.6a) and (B.6b) sufficient conditions for the limiters $\psi_{i'}^\pm$ in (B.7) should be deduced. However, the conditions recently established by Mercier and Delhez (2010) for equidistant grids are highly complex.

Therefore, in the present studies the traditional limiters based on the condition (see e.g. Hirsch, 2007),

$$0 \leq \psi_{i'}^\pm \leq \max \left(0, \min \left(\frac{2r_{i'}^\pm}{\text{CFL}_{i'} \left(\pm u_{i'}^\pm \right)}, \frac{2}{1 - \text{CFL}_{i'} \left(\pm u_{i'}^\pm \right)} \right) \right), \quad (\text{B.8})$$

derived from (B.7) for uniform flow on uniform grids, with $\text{CFL}_{i'}(u)$ and $r_{i'}^\pm$ defined in (4.32) and (4.34), are utilised. The P2-PDM limiter in (4.33d) is defined in such a way to always be inside the TVD region spanned by (B.8). According to Pietrzak (1998), the P2-PDM limiter recovers the ULTIMATE-QUICKEST scheme of Leonard (1991).

Sweby (1984) further restricted the TVD region by enforcing the limiter to be independent from the Courant number and to be a convex average of $\psi_{i'}^{\text{LW},\pm}$ and $\psi_{i'}^{\text{WB},\pm}$ given in (B.4a) and (B.4b), respectively:

$$\max\left(0, \min\left(\psi_{i'}^{\text{LW},\pm}, \psi_{i'}^{\text{WB},\pm}\right)\right) \leq \psi_{i'}^{\pm} \leq \max\left(0, \min\left(\max\left(\psi_{i'}^{\text{LW},\pm}, \psi_{i'}^{\text{WB},\pm}\right), 2r_{i'}^{\pm}, 2\right)\right). \quad (\text{B.9})$$

The lower and upper limits in (B.9) define the minmod and Superbee limiters given in (4.33b) and (4.33c), respectively.

B.2. DVD due to diffusion

Considering only diffusive fluxes, temporally discretised by the θ -method, the discrete transport equation (4.5) becomes:

$$\frac{V_i \varphi_i^{(n+1)} - V_i \varphi_i^{(n)}}{\Delta t} - \left[A_{i'} \frac{\nu_{i'}}{\Delta x_{i'}} \left[\theta \varphi_{i_*}^{(n+1)} + (1 - \theta) \varphi_{i_*}^{(n)} \right]_{i_*=i'-1/2}^{i_*=i'+1/2} \right]_{i'=i-1/2}^{i'=i+1/2} = 0. \quad (\text{B.10})$$

Since diffusion does not cause any mass transport, the volume of the FV-cell is constant. Multiplication of (B.10) with $(\varphi_i^{(n)} + \varphi_i^{(n+1)})$ yields the prognostic equation for the discrete second moment (Burchard, 2002b, Eq. (14))¹. After further reformulation of the sink terms due to subsequent use of (B.10), the prognostic equation for the discrete second moment can be derived as

$$\begin{aligned} & \frac{1}{V_i} \left(\frac{V_i (\varphi_i^{(n+1)})^2 - V_i (\varphi_i^{(n)})^2}{\Delta t} - \left[A_{i'} \frac{\nu_{i'}}{\Delta x_{i'}} \left[\theta (\varphi_{i_*}^{(n+1)})^2 + (1 - \theta) (\varphi_{i_*}^{(n)})^2 \right]_{i_*=i'-1/2}^{i_*=i'+1/2} \right]_{i'=i-1/2}^{i'=i+1/2} \right) \\ & = - \left(\theta \chi_i^{\text{ana}} (\varphi^{(n+1)}) + (1 - \theta) \chi_i^{\text{ana}} (\varphi^{(n)}) + \theta^2 \chi_i^{\text{num,d}} (\varphi^{(n+1)}) - (1 - \theta)^2 \chi_i^{\text{num,d}} (\varphi^{(n)}) \right) \leq 0, \end{aligned} \quad (\text{B.11})$$

with the *discrete* AVD rate (compare with (4.4))

$$\chi_i^{\text{ana}} (\varphi) = 2 \frac{\Delta x_{i-1/2} A_{i-1/2} \nu_{i-1/2} \left(\frac{\varphi_i - \varphi_{i-1}}{\Delta x_{i-1/2}} \right)^2 + \Delta x_{i+1/2} A_{i+1/2} \nu_{i+1/2} \left(\frac{\varphi_{i+1} - \varphi_i}{\Delta x_{i+1/2}} \right)^2}{2V_i} \geq 0, \quad (\text{B.12})$$

¹In Eq. (14) of Burchard (2002b) the typo $\sigma(\hat{u}_j - \hat{u}_{j-1})(\hat{u}_j - u_{j-1})$ must be replaced by $\sigma(\hat{u}_j - \hat{u}_{j-1})(u_j - \hat{u}_{j-1})$.

but also additional numerical contributions given in terms of the generalised Courant number (B.2):

$$\chi_i^{\text{num,d}}(\varphi) = \frac{\left(\left[\text{CFL}_{i,i'} \left(\frac{\nu_{i'}}{\Delta x_{i'}} \right) [\varphi_{i*}^{i*}]_{i*=i'-1/2}^{i*=i'+1/2} \right]_{i'=i-1/2}^{i'=i+1/2} \right)^2}{\Delta t}. \quad (\text{B.13})$$

Following Burchard (2002b), the conservative transfer of variance between resolved and unresolved scales requires the numerical contributions $\chi_i^{\text{num,d}}$ to be considered as sources within the microstructure variance equations of turbulence models. From $\mathcal{O}(\chi_i^{\text{num,d}}/\chi_i^{\text{ana}}) = \text{CFL}_i \left(\frac{\nu}{\Delta x} \right)$ the possible significance of the numerical contributions, in particular associated with vertical diffusion in layered ocean models, can be estimated.

B.3. DVD due to the explicit FOU scheme

For the explicit FOU scheme, recovered by (4.33a), (B.7) reduces to $C_i^\pm = \text{CFL}_{i\mp 1/2,i}^{(n+1)} (\pm u_{i\mp 1/2}^\pm)$. Multiplication of (B.5) with $(\varphi_i^{(n)} + \varphi_i^{(n+1)})$, use of (B.5) to substitute $\varphi_i^{(n+1)}$ and final reformulation with the discrete incompressibility constraint yields the associated prognostic equation for the discrete second moment:

$$\begin{aligned} & \frac{1}{V_i^{(n+1)}} \left(\frac{V_i^{(n+1)} (\varphi_i^{(n+1)})^2 - V_i^{(n)} (\varphi_i^{(n)})^2}{\Delta t} + [A_{i'} u_{i'} (\tilde{\varphi}_{i'})^2]_{i'=i-1/2}^{i'=i+1/2} \right) \\ &= - \left(C_i^- (1 - C_i^-) \left(\frac{\varphi_{i+1}^{(n)} - \varphi_i^{(n)}}{\Delta x_i} \right)^2 + C_i^+ (1 - C_i^+) \left(\frac{\varphi_i^{(n)} - \varphi_{i-1}^{(n)}}{\Delta x_i} \right)^2 \right) \frac{\Delta x_i^2}{\Delta t} \\ & \quad - 2C_i^- C_i^+ \left(\frac{\varphi_{i+1}^{(n)} - \varphi_i^{(n)}}{\Delta x_i} \right) \left(\frac{\varphi_i^{(n)} - \varphi_{i-1}^{(n)}}{\Delta x_i} \right) \frac{\Delta x_i^2}{\Delta t} \quad (\text{B.14}) \end{aligned}$$

For unidirectional flow, e.g. $u_{i'} > 0$, (B.14) is equivalent to Eq. (24) in Burchard (2012). In this case from the right-hand side of (B.14) the local DVD rate

$$\chi_i^{\text{FOU,(n+1)}} = 2\nu_i^{\text{FOU}} \left(\frac{\varphi_i^{(n)} - \varphi_{i-1}^{(n)}}{\Delta x_i} \right)^2 \quad (\text{B.15})$$

with the well-known expression for the numerical diffusivity of the explicit FOU scheme

$$\nu_i^{\text{FOU}} = \frac{1}{2} \text{CFL}_{i-1/2,i}^{(n+1)}(u_{i-1/2}) \left(1 - \text{CFL}_{i-1/2,i}^{(n+1)}(u_{i-1/2})\right) \frac{\Delta x_i^2}{\Delta t} \quad (\text{B.16})$$

can be deduced (Molenkamp, 1968).

B.4. An alternative derivation of χ^{K13}

Formally (4.28) can be split into two steps,

$$V_i^{(*)} \varphi_i^{(*)} = V_i^{(n)} \varphi_i^{(n)} - \Delta t \left[A_{i+1/2} u_{i+1/2}^+ \tilde{\varphi}_{i+1/2} - A_{i-1/2} u_{i-1/2}^- \tilde{\varphi}_{i-1/2} \right], \quad (\text{B.17a})$$

$$V_i^{(n+1)} \varphi_i^{(n+1)} = V_i^{(*)} \varphi_i^{(*)} - \Delta t \left[A_{i+1/2} u_{i+1/2}^- \tilde{\varphi}_{i+1/2} - A_{i-1/2} u_{i-1/2}^+ \tilde{\varphi}_{i-1/2} \right], \quad (\text{B.17b})$$

with u_v^\pm defined in (4.30a) and (4.30b).

Following Prather (1986), the first step (B.17a) represents the *decomposition* of the old FV-cell $^{(n)}$ into the subvolumes to be advected out to the neighbouring cells and into the portion $^{(*)}$ that remains in the cell. In the second step (B.17b) the new FV-cell $^{(n+1)}$ is obtained by *recombination* of the portion remained in the cell and the subvolumes advected into the cell. This recombination is the ‘‘Average’’ step of the Reconstruct-Evolve-Average algorithm described by LeVeque (2002). A simple example for uniform flow is sketched in Figure B.1, generalising Fig. 1 of Morales Maqueda and Holloway (2006).

Based on the split (B.17a) and (B.17b), for explicit schemes Morales Maqueda and Holloway (2006) motivated an alternative derivation of the local DVD rate associated with (4.28). The existence of subvolumes offers a physically sound definition of variance inside each FV-cell².

²Originally, within their analysis of the SOM-scheme, Morales Maqueda and Holloway (2006) based their variance calculations on a quadratic tracer distribution inside each subvolume.

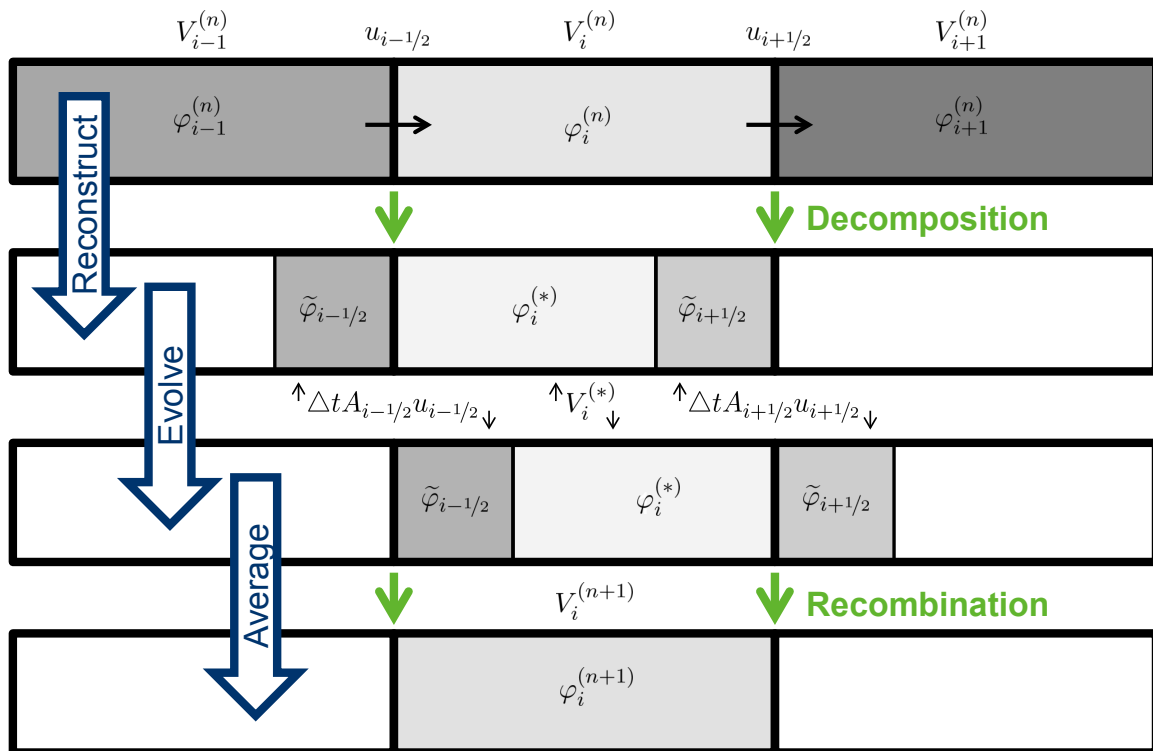


Figure B.1.: Advection in a FV-framework (adapted from Morales Maqueda and Holloway (2006)): The schema shows the decomposition of FV-cells into subvolumes, to be advected, and their recombination on a fixed grid for uniform 1D flow. Only the subvolumes affecting the central cell are drawn. The grey shade of the subvolumes indicates the value of φ . The reader is referred to the main text for the definition of symbols. It should be noted that the schema only depicts the budget of subvolumes.

Here, *before the decomposition* and *after the recombination* the FV-cells do not contain any subvolumes and thus no variance. However, *after the decomposition* the variance inside the FV-cell can be quantified according to:

$$\begin{aligned}
 \sigma_{V_i^{(n+)}}^2(\varphi) &= \langle \varphi^2 \rangle_{V_i^{(n+)}} - \langle \varphi \rangle_{V_i^{(n+)}}^2 \\
 &= \frac{1}{V_i^{(n)}} \left(V_i^{(*)} \left(\varphi_i^{(*)} \right)^2 + \Delta t A_{i+1/2} u_{i+1/2}^+ \left(\tilde{\varphi}_{i+1/2} \right)^2 - \Delta t A_{i-1/2} u_{i-1/2}^- \left(\tilde{\varphi}_{i-1/2} \right)^2 \right) \\
 &\quad - \left(\frac{1}{V_i^{(n)}} \left(V_i^{(*)} \varphi_i^{(*)} + \Delta t A_{i+1/2} u_{i+1/2}^+ \tilde{\varphi}_{i+1/2} - \Delta t A_{i-1/2} u_{i-1/2}^- \tilde{\varphi}_{i-1/2} \right) \right)^2 \\
 \stackrel{\text{(B.17a)}}{=} &\frac{1}{V_i^{(n)}} \left(V_i^{(*)} \left(\varphi_i^{(*)} \right)^2 + \Delta t A_{i+1/2} u_{i+1/2}^+ \left(\tilde{\varphi}_{i+1/2} \right)^2 - \Delta t A_{i-1/2} u_{i-1/2}^- \left(\tilde{\varphi}_{i-1/2} \right)^2 \right) \\
 &\quad - \frac{1}{V_i^{(n)}} \left(V_i^{(n)} \left(\varphi_i^{(n)} \right)^2 \right). \tag{B.18}
 \end{aligned}$$

Thus, except for the explicit FOU scheme ($\varphi_i^{(*)} \equiv \tilde{\varphi}_{i\pm 1/2} \equiv \varphi_i^{(n)}$), the decomposition causes a variance growth $(\Delta\sigma^2)_i^{\text{d},(n)} = \sigma_{V_i^{(n+)}}^2 - 0$ inside the FV-cell. This possible variance growth during the decomposition was not identified by Morales Maqueda and Holloway (2006). Similar to (B.18), the variance inside the FV-cell *before the recombination* can be quantified:

$$\begin{aligned}
 \sigma_{V_i^{(n+1-)}}^2(\varphi) &= \langle \varphi^2 \rangle_{V_i^{(n+1-)}} - \langle \varphi \rangle_{V_i^{(n+1-)}}^2 \\
 \stackrel{\text{(B.17b)}}{=} &\frac{1}{V_i^{(n+1)}} \left(V_i^{(*)} \left(\varphi_i^{(*)} \right)^2 - \Delta t A_{i+1/2} u_{i+1/2}^- \left(\tilde{\varphi}_{i+1/2} \right)^2 + \Delta t A_{i-1/2} u_{i-1/2}^+ \left(\tilde{\varphi}_{i-1/2} \right)^2 \right) \\
 &\quad - \frac{1}{V_i^{(n+1)}} \left(V_i^{(n+1)} \left(\varphi_i^{(n+1)} \right)^2 \right). \tag{B.19}
 \end{aligned}$$

With the variance decay caused by the recombination $(\Delta\sigma^2)_i^{\text{r},(n+1)} = 0 - \sigma_{V_i^{(n+1-)}}^2$, the alternative local DVD rate (4.36b) can be rederived by means of

$$\chi_i^{\text{K13},(n+1)} = -\frac{1}{\Delta t V_i^{(n+1)}} \left(V_i^{(n)} (\Delta\sigma^2)_i^{\text{d},(n)} + V_i^{(n+1)} (\Delta\sigma^2)_i^{\text{r},(n+1)} \right). \tag{B.20}$$

Appendix C.

The temporal resolution of nonhydrostatic effects

The one-stage AR-IIR filter (5.10) requires the storage of only one previous stage $\bar{b}_{\text{nh}}^{(n,l-1)}$. However, expansion with $b_{\text{nh}}^{(n,0)} = b_{\text{nh}}^{(n-1,N_{\text{it}})}$ shows that the filter actually operates as a cumulative average with fixed and normalised weights $\theta_m = (1 - \theta)^m \theta$:

$$\bar{b}_{\text{nh}}^{(n,l)} = \sum_{m=0}^{nN_{\text{it}}+l-1} \theta_m b_{\text{nh}}^{(\lfloor (nN_{\text{it}}+l-m)/N_{\text{it}} \rfloor, (nN_{\text{it}}+l-m)\%N_{\text{it}})} + (1 - \theta)^{nN_{\text{it}}+l} \bar{b}_{\text{nh}}^{(0,0)}. \quad (\text{C.1})$$

Slightly obscured by the floor function $\lfloor \cdot \rfloor$ and the modulo operation $\%$, this filter simply averages the current value $b_{\text{nh}}^{(n,l)}$ with all unfiltered ones from previous time stages and iterations. For $N_{\text{it}} = 1$ the expansion reduces to the more intuitive form

$$\bar{b}_{\text{nh}}^{(n)} = \sum_{m=0}^{n-1} \theta_m b_{\text{nh}}^{(n-m)} + (1 - \theta)^n \bar{b}_{\text{nh}}^{(0)}. \quad (\text{C.2})$$

Due to the strictly monotonically decreasing series $(\theta_m)_{m \in [0, nN_{\text{it}}+l]}$, the filtering of strong step-to-step oscillations is only possible with a very small weight θ . For small filter weights a great contribution to the first filtered values is given by zero initial values ($\bar{b}_{\text{nh}}^{(0,0)} = 0$). This inherent hydrostatic run-up stabilises the first internal time steps, usually containing a huge vertical acceleration due to the initial resting but maybe unstable state.

The memory effect of the filter determines the temporal resolution of nonhydrostatic effects Δt_{nh} . The latter is defined as the elapsed interval, in which a prescribed contribution to the filtered $\bar{b}_{\text{nh}}^{(n,l)}$ originates in. The contribution is given by $\bar{\theta} \in]0, 1]$ and determines the number of included stages M by the relation:

$$\sum_{m=0}^{M-1} \theta_m \geq \bar{\theta}. \quad (\text{C.3})$$

For the analysis within this thesis $\bar{\theta} = 99\%$ was chosen, implying that at least 99% of the contribution to $\bar{b}_{\text{nh}}^{(n,l)}$ originates in the elapsed interval Δt_{nh} . With $\lceil \cdot \rceil$ representing the ceiling function, inversion of (C.3) yields

$$M \geq \left\lceil \frac{\ln(1 - \bar{\theta})}{\ln(1 - \theta)} \right\rceil. \quad (\text{C.4})$$

Thus, the temporal resolution of nonhydrostatic effects can finally be estimated as

$$\Delta t_{\text{nh}} = \left\lceil \frac{\ln(1 - \bar{\theta})}{\frac{\ln(1 - \theta)}{N_{\text{it}}}} \right\rceil \Delta t_{3\text{D}}. \quad (\text{C.5})$$

Nomenclature

AVD	analytical variance decay, page 22
CFD	Computational Fluid Dynamics, page 51
CFL	Courant-Friedrichs-Lewy, page 16
DNS	Direct Numerical Simulation, page 9
DVD	discrete variance decay, page 23
FOU	First-Order Upstream, page 21
FV	Finite Volume, page 23
GETM	General Estuarine Transport Model, page 11
GLM	Generalised Lagrangian Mean, page 75
NSE	Navier-Stokes Equations, page 5
TVD	Total Variation Dimishing, page 11
\cdot	scalar product, page V
∇	Nabla operator (unit: m^{-1}), page V
η	surface elevation (unit: m), page 6
ν	diffusivity (unit: $\text{m}^2 \text{s}^{-1}$), page 12
ρ_0	reference density (unit: Kg m^{-3}), page 5
b	buoyancy (unit: m s^{-2}), page 7
D	total water depth (unit: m), page 15
f_h	horizontal Coriolis parameter (unit: s^{-1}), page 5
f_v	vertical Coriolis parameter, inertial frequency (unit: s^{-1}), page 5
g	gravitational acceleration (unit: m s^{-2}), page 5
H	still water depth (unit: m), page 6
h_k	layer height (unit: m), page 13
w^s	grid-related vertical velocity (unit: m s^{-1}), page 13

Bibliography

- Andrews, D.G., McIntyre, M.E., 1978a. An exact theory of nonlinear waves on a Lagrangian-mean flow. *Journal of Fluid Mechanics* 89, 609–646.
- Andrews, D.G., McIntyre, M.E., 1978b. On wave-action and its relatives. *Journal of Fluid Mechanics* 89, 647–664.
- Arakawa, A., 1966. Computational Design for Long-Term Numerical Integration of the Equations of Fluid Motion: Two-Dimensional Incompressible Flow. Part I. *Journal of Computational Physics* 1, 119–143.
- Arakawa, A., Lamb, V.R., 1977. Computational Design of the Basic Dynamical Processes of the UCLA General Circulation Model, in: Chang, J. (Ed.), *General Circulation Models of the Atmosphere*. Academic Press. volume 17 of *Methods in Computational Physics: Advances in Research and Applications*, pp. 173–265.
- Ardhuin, F., Raschle, N., Belibassakis, K.A., 2008. Explicit wave-averaged primitive equations using a generalized Lagrangian mean. *Ocean Modelling* 20, 35–60.
- Aris, R., 1989. *Vectors, Tensors and the Basic Equations of Fluid Mechanics*. Dover Publications, Inc.
- Auclair, F., Estournel, C., Floor, J.W., Herrmann, M.J., Nguyen, C., Marsaleix, P., 2011. A non-hydrostatic algorithm for free-surface ocean modelling. *Ocean Modelling* 36, 49–70.
- Bennis, A.C., Ardhuin, F., 2011. Comments on "The Depth-Dependent Current and Wave Interaction Equations: A Revision". *Journal of Physical Oceanography* 41, 2008–2012.
- Bennis, A.C., Ardhuin, F., Dumas, F., 2011. On the coupling of wave and three-dimensional circulation models: Choice of theoretical framework, practical implementation and adiabatic tests. *Ocean Modelling* 40, 260–272.
- Bergh, J., Berntsen, J., 2010. The surface boundary condition in nonhydrostatic ocean models. *Ocean Dynamics* 60, 301–315.
- Berntsen, J., 2000. *USERS GUIDE for a modesplit σ -coordinate numerical ocean model*. Technical Report 135. Department of Applied Mathematics, University of Bergen.
- Berntsen, J., Furnes, G., 2005. Internal pressure errors in sigma-coordinate ocean models – sensitivity of the growth of the flow to the time stepping method and possible non-hydrostatic effects. *Continental Shelf Research* 25, 829–848.
- Berntsen, J., Xing, J., Alendal, G., 2006. Assessment of non-hydrostatic ocean models using laboratory scale problems. *Continental Shelf Research* 26, 1433–1447.
- Berntsen, J., Xing, J., Davies, A.M., 2008. Numerical studies of internal waves at a sill: Sensitivity to horizontal grid size and subgrid scale closure. *Continental Shelf Research* 28, 1376–1393.
- Berntsen, J., Xing, J., Davies, A.M., 2009. Numerical studies of flow over a sill: sensitivity of the non-hydrostatic effects to the grid size. *Ocean Dynamics* 59, 1043–1059.

- Blumberg, A.F., Mellor, G.L., 1987. A Description of a Three-Dimensional Coastal Ocean Circulation Model, in: Heaps, N.S. (Ed.), *Three Dimensional Coastal Ocean Models*. American Geophysical Union. volume 4.
- Booij, N., Ris, R.C., Holthuijsen, L.H., 1999. A third-generation wave model for coastal regions 1. Model description and validation. *Journal of Geophysical Research* 104 (C4), 7649–7666.
- Browning, G.L., Holland, W.R., Kreiss, H.O., Worley, S.J., 1990. An accurate hyperbolic system for approximately hydrostatic and incompressible oceanographic flows. *Dynamics of Atmospheres and Oceans* 14, 303–332.
- Burchard, H., 2001. Simulating the Wave-Enhanced Layer under Breaking Surface Waves with Two-Equation Turbulence Models. *Journal of Physical Oceanography* 31, 3133–3145.
- Burchard, H., 2002a. *Applied Turbulence Modelling in Marine Waters*. Springer.
- Burchard, H., 2002b. Energy-conserving discretisation of turbulent shear and buoyancy production. *Ocean Modelling* 4, 347–361.
- Burchard, H., 2012. Quantification of numerically induced mixing and dissipation in discretisations of shallow water equations. *International Journal on Geomathematics* 3, 51–65.
- Burchard, H., Bolding, K., 2002. GETM – a General Estuarine Transport Model. Scientific Documentation. Technical Report EUR 20253 EN. European Commission.
- Burchard, H., Bolding, K., Umlauf, L., 2013. GETM – Source Code and Test Case Documentation.
- Burchard, H., Bolding, K., Villarreal, M.R., 2004. Three-dimensional modelling of estuarine turbidity maxima in a tidal estuary. *Ocean Dynamics* 54, 250–265.
- Burchard, H., Gräwe, U., 2013. Quantification of Numerical and Physical Mixing in Coastal Ocean Model Applications, in: Ansorge, R. and Bijl, H. and Meister, A. and Sonar, T. (Ed.), *Recent developments in the Numerics of Nonlinear Hyperbolic Conservation Laws*. Springer. volume 120 of *Notes on Numerical Fluid Mechanics and Multidisciplinary Design*, pp. 89–103.
- Burchard, H., Janssen, F., Bolding, K., Umlauf, L., Rennau, H., 2009. Model simulations of dense bottom currents in the Western Baltic Sea. *Continental Shelf Research* 29, 205–220.
- Burchard, H., Lass, H.U., Mohrholz, V., Umlauf, L., Sellschopp, J., Fiekas, V., Bolding, K., Arneborg, L., 2005. Dynamics of medium-intensity dense water plumes in the Arkona Basin, Western Baltic Sea. *Ocean Dynamics* 55, 391–402.
- Burchard, H., Petersen, O., 1997. Hybridization between σ - and z-co-ordinates for improving the internal pressure gradient calculation in marine models with steep bottom slopes. *International Journal for Numerical Methods in Fluids* 25, 1003–1023.
- Burchard, H., Rennau, H., 2008. Comparative quantification of physically and numerically induced mixing in ocean models. *Ocean Modelling* 20, 293–311.
- Canuto, V.M., Howard, A., Cheng, Y., Dubovikov, M.S., 2001. Ocean Turbulence. Part I: One-Point Closure Model—Momentum and Heat Vertical Diffusivities. *Journal of Physical Oceanography* 31, 1413–1426.
- Carter, G.S., Fringer, O.B., Zaron, E.D., 2012. Regional models of internal tides. *Oceanography* 25, 56–65.
- Casulli, V., 1999. A semi-implicit finite difference method for non-hydrostatic, free-surface flows. *International Journal for Numerical Methods in Fluids* 30, 425–440.
- Casulli, V., Stelling, G.S., 1998. Numerical Simulation of 3D Quasi-Hydrostatic, Free-Surface Flows. *Journal of Hydraulic Engineering* 124, 678–856.

- Casulli, V., Zanolli, P., 2002. Semi-Implicit Numerical Modeling of Nonhydrostatic Free-Surface Flows for Environmental Problems. *Mathematical and Computer Modelling* 36, 1131–1149.
- Chen, C., Liu, H., Beardsley, R.C., 2003. An Unstructured Grid, Finite-Volume, Three-Dimensional, Primitive Equations Ocean Model: Application to Coastal Ocean and Estuaries. *Journal of Atmospheric and Oceanic Technology* 20, 159–186.
- Chorin, A.J., 1967a. A Numerical Method for Solving Incompressible Viscous Flow Problems. *Journal of Computational Physics* 2, 12–26.
- Chorin, A.J., 1967b. The Numerical Solution of the Navier-Stokes Equations for an Incompressible Fluid. *Bulletin of the American Mathematical Society* 73, 928–931.
- Chorin, A.J., 1968. Numerical Solution of the Navier-Stokes Equations. *Mathematics of Computation* 22, 745–762.
- Courant, R., Friedrichs, K., Lewy, H., 1928. Über die partiellen Differenzgleichungen der mathematischen Physik. *Mathematische Annalen* 100, 32–74.
- Craig, P.D., Banner, M.L., 1994. Modeling Wave-Enhanced Turbulence in the Ocean Surface Layer. *Journal of Physical Oceanography* 24, 2546–2559.
- Craik, A.D.D., Leibovich, S., 1976. A rational model for Langmuir circulations. *Journal of Fluid Mechanics* 73, 401–426.
- Davies, A.M., Xing, J., 2007. On the influence of stratification and tidal forcing upon mixing in sill regions. *Ocean Dynamics* 57, 431–451.
- Dietrich, D.E., Ko, D.S., 1994. A semi-collocated ocean model based on the SOMS approach. *International Journal for Numerical Methods in Fluids* 19, 1103–1113.
- Dietrich, D.E., Lin, C.A., 2002. Effects of hydrostatic approximation and resolution on the simulation of convective adjustment. *Tellus* 54A, 34–43.
- Dietrich, D.E., Marietta, M.G., Roache, P.J., 1987. An ocean modelling system with turbulent boundary layers and topography: numerical description. *International Journal for Numerical Methods in Fluids* 7, 833–855.
- Durrant, D.R., 2010. *Numerical Methods for Fluid Dynamics*. Springer.
- Ferziger, J.H., Perić, M., 1997. *Computational Methods for Fluid Dynamics*. ISBN 3-540-59434-5, Springer.
- Fletcher, C.A.J., 1988. *Computational Techniques for Fluid Dynamics 2. Specific Techniques for Different Flow Categories*. volume 2. Springer. 1st edition.
- Foias, C., Manley, O.P., Rosa, R., Témam, R., 2001. *Navier-Stokes Equations and Turbulence*. volume 83 of *Encyclopedia of Mathematics and its Applications*. Cambridge University Press.
- Fringer, O.B., Armfield, S.W., Street, R.L., 2005. Reducing numerical diffusion in interfacial gravity wave simulations. *International Journal for Numerical Methods in Fluids* 49, 301–329.
- Fringer, O.B., Gerritsen, M.G., Street, R.L., 2006. An unstructured-grid, finite-volume, nonhydrostatic, parallel coastal ocean simulator. *Ocean Modelling* 14, 139–173.
- Gaarhuis, J., 1995. A non-hydrostatic pressure model for shallow water flow. Technical Report. Technische Universiteit Eindhoven Instituut Vervolgopleidingen.
- Gerkema, T., Zimmerman, J.T.F., Maas, L.R.M., van Haren, H., 2008. Geophysical and Astrophysical Fluid Dynamics beyond the Traditional Approximation. *Reviews of Geophysics* 46.

- Germano, M., 1992. Turbulence: the filtering approach. *Journal of Fluid Mechanics* 238, 325–336.
- Getzlaff, J., Nurser, G., Oschlies, A., 2010. Diagnostics of diapycnal diffusivity in z-level ocean models part I: 1-Dimensional case studies. *Ocean Modelling* 35, 173–186.
- Getzlaff, J., Nurser, G., Oschlies, A., 2012. Diagnostics of diapycnal diffusion in z-level ocean models. Part II: 3-Dimensional OGCM. *Ocean Modelling* 45–46, 27–36.
- Geurts, B.J., Holm, D.D., 2006. Commutator errors in large-eddy simulation. *Journal of Physics A: Mathematical and General* 39, 2213–2229.
- Godunov, S.K., 1959. A difference method for numerical calculation of discontinuous solutions of the equations of hydrodynamics. *Mat. Sb. (N.S.)* 47 (89), 271–306.
- Godunov, S.K., 1960. A difference method for the numerical calculation of discontinuous solutions of hydrodynamic equations Translated from *Mat. Sb. (N.S.)*, Vol. 47(89), No. 3 (1959), 271–306.
- Gräwe, U., Burchard, H., 2012. Storm surges in the Western Baltic Sea: the present and a possible future. *Climate Dynamics* 39, 165–183.
- Gräwe, U., Friedland, R., Burchard, H., 2013. The future of the western Baltic Sea: two possible scenarios. *Ocean Dynamics* 63, 901–921.
- Gräwe, U., Holtermann, P., Klingbeil, K., Burchard, H., in prep. Advantages of vertically adaptive coordinates in numerical models of stratified shelf seas. *Ocean Modelling*.
- Griebel, M., Dornseifer, T., Neunhoffer, T., 1998. *Numerical Simulation in Fluid Dynamics*. Society for Industrial and Applied Mathematics.
- Griffies, S.M., 2004. *Fundamentals of Ocean Climate Models*. Princeton University Press.
- Griffies, S.M., Pacanowski, R.C., Hallberg, R.W., 2000. Spurious Diapycnal Mixing Associated with Advection in a z-Coordinate Ocean Model. *Monthly Weather Review* 128, 538–564.
- Griffiths, R.W., Linden, P.F., 1981. The stability of vortices in a rotating, stratified fluid. *Journal of Fluid Mechanics* 105, 283–316.
- Härtel, C., Meiburg, E., Necker, F., 2000. Analysis and direct numerical simulation of the flow at a gravity-current head. Part 1. Flow topology and front speed for slip and no-slip boundaries. *Journal of Fluid Mechanics* 418, 189–212.
- Harten, A., 1983. High Resolution Schemes for Hyperbolic Conservation Laws. *Journal of Computational Physics* 49, 357–393.
- Heggelund, Y., Vikebø, F., Berntsen, J., Furnes, G., 2004. Hydrostatic and non-hydrostatic studies of gravitational adjustment over a slope. *Continental Shelf Research* 24, 2133–2148.
- Hinze, J.O., 1975. *Turbulence*. Number 1 in McGraw-Hill series in mechanical engineering, McGraw-Hill, Inc.. 2nd edition.
- Hirsch, C., 2007. *Numerical Computations of Internal and External Flows: Fundamentals of Computational Fluid Dynamics*. volume 1. Elsevier.
- Hofmeister, R., Beckers, J.M., Burchard, H., 2011. Realistic modelling of the exceptional inflows into the central Baltic Sea in 2003 using terrain-following coordinates. *Ocean Modelling* 39, 233–247.
- Hofmeister, R., Burchard, H., Beckers, J.M., 2010. Non-uniform adaptive vertical grids for 3D numerical ocean models. *Ocean Modelling* 33, 70–86.
- Holleman, R., Fringer, O.B., Stacey, M., 2013. Numerical diffusion for flow-aligned unstructured grids with application to estuarine modeling. *International Journal for Numerical Methods in Fluids* 72, 1117–1145.

- Holtermann, P., Burchard, H., Gräwe, U., Klingbeil, K., Umlauf, L., in prep. Evolution of an anthropogenic tracer in a stratified basin with intensified boundary mixing. *Journal of Geophysical Research (Oceans)* .
- Holthuijsen, L.H., 2007. *Waves in Oceanic and Coastal Waters*. Cambridge University Press.
- Horn, D.A., Imberger, J., Ivey, G.N., 2000. Internal Solitary Waves in Lakes - a Closure Problem for Hydrostatic Models. CWR reference ED 1477 DH.
- Horn, D.A., Imberger, J., Ivey, G.N., 2001. The degeneration of large-scale interfacial gravity waves in lakes. *Journal of Fluid Mechanics* 434, 181–207.
- Ilicak, M., Adcroft, A.J., Griffies, S.M., Hallberg, R.W., 2012. Spurious diapycnal mixing and the role of momentum closure. *Ocean Modelling* 45-46, 37–58.
- Jachec, S.M., Fringer, O.B., Gerritsen, M.G., Street, R.L., 2006. Numerical simulation of internal tides and the resulting energetics within Monterey Bay and the surrounding area. *Geophysical Research Letters* 33.
- James, I.D., 1996. Advection schemes for shelf sea models. *Journal of Marine Systems* 8, 237–254.
- Janin, J.M., Lepeintre, F., Pechon, P., 1992. TELEMAC-3D: A finite element code to solve 3D free surface flow problems. Technical Report HE 42/92.07. Electricité de France, Département Laboratoire National d'Hydraulique.
- Jankowski, J.A., 1999. A non-hydrostatic model for free surface flows. Ph.D. thesis. Universität Hannover.
- Jenkins, A.D., 1989. The Use of a Wave Prediction Model for Driving a Near-Surface Current Model. *Deutsche Hydrographische Zeitschrift* 42, 133–149.
- Johns, B., 1991. The modelling of the free surface flow of water over topography. *Coastal Engineering* 15, 257–278.
- Johns, B., Xing, J., 1993. Three-dimensional modelling of the free surface turbulent flow of water over a bedform. *Continental Shelf Research* 13, 705–721.
- Kamenkovich, V.M., 1967. On the coefficients of eddy diffusion and viscosity in large-scale oceanic and atmospheric motions. *Izvestiya, Atmospheric and Ocean Physics* 3, 1326–1333.
- Kämpf, J., Backhaus, J.O., 1998. Shallow, brine-driven free convection in polar oceans: Nonhydrostatic numerical process studies. *Journal of Geophysical Research* 103 (C3), 5577–5593.
- van Kan, J., 1986. A second-order accurate pressure correction scheme for viscous incompressible flow. *Journal of Science and Statistical Computation* 7, 870–891.
- Kanarska, Y., Maderich, V., 2003. A non-hydrostatic numerical model for calculating free-surface stratified flows. *Ocean Dynamics* 53, 176–185.
- Kanarska, Y., Shchepetkin, A.F., McWilliams, J.C., 2007. Algorithm for non-hydrostatic dynamics in the Regional Oceanic Modeling System. *Ocean Modelling* 18, 143–174.
- Kang, D., Fringer, O.B., 2012. Energetics of Barotropic and Baroclinic Tides in the Monterey Bay Area. *Journal of Physical Oceanography* 42, 272–290.
- Kantha, L.H., Clayson, C.A., 2000. *Numerical Models of Oceans and Oceanic Processes*. Academic Press.
- Kasahara, A., 1974. Various Vertical Coordinate Systems Used For Numerical Weather Prediction. *Monthly Weather Review* 102, 509–522.

- Keilegavlen, E., Berntsen, J., 2009. Non-hydrostatic pressure in σ -coordinate ocean models. *Ocean Modelling* 28, 240–249.
- Kirwan, Jr., A.D., 1969. Formulation of Constitutive Equations for Large-Scale Turbulent Mixing. *Journal of Geophysical Research* 74 (28), 6953–6959.
- Klingbeil, K., 2009. Testing the feasibility of an alternative approach for including nonhydrostatic dynamics into the General Estuarine Transport Model. Master's thesis. Universität Rostock.
- Klingbeil, K., Burchard, H., 2013. Implementation of a direct nonhydrostatic pressure gradient discretisation into a layered ocean model. *Ocean Modelling* 65, 64–77.
- Klingbeil, K., Mohammadi-Aragh, M., Gräwe, U., Burchard, H., 2013. Quantification of spurious dissipation and mixing – Discrete Variance Decay in a Finite-Volume framework. *Ocean Modelling* (submitted).
- Kumar, N., Voulgaris, G., Warner, J.C., 2011. Implementation and modification of a three-dimensional radiation stress formulation for surf zone and rip-current applications. *Coastal Engineering* 58, 1097–1117.
- Kumar, N., Voulgaris, G., Warner, J.C., Olabarrieta, M., 2012. Implementation of the vortex force formalism in the coupled ocean-atmosphere-wave-sediment transport (COAWST) modeling system for inner shelf and surf zone applications. *Ocean Modelling* 47, 65–95.
- Kundu, P.K., Cohen, I.M., 2008. *Fluid Mechanics*. Academic Press. 4 edition.
- Labeur, R.J., Pietrzak, J.D., 2005. A fully three dimensional unstructured grid non-hydrostatic finite element coastal model. *Ocean Modelling* 10, 51–67.
- Lai, Z., Chen, C., Beardsley, R.C., Rothschild, B., Tian, R., 2010a. Impact of high-frequency nonlinear internal waves on plankton dynamics in Massachusetts Bay. *Journal of Marine Research* 68, 259–281.
- Lai, Z., Chen, C., Cowles, G.W., Beardsley, R.C., 2010b. A nonhydrostatic version of FVCOM: 1. Validation experiments. *Journal of Geophysical Research* 115, C11010.
- Lane, E.M., Restrepo, J.M., McWilliams, J.C., 2007. Wave-Current Interaction: A Comparison of Radiation-Stress and Vortex-Force Representations. *Journal of Physical Oceanography* 37, 1122–1141.
- Larson, J., Jacob, R., Ong, E., 2005. The Model Coupling Toolkit: A New Fortran90 Toolkit for Building Multiphysics Parallel Coupled Models. *International Journal of High Performance Computing Applications* 19, 277–292.
- Lax, P.D., Wendroff, B., 1960. Systems of Conservation Laws. *Communications on Pure and Applied Mathematics* XIII, 217–237.
- van der Lee, E.M., Umlauf, L., 2011. Internal wave mixing in the Baltic Sea: Near-inertial waves in the absence of tides. *Journal of Geophysical Research* 116, C10016.
- Lee, J.W., Teubner, M.D., Nixon, J.B., Gill, P.M., 2006. Application of the artificial compressibility method for turbulent open channel flows. *International Journal for Numerical Methods in Fluids* 51, 617–633.
- Legg, S., Adcroft, A.J., 2003. Internal Wave Breaking at Concave and Convex Continental Slopes. *Journal of Physical Oceanography* 33, 2224–2246.
- Leibovich, S., 1980. On wave-current interaction theories of Langmuir circulations. *Journal of Fluid Mechanics* 99, 715–724.

- Leonard, B.P., 1979. A stable and accurate convective modelling procedure based on quadratic upstream interpolation. *Computer Methods in Applied Mechanics and Engineering* 19, 59–98.
- Leonard, B.P., 1991. The ULTIMATE conservative difference scheme applied to unsteady one-dimensional advection. *Computer Methods in Applied Mechanics and Engineering* 88, 17–74.
- LeVeque, R.J., 2002. *Finite-Volume Methods for Hyperbolic Problems*. Cambridge Texts in Applied Mathematics, Cambridge University Press.
- Li, Z., Johns, B., 2001. A numerical method for the determination of weakly non-hydrostatic non-linear free surface wave propagation. *International Journal for Numerical Methods in Fluids* 35, 299–317.
- Lilly, D.K., 1966. *The Representation of Small-Scale Turbulence in Numerical Simulation Experiments*. NCAR Manuscript 281. National Center for Atmospheric Research.
- Lin, C.A., Dietrich, D.E., 1994. A numerical study of low Reynolds number 2-dimensional convective adjustment. *Geophysical & Astrophysical Fluid Dynamics* 74, 123–134.
- Longuet-Higgins, M.S., 1953. Mass Transport in Water Waves. *Philosophical Transactions of the Royal Society of London* 245, 535–581.
- Longuet-Higgins, M.S., Stewart, R.W., 1964. Radiation stresses in water waves ; a physical discussion, with applications. *Deep-Sea Research* 11, 529–562.
- Lorenz, E.N., 1963. Deterministic Nonperiodic Flow. *Journal of the Atmospheric Sciences* 20, 130–141.
- Mahadevan, A., Olinger, J., Street, R.L., 1996. A Nonhydrostatic Mesoscale Ocean Model. Part I: Well-Posedness and Scaling. *Journal of Physical Oceanography* 26, 1868–1880.
- Marsaleix, P., Auclair, F., Floor, J.W., Herrmann, M.J., Estournel, C., Pairaud, I., Ulses, C., 2008. Energy conservation issues in sigma-coordinate free-surface ocean models. *Ocean Modelling* 20, 61–89.
- Marshall, J., Hill, C., Perelman, L., Adcroft, A.J., 1997. Hydrostatic, quasi-hydrostatic, and nonhydrostatic ocean modeling. *Journal of Geophysical Research* 102 (C3), 5733–5752.
- Marshall, J., Jones, H., Hill, C., 1998. Efficient ocean modeling using non-hydrostatic algorithms. *Journal of Marine Systems* 18, 115–134.
- McWilliams, J.C., Restrepo, J.M., Lane, E.M., 2004. An asymptotic theory for the interaction of waves and currents in coastal waters. *Journal of Fluid Mechanics* 511, 135–178.
- Mellor, G.L., 2003. The Three-Dimensional Current and Surface Wave Equations. *Journal of Physical Oceanography* 33, 1978–1989.
- Mellor, G.L., 2008. The Depth-Dependent Current and Wave Interaction Equations: A Revision. *Journal of Physical Oceanography* 38, 2587–2596.
- Mellor, G.L., 2011a. Corrigendum. *Journal of Physical Oceanography* 41, 1417–1418.
- Mellor, G.L., 2011b. Wave radiation stress. *Ocean Dynamics* 61, 563–568.
- Mellor, G.L., Blumberg, A.F., 1985. Modeling Vertical and Horizontal Diffusivities with the Sigma Coordinate System. *Monthly Weather Review* 113, 1379–1383.
- Mercier, C., Delhez, E.J.M., 2010. Really TVD advection schemes for the depth-integrated transport equation. *Ocean Modelling* 33, 10–19.

- Michaud, H., Marsaleix, P., Leredde, Y., Estournel, C., Bourrin, F., Lyard, F., Mayet, C., Ardhuin, F., 2012. Three-dimensional modelling of wave-induced current from the surf zone to the inner shelf. *Ocean Science Discussions* 8, 657–681.
- Moghimi, S., Klingbeil, K., Gräwe, U., Burchard, H., 2012. A direct comparison of a depth-dependent Radiation stress formulation and a Vortex force formulation within a three-dimensional coastal ocean model. *Ocean Modelling* (in press).
- Molenkamp, C.R., 1968. Accuracy of Finite-Difference Methods Applied to the Advection Equation. *Journal of Applied Meteorology* 6, 160–167.
- Morales Maqueda, M.A., Holloway, G., 2006. Second-order moment advection scheme applied to Arctic Ocean simulation. *Ocean Modelling* 14, 197–221.
- Moukalled, F.H., Darwish, M., 2000. A unified Formulation of the segregated Class of Algorithms for Fluid Flow at all Speeds. *Numerical Heat Transfer* 37, 103–139.
- Nausch, G., Feistel, R., Umlauf, L., Nagel, K., Siegel, H., 2009. Hydrographisch-chemische Zustandseinschätzung der Ostsee 2008. Number 77 in *Meereswissenschaftliche Berichte*, Leibniz Institute for Baltic Sea Research Warnemünde.
- Orlanski, I., 1981. The Quasi-Hydrostatic Approximation. *Journal of the Atmospheric Sciences* 38, 572–582.
- Özgökmen, T.M., Chassignet, E.P., 2002. Dynamics of Two-Dimensional Turbulent Bottom Gravity Currents. *Journal of Physical Oceanography* 32, 1460–1478.
- Phillips, N.A., 1966. The Equations of Motion for a Shallow Rotating Atmosphere and the "Traditional Approximation". *Journal of the Atmospheric Sciences* 23, 626–628.
- Phillips, O.M., 1977. *The Dynamics of the Upper Ocean*. Cambridge University Press. 2nd edition.
- Pietrzak, J.D., 1998. The Use of TVD Limiters for Forward-in-Time Upstream-Biased Advection Schemes in Ocean Modeling. *Monthly Weather Review* 126, 812–830.
- Pope, S.B., 2000. *Turbulent Flows*. Cambridge University Press.
- Prather, M.J., 1986. Numerical Advection by Conservation of Second-Order Moments. *Journal of Geophysical Research* 91 (D6), 6671–6681.
- Reissmann, J.H., Burchard, H., Feistel, R., Hagen, E., Lass, H.U., Mohrholz, V., Nausch, G., Umlauf, L., Wiczeorek, G., 2009. Vertical mixing in the Baltic Sea and consequences for eutrophication - A review. *Progress in Oceanography* 52, 47–80.
- Rennau, H., Burchard, H., 2009. Quantitative analysis of numerically induced mixing in a coastal model application. *Ocean Dynamics* 59, 671–687.
- Rennau, H., Schimmels, S., Burchard, H., 2012. On the effect of structure-induced resistance and mixing on inflows into the Baltic Sea: A numerical model study. *Coastal Engineering* 60, 53–68.
- Reynolds, O., 1883. An Experimental Investigation of the Circumstances Which Determine Whether the Motion of Water Shall Be Direct or Sinuous, and of the Law of Resistance in Parallel Channels. *Philosophical Transactions of the Royal Society of London* 174, 935–982.
- Reynolds, O., 1895. On the Dynamical Theory of Incompressible Viscous Fluids and the Determination of the Criterion. *Philosophical Transactions of the Royal Society of London* 186, 123–164.
- Shchepetkin, A.F., McWilliams, J.C., 1998. Quasi-Monotone Advection Schemes Based on Explicit Locally Adaptive Dissipation. *Monthly Weather Review* 126, 1541–1580.

- Shchepetkin, A.F., McWilliams, J.C., 2003. A method for computing horizontal pressure-gradient force in an oceanic model with a non-aligned vertical coordinate. *Journal of Geophysical Research* 108 (C3), 3090–3124.
- Shchepetkin, A.F., McWilliams, J.C., 2005. The Regional Ocean Modeling System: A split-explicit, free-surface, topography-following-coordinate oceanic model. *Ocean Modelling* 9, 347–404.
- Shen, C.Y., Evans, T.E., 2004. A free-surface hydrodynamic model for density-stratified flow in the weakly to strongly non-hydrostatic regime. *Journal of Computational Physics* 200, 695–717.
- Simpson, J.E., 1982. Gravity currents in the laboratory, atmosphere, and ocean. *Annual Reviews for Fluid Mechanics* 14, 213–234.
- Smagorinsky, J., 1963. General Circulation Experiments with the Primitive Equations. *Monthly Weather Review* 91, 99–164.
- Smagorinsky, J., 1993. Some Historical Remarks on the Use of Nonlinear Viscosities, in: Galperin, B., Orszag, S.A. (Eds.), *Large Eddy Simulation of Complex Engineering and Geophysical Flows*. Cambridge University Press, pp. 3–36.
- Smith, R.D., McWilliams, J.C., 2003. Anisotropic horizontal viscosity for ocean models. *Ocean Modelling* 5, 129–156.
- Spurk, J.H., Aksel, N., 2008. *Fluid Mechanics*. Springer. 2nd edition.
- Stashchuk, N., Vlasenko, V., Hutter, K., 2005. Numerical Modelling of disintegration of basin-scale internal waves in a tank filled with stratified water. *Nonlinear Processes in Geophysics* 12, 955–964.
- Strang, G., 1968. On the Construction and Comparison of Difference Schemes. *Journal on Numerical Analysis* 5, 506–517.
- Sweby, P.K., 1984. High Resolution Schemes Using Flux Limiters for Hyperbolic Conservation Laws. *Journal on Numerical Analysis* 21, 995–1011.
- Tartinville, B., Deleersnijder, E., Lazure, P., Proctor, R., Ruddick, K.G., Uittenbogaard, R.E., 1998. A coastal ocean model intercomparison study for a three-dimensional idealised test case. *Applied Mathematical Modelling* 22, 165–182.
- Taylor, K.E., 2001. Summarizing multiple aspects of model performance in a single diagram. *Journal of Geophysical Research* 106 (D7), 7183–7192.
- Témam, R., 1969. Sur l'Approximation de la Solution de Équations de Navier-Stokes par la Méthode de Pas Fractionnaires (II). *Arch. Rational Mech. Anal.* 32, 377–385.
- Thiem, Ø., Berntsen, J., 2009. Numerical studies of large-amplitude internal waves shoaling and breaking at shelf slopes. *Ocean Dynamics* 59, 937–952.
- Tseng, Y.H., Breaker, L.C., 2007. Nonhydrostatic simulations of the regional circulation in the Monterey Bay area. *Journal of Geophysical Research* 112, C12017.
- Tseng, Y.H., Dietrich, D.E., Ferziger, J.H., 2005. Regional circulation of the Monterey Bay region: Hydrostatic versus nonhydrostatic modeling. *Journal of Geophysical Research* 110, C09015.
- Uchiyama, Y., McWilliams, J.C., Shchepetkin, A.F., 2010. Wave-current interaction in an oceanic circulation model with a vortex-force formalism: Application to the surf zone. *Ocean Modelling* 34, 16–35.
- Umlauf, L., Burchard, H., 2005. Second-order turbulence closure models for geophysical boundary layers. A review of recent work. *Continental Shelf Research* 25, 795–827.

- Ursell, F., 1953. The long-wave paradox in the theory of gravity waves. *Mathematical Proceedings of the Cambridge Philosophical Society* 49, 685–694.
- Venayagamoorthy, S.K., Fringer, O.B., 2012. Examining Breaking Internal Waves on a Shelf Slope Using Numerical Simulations. *Oceanography* 25, 132–139.
- Veronis, G., 1968. Comments on Phillip's Proposed Simplification of the Equations of Motion for a Shallow Rotating Atmosphere. *Journal of the Atmospheric Sciences* 25, 1154–1155.
- Vitousek, S., Fringer, O.B., 2011. Physical vs. numerical dispersion in nonhydrostatic ocean modeling. *Ocean Modelling* 40, 72–86.
- Wadzuk, B.M., 2004. Hydrostatic and Non-hydrostatic Internal Wave Models. Ph.D. thesis. University of Texas at Austin.
- Wajsowicz, R.C., 1993. A Consistent Formulation of the Anisotropic Stress Tensor for Use in Models of the Large-Scale Ocean Circulation. *Journal of Computational Physics* 105, 333–338.
- Wang, B., Fringer, O.B., Giddings, S.N., Fong, D.A., 2009. High-resolution simulations of a macrotidal estuary using SUNTANS. *Ocean Modelling* 28, 167–192.
- Warming, R.F., Beam, R.M., 1976. Upwind Second-Order Difference Schemes and Applications in Aerodynamic Flows. *AIAA Journal* 14, 1241–1249.
- White, A.A., Bromley, R.A., 1995. Dynamically consistent, quasi-hydrostatic equations for global models with a complete representation of the Coriolis force. *Quarterly Journal of the Royal Meteorological Society* 121, 399–418.
- Williams, G.P., 1972. Friction Term Formulation and Convective Instability in a Shallow Atmosphere. *Journal of the Atmospheric Sciences* 29, 870–876.
- Xing, J., Davies, A.M., 2006. Processes influencing tidal mixing in the region of sills. *Geophysical Research Letters* 33.
- Xing, J., Davies, A.M., 2007. On the importance of non-hydrostatic processes in determining tidally induced mixing in sill regions. *Continental Shelf Research* 27, 2162–2185.
- Yuan, H., Wu, C.H., 2004. An implicit three-dimensional fully non-hydrostatic model for free-surface flows. *International Journal for Numerical Methods in Fluids* 46, 709–733.
- Zhang, Z., Fringer, O.B., Ramp, S.R., 2011. Three-dimensional, nonhydrostatic numerical simulation of nonlinear internal wave generation and propagation in the South China Sea. *Journal of Geophysical Research* 116, C05022.